Visualization of Twin Oscillating Foils in the Near Wake of a Model Destroyer

by

Jennifer Tam Lin

S.B., Ocean Engineering, Massachusetts Institute of Technology (2000)

Submitted to the Department of Ocean Engineering
in partial fulfillment of the requirements for the degree of

Master of Science in Naval Architecture and Marine Engineering

at the

MASSACHUSETTS INSTITUTE OF TECHNOLOGY

June 2000

Author................ ....
Department of Ocean Engineering
May 23, 2000

Certified by........
....
Michael S. Triantafyllou
Professor of Ocean Engineering
Thesis Supervisor

Accepted by ....
....
Nicholas Patrikalakis
Kawasaki Professor of Engineering
Chairman, Departmental Committee on Graduate Studies

Visualization of Twin Oscillating Foils in the Near Wake of a Model Destroyer

by
Jennifer Tam Lin

Abstract

The propulsive properties of a novel four-degree-of-freedom twin oscillating foil mechanism were investigated by conducting dye visualizations. A prototype system was developed and mounted on the stern of a model DDG-51 destroyer. Flow visualization experiments were performed in the MIT Testing Tank over a range of Strouhal numbers, St. = 0.1 to 0.5; angles of attack, α = 10°, 15°, 20°, 25°, and 30°; and phase, ϕ = 90°, between heave and pitch motions. Phase angles, ϕ = 70° and 110°, were also tested at a subset of parameters. The Reynolds numbers are R_C = 15,000 and R_L = 600,000, based on the foil chord length and the ship's length, respectively. The carriage towed the boat with a fixed forward speed of U = 0.2 m/s. An on-board camera recorded the vortex shedding patterns in the near wake.

Wake structures over the range of parameters were mapped from the digitized footage of visualizations. The predominant shedding pattern has elongated loops of vortices due to vortices that convect faster outward and inward than downstream. This pattern is typical of higher Strouhal number experiments and is indicative of thrust. The vortical patterns were compared to previous studies on oscillating foils.

Thesis Supervisor: Michael S. Triantafyllou
Title: Professor of Ocean Engineering

Acknowledgments

First I would like to thank my advisor Prof. Michael Triantafyllou for his silent, but steadfast encouragement in all of my work. I am extremely grateful to Dr. Franz Hover who has been so helpful in every aspect of this project. I've learned to like his "not-a-show-stopper" approach to experimentation.

I wish to thank the Ocean Engineering Department at MIT for their financial support in February and their endeavors for improvement of student life and learning.

Working at the Towing Tank has been a great learning experience for me. I have to say a major thank you to Alex, Albert, Craig, Dave, Doug, John, Josh, and Michael for being helpful and for being cool people to work with. Thanks to all the UROPs who lent a helping hand.

Many members of the faculty have truly been supportive during my years at MIT: Kristin Gunst, Prof. John Leonard, Prof. Nick Makris, Prof. Patty Manning, Jean Sucharewicz, Bonnie Walters, Prof. Mark Welsh, and Prof. T. Wierzbicki. I am thankful to them for their advice and approachable demeanor. I especially wish to express my gratitude to Prof. T. F. Ogilvie, who has been advising me from afar.

I am so glad to have been a part of the MIT Cross Products last year when I first began my thesis work. Worship and rehearsals were always refreshing. Thanks Ben, Bryan, Christine, Connie, Dan, David, Jane, Jen, Jesse, Julie, Ryan, Tony, Vanessa, and Vivian for a wonderful year of fellowship, singing and ministry!

I would like to thank all of my friends at MIT for being here with me. To the best of the bunch Erynn, I wish her the best in medical school and with Jung.

My parents are awesome for being wonderfully supportive throughout my years at MIT. To my little bro Kenric, thanks for making childhood challenging and fun.

My husband Calvin has given me the strength and patience to carry on. I look forward to being reunited with him. Last, but not least, thank you God for the sacrifice.

Contents

List of Figures

List of Tables

Chapter 1

Introduction

Over millions of years, fish have evolved to propel themselves through the water rather effortlessly and efficiently. The interest that was generated on how they are able to swim so efficiently is primarily credited to James Gray. In a 1935 study on the hydrodynamic characteristics of a swimming dolphin, Gray illustrates how the power generated by the muscles of a dolphin is not sufficient to propel it at the high swimming speeds it is capable of [7]. The required thrust was noted to be seven times the force that is generated from the muscles. His quandary intrigued scientists and engineers to pursue an explanation for this paradox now known as Gray's Paradox. Through biomimicry, researchers have shown that a fish's undulating body and caudal fin is used to control vortices to its propulsive and maneuvering advantage, offering key insight to the mystery.

Through studying fish, researchers realized that other aquatic animals such as penguins and turtles have the ability to swim as quickly and efficiently as fish. The flapping motion of their pectoral flippers can produce favorable thrust.

1.1 Motivation

Currently, propulsors such as propellers are optimized to operate efficiently at set speeds and are matched specifically to a certain ship design. Other forms of newer propulsive systems include water jets, which are designed for use in high-speed craft. Thus it would be convenient for large vessels if there existed propulsors that could propel vessels over a wide range of speeds with high efficiencies. As a result engineers have turned to mimic nature's efficient swimmers. One such device utilizes concepts derived from observations of penguin swimming. A novel twin foil-propulsive system was created for

8

direct applications to the marine transport industry and ship maneuverability. This and similar types of oscillating foil propulsion can provide useful insight into new propulsive designs, further improvements in conventional ships, and potentially substantial economic savings.

1.2 Novel Mechanisms for Propulsion

The first generation oscillating foilboat or Penguin Boat (shown in Figure 1-1) was a small mechanism permanently built into a Mariner class aircraft carrier model hull. Built by Czarnowski [4], it had two foils that protruded into the water and flapped. Through experimental testing, Czarnowski revealed that oscillating foil propulsion had an advantage over propellers due to the increase in swept area. While in this case the increase in efficiency is only about 1%, the results of his preliminary study were encouraging. Spurred on by initial findings, the second generation mechanism, Proteus, was developed. This iteration is closer in design to today's flapping foil mechanism, which is also mounted on the stern of the Arleigh Burke DDG-51 destroyer hull model. Dye visualizations and efficiency tests were conducted in hopes of illuminating the ideal parameters for efficient oscillating foil propulsion. These tests were inconclusive in the laboratory so Czarnowski chose to test the ship in an untethered configuration on the Charles River. These "real-world" tests were successful and the ship was shown capable of propelling itself at a maximum speed of 1.75 m/s while flapping at 3 Hz.

9
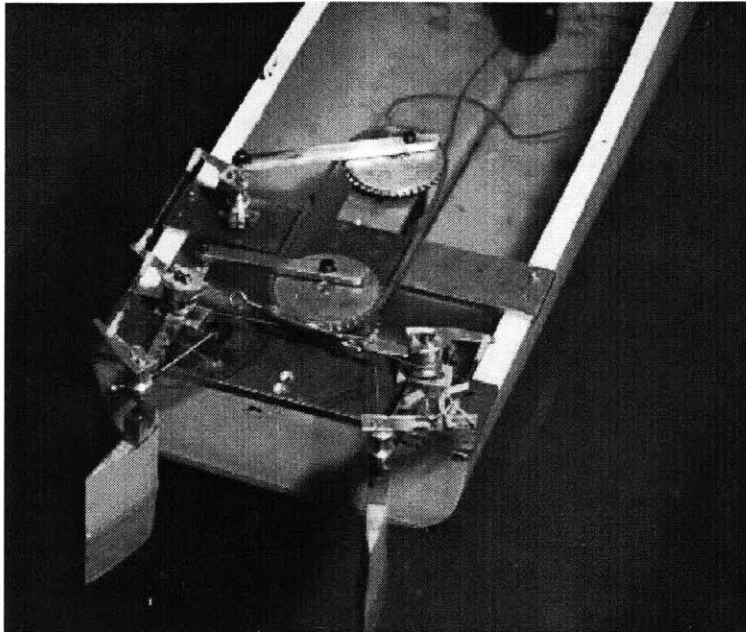
Figure 1-1: The original Penguin Boat (on display at the Hart Gallery at MIT).

Other researchers have designed and investigated unique configurations of foils or fins for efficient propulsion. These designs exemplify that propulsive energy can be harnessed using oscillating foil propulsion.

Nagai, Teruya, and Isaka's oscillating wing propulsive ship (shown in Figure 1-2) is an endeavor to utilize thunniform (using tail for propulsion) swimming with a lunate shaped wing to propel a ship [12]. The mechanism involves movement of the wing in pitch and heave simultaneously. Powered by a motorbike engine, the range of oscillation frequencies is from 0-5.06 Hz at an amplitude of oscillation of 400 mm. Nagai et al. noticed a tendency of the speed to reach a plateau at higher frequency ranges, but believe that the performance of the mechanism would improve upon the optimization of several components.
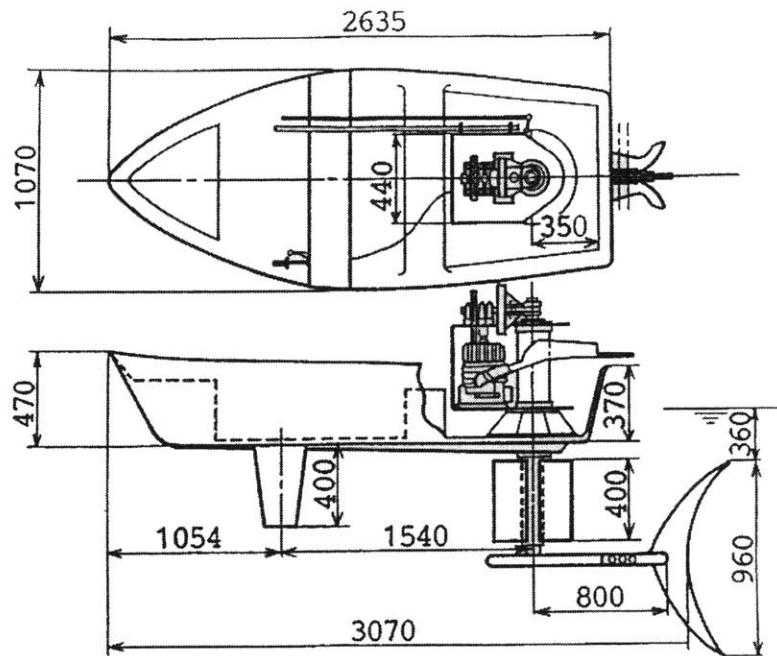
Figure 1-2: Oscillating Wing Propulsive Ship

In another investigation on using oscillating foils for propulsion, Yamaguchi and Bose [19] used linear and nonlinear theory to compare open water efficiencies of rigid foils, flexible foils, and screw propellers in a particular application behind a 200,000 DWT tanker. The Shipbuilding Research Association (SRA) of Japan conducted research in 1986 on various ship propulsion devices. The design for their ship and foil configuration is shown in Figure 1-3. The SRA foil had a cross-section shape of NACA 63A015; a rectangular planform; and an elastic trailing edge starting midchord with a Young's Modulus of 3.0×10^6 Pa. The chord length was 7 m and the span was 49 m. The nondimensional Young's Modulus of the flexible trailing edge is 112.96 at a ship speed of 14 kt. Yamaguchi and Bose have found that the ship speed affects the flexible foil more than the rigid one due to the increase in nondimensional Young's Modulus as ship speed is lowered, effectively increasing the stiffness of the foil.

An advantage of oscillating foil propulsors is that the efficiency is less sensitive to working conditions than a screw propeller. Although open water efficiency of the screw propeller was lower than the foils from the SRA tests by 17-25%, when placed behind the

ship, the quasi-efficiency was higher than the rigid foil by 3-4%. This quasi-efficiency was lower than a partly flexible foil, which was 72% efficient, a difference of 3.5%.
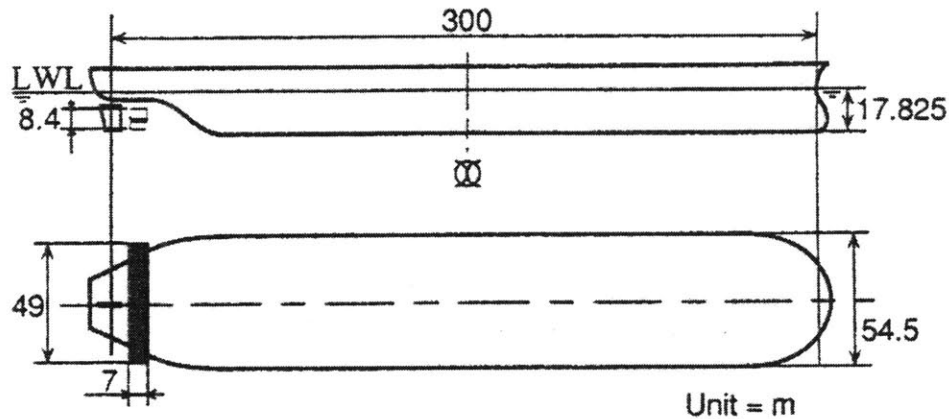
Figure 1-3: Arrangement of ship and oscillating foil propulsor. [Yamaguchi and Bose]

Another novel propulsion device is the Hobie Mirage, a pedal powered kayak (shown in Figure 1-4) designed by Greg Ketterman and marketed by Hobie Cat Company. The propulsion system consists of two flippers located on the centerline under the kayak that flap and produce thrust when a person steps on pedals alternately similar to a peddle boat. The flippers both sway and yaw and appear to be flexible. No experimental data on this apparatus was found. However, this is a patent pending device that has been marketed to the public and has met with overall favorable reviews.
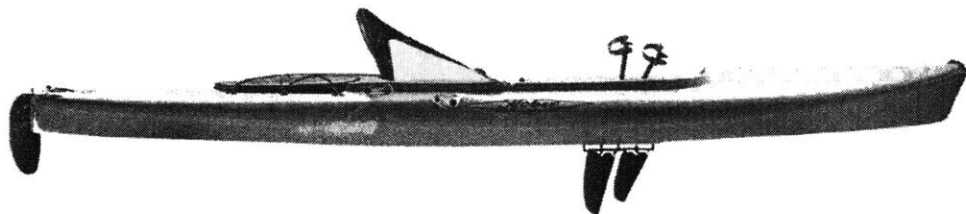
Figure 1-4: Hobie Mirage Kayak

Overall the applications of oscillating foil propulsion in both the recreational and industrial sectors are exciting. This thesis continues the investigation into such devices

by delving into the vortex pattern interactions generated by twin oscillating foils, but first a discussion of the motion parameters and previous work on single oscillating foils is warranted.

1.3 Definitions

The motion of a flapping foil can be defined by several motion parameters. The foil heaving motion is governed by a simple sinusoid

$$h(t) = h_o \sin(\omega t), \qquad 1.1$$

where h_0 is the maximum heave displacement and ω is the angular frequency. While the foil is heaving, the pitch oscillations lag behind the heave and follow the motion dictated by the pitch angle theta,

$$\theta(t) = \theta_o \sin(\omega t + \phi), \qquad 1.2$$

where θ_0 is the maximum pitch amplitude and ϕ is the phase angle between heave and pitch.

Most literature encountered uses reduced frequency k or $f*$ as the non-dimensional number of importance. This reduced frequency compares the time that a particle spends moving over the foil chord and the period of the motion and is defined as

$$k = \frac{\pi f c}{U} \quad \text{or} \quad f* = \frac{\omega c}{2U}, \qquad 1.3$$

where U is the free stream velocity, f is oscillation frequency, and c is the chord length of the foil. Here we define, the Strouhal number as

$$St = \frac{2h_0 f}{U}. \qquad 1.4$$

This parameter is more descriptive than using reduced frequency since the shedding frequency is proportional to the wake width, which is generally unknown, but is taken to be twice the heave amplitude or trailing edge excursion.

13
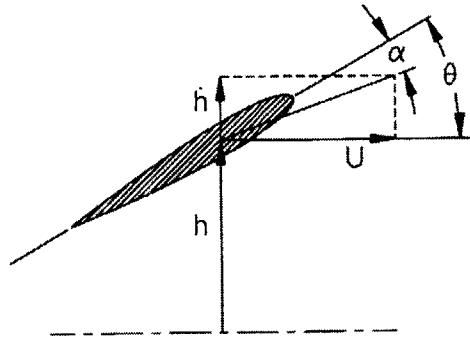
Figure 1-5: Foil parameters.

Another important parameter is the angle of attack. This is the angle at which the flow hits the foil, measured about the pivot point of the foil. The angle of attack is defined as

$$\alpha = \arctan\left[\frac{\dot{h}\omega}{U}\right] - \theta,$$

1.5

where $\dot{h}$ is the first derivative of h (equation 1.1) and θ is from equation 1.2.

Using equations 1.1-1.5 to define the foil motion, a path such as shown in Figure 1-6 can be expected.
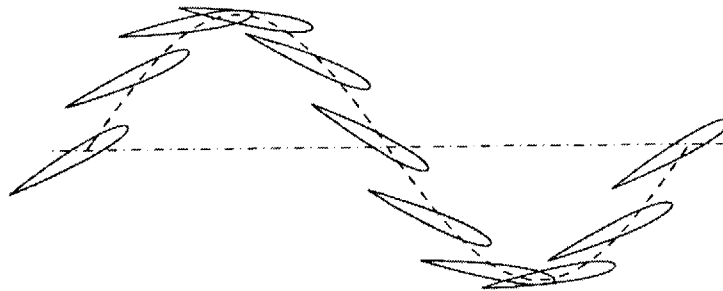
Figure 1-6: Foil moving with time.

Finally the non-dimensional Reynolds number provides a comparison of inertial forces to viscous forces. It is defined as

$$\text{Re} = \frac{Uc}{v} = \frac{\rho Uc}{\mu},$$

1.6

14

where ν is the kinematic viscosity, ρ is density, and μ is dynamic viscosity. All of these parameters can be varied to result in dramatic changes in vortex shedding patterns. Examples of such changes are outlined in the next section for single pitching foils.

1.4 Theory

It is well known that bluff bodies shed vortices that are arranged in such a way as to create a drag, a force against the direction of travel. A classic example of this drag wake is the von Kármán vortex street which is formed when a new vortex alternately sheds from either side of the cylinder and moves downstream (see figure 1-7). It was Strouhal who realized that the vortices are shed proportional to U/d, where d is $2h_0$ in this case. A propulsive signature could be a reverse Kármán street such as the one in Figure 1-8. In accordance with the Biot-Savart law for fluids, the shed vortices induce velocity on each other in the downstream direction, creating a jet. A plane cut along the lateral line of a swimming fish typically reveals a similar signature when the fish is producing thrust.
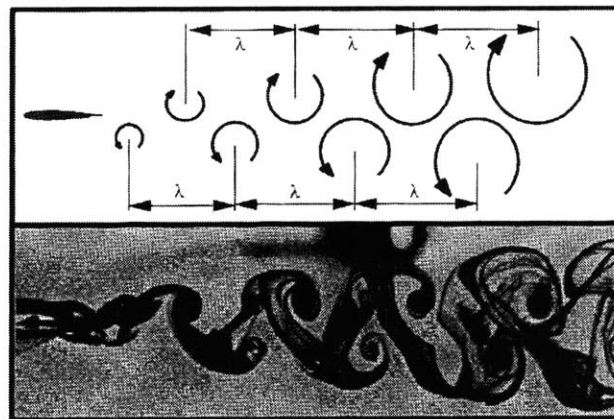
Figure 1-7: Vortex street indicative of drag. [Jones et al.]

If the direction of the vortex swirl and its proximity to other vortices are known, the path of the flow can be deduced. When velocity is induced by vortices, it has a component of "lift," or force in the inward or outward direction, and a component in the downstream (or upstream) direction. The resultant force in the downstream direction is thrust. For

15

example, Figure 1-9 shows alternating vortices placed in a straight line, producing zero thrust, which has no momentum deficit or excess.
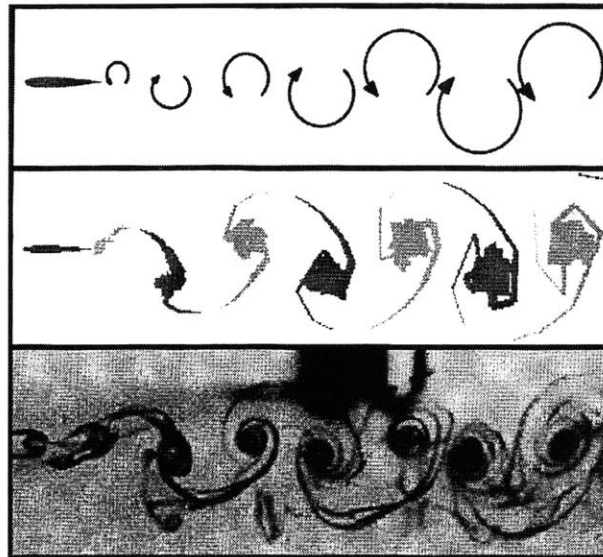
Figure 1-8: Vortex street indicative of thrust. [Jones et al.]
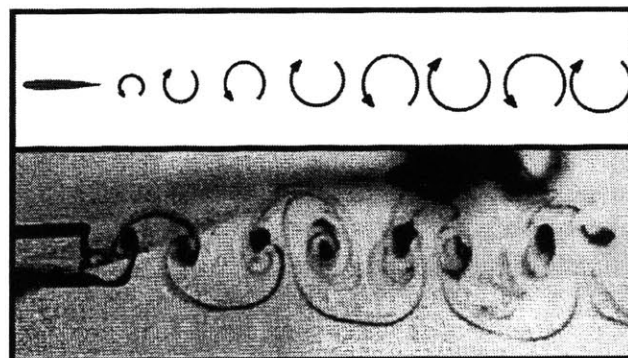
Figure 1-9: Vortex street indicative of zero drag. [Jones et al.]

Throughout the thesis, the term 'wake' is used liberally, when in actuality the flow may be a jet. The term will be differentiated using terms such as a drag wake and a jet wake.

1.5 Previous Work in Visualization of Flow

Many researchers have used various techniques of visualization in determining flow around airfoils and hydrofoils using smoke, dye, and neutrally-buoyant particles.

From experiments conducted on cylinders in the towing tank, Williamson and Roshko [19] describe major vortex patterns in the fundamental lock-in region "2S,""2P," and "P + S." The "S" stands for single and "P" for pair. The "2S" pattern is the typical von Kármán vortex street. The "2P" formation has opposite sign vortices pairing and convecting laterally outward from the wake centerline. "P + S" mode is asymmetric and sheds a vortex pair and a single vortex each cycle. He also noted "P," "2P," and "2P +2S" formations and coalescence in the near wake.

Freymuth [5] studied propulsive vortical signatures of NACA 0015 airfoils in pure plunging motion and in pure pitching motion. He mentioned that increases in mean angle and in pitch or plunge amplitude tend to cause leading edge separation. Conducted experiments showed that plunging sinusoidal motion can generate thrust.

Koochesfahani [10] performed experiments investigating the vortical flow patterns in the wake of a NACA 0012 airfoil in a low-speed water channel. By controlling frequency, amplitude, and shape of the oscillation waveform, he demonstrated that much control can be exercised over the structure of the wake. Laser Doppler velocimetry was used to measure the streamwise velocity, thereby finding thrust and drag corresponding to each flow pattern. Koochesfahani found that nonsinusoidal motions result in waveforms that may have one strong vortex accompanied by two smaller ones or vice versa. Also, the critical reduced frequency for thrust creation depended on the amplitude of oscillation.

Using smoke to examine the flow field around a flapping airfoil, Panda and Zaman [13] focused on further understanding the dynamic stall vortex (DSV) or leading edge vortex and trailing edge vortex (TEV) on airfoils and lifting surfaces in unsteady flow environments. They have noticed that literature does not address the TEV and mushroom formations that follow DSV and lift generation. Through experimentation, Panda and Zaman found that the phase delay in the shedding of the DSV varies approximately linearly with k over the full range of k covered.

17

Ohmi et al. [12] compared experimental and numerical visualization of two NACA 0012 foils: one with a half-chord model and one with one-third-chord model. Experiments at high frequencies suggest that the large incidence cases are more sensitive to any variation of flow conditions, more specifically the product of the reduced frequency and amplitude. The diverse vortical patterns are basically determined by whether the vortices shed from the leading edge travel downstream in tandem with younger trailing edge vortices. Also, the Reynolds number is an important parameter if the generated wake remains unsettled in an intermediate pattern, but the overall effect is not comparable to that of other parameters.

Gopalkrishnan [6] looked at cylinder-foil vortex interaction as a paradigm for vorticity control. He found that the oscillating foil in the wake of a cylinder can reposition the cylinder's vortices from their Karman vortex street configuration thereby entering into one of three modes: vortex pairing, destructive vortex merging, and constructive vortex merging. In both flow visualization and force measurements, the separation distance between the cylinder and the foil affect the behavior.

Anderson [2] investigated the propulsive properties of a harmonically oscillating rigid flapping foil. She found that dynamic stall appears in most cases of thrust production and is dependent on the kinematics of the foil. The DSV is an efficient mechanism of transferring momentum into the wake and can be manipulated to increase the propulsive efficiency. The leading edge separation often dominates the wake structure for a wide range of Strouhal numbers and maximum angles of attack as low as 10°. For high efficiency and high thrust, the reverse Kármán street was prevalent. The phase affects the development of DSV. Thrust and vortex strength increase with Strouhal number and maximum angle of attack. In another set of experiments, Anderson used DPIV to study the wake interaction of a bluff body and flapping foil. Upstream vortices either pulled apart to destruction or merged with leading or trailing edge vortices.

Jones et al. [9] compared both numerical and experimental wake structures of airfoils undergoing oscillatory plunging motions. Using laser Doppler velocimetry, they were able to obtain velocity from the flow. Two-color dye showed unsteady wake structures. Qualitative and quantitative comparisons of these wake patterns were made from photographs of the water tunnel experiments with digital images from panel code

18

interface. Figures 1-7, 1-8, and 1-9 are Jones' experimental and numerical work, excellent examples of vortical signatures.

1.6 Objective of Thesis

From previous research, we can see how studying the flow signature behind foils and bluff bodies have helped in building a fundamental basis of knowledge on the behavior of vortices and their formation. The aim of this thesis is to elucidate the propulsive vortical signature of two symmetrically oscillating foils in the wake of a model destroyer by dye visualization. By studying the wake structure, we may gain some insight into the mechanisms of vorticity generation and control.

Chapter 2

Experimental Set-Up

2.1 Towing Tank Testing Facility

The laboratory is part of the Department of Ocean Engineering at MIT. It has a main testing tank and an adjoining control room commonly referred to as the bridge. An I-beam, with an attached rail, is suspended above the tank. Two carriages that run along the rail were designed to tow objects at regulated speeds through the water. One of the carriages is occupied by the RoboTuna, the other one by the Virtual Cable Testing Apparatus (VCTA), two additional projects at the Towing Tank.

2.2 Testing Tank and Carriage

The main testing tank is 30m long, 2.6 m wide, and filled to a water height of 1.1 m. The VCTA carriage was used for testing the mechanism. It is equipped with power supplies, a bus that transfers information back and forth from the bridge, and a transmitter to the bridge. Communication with on-carriage devices and computers occurs from the bridge through the transmitter. For ease of working between projects, the original VCTA set-up has been left intact and the addition of a carriage extender has adapted the carriage for testing.

The VCTA carriage can operate at a range of speeds from 0.2 m/s to 1.2 m/s with adjustable acceleration and deceleration rates. Carcon, the computer system, controls the commanded towing speed of the carriage.

2.3 Destroyer Model

The hull model is a scale DDG-51 Arleigh-Burke class destroyer 5514: 3.4 m length, 48.3 cm beam, 15.2 cm draft. The model requires 66 kg of ballast, not including its own weight, to trim the boat to the design water line. It was originally constructed of strong fiberglass and wood with a gray layer of paint. Aft of the bulbous bow, turbulence stimulators are permanently adhered to ensure that the boat is operating in the turbulent regime.

Digital particle laser velocimetry (DPIV) has been used for studying the destroyer hull in a comparison of vortical signatures of model boats. Ames [1], a graduate student who had worked at the Towing Tank, discovered that the DDG-51 has two distinct symmetrical wakes. The destroyer wake is a huge unknown in dye visualization experiments because of the complexity of the hull geometry and unknown vortical interactions with oscillating foils.

2.4 Mounting the Destroyer Hull to the Carriage

The destroyer hull was first partially ballasted by placing 30 kg distributed within. To determine whether the model is trimmed correctly, the water level was aligned with the design water line drawn on the model. The distributed weights were placed low inside the hull to lend stability in roll.

The destroyer hull was mounted slightly forward of its "hydrodynamic center" to the VCTA carriage via a strut. This minimized the sway and yaw forces on the hull. The strut (or mast) assembly was bolted to a vertically oriented linear drive (or linear slide) attached to the carriage and therefore allowed the boat to freely heave.
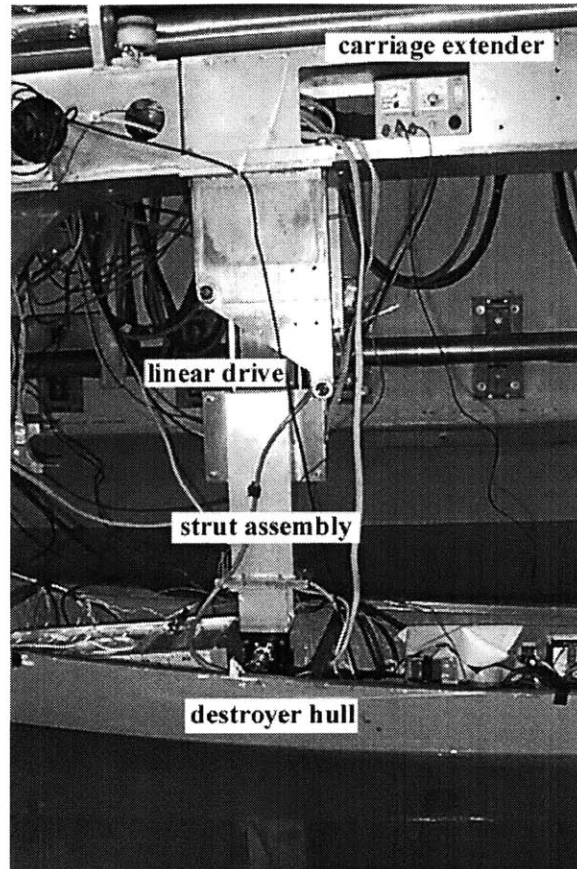
Figure 2-1: Mounting the destroyer to the carriage.

2.5 Mounting the Foilboat Mechanism to the Destroyer

The foilboat mechanism was aligned and centered on the model destroyer's stern and attached using two similarly sized C-clamps that secured the mechanism in place.

The foils extended as far beneath the water surface as possible to maximize the sweep area such that only the shafts, extending up from the quarter chord pivot point, pierced the water surface to attach to the end of the universal joints. The foils were 10 cm from the transom.
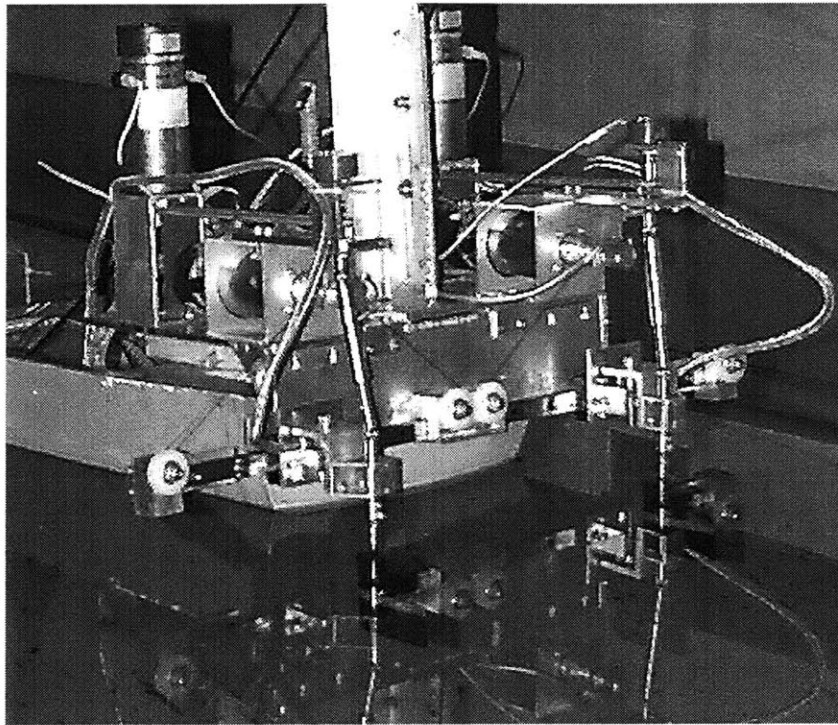
2.6 Foilboat Mechanism

The foilboat had a control box that houses equipment for motion control. Inside the box, there was a stack of cards consisting of an AMPRO CoreModule 486-II computer, a MiniModule disk drive controller, a MiniModule VGA-FP video controller, and a Motion

Engineering Inc. (MEI) 104-DSP 4-axis. The MEI card outputted commands to 4 Copley Model 403 servo amplifiers for motor control. The wires compactly led out of the box to the motors on the mechanism through Belden wires with box connectors. The four Pittman Model 14X04 DC servo motors drove the foils. BEI MX21 series encoders were affixed on the motors for MEI position (count) feedback from the motors to the MEI controller. Using the MEI software, code was written in C and MEI routines to control the oscillatory motion of the foils.

Originally designed to be autonomously operated, the foilboat was powered by two 12 V car batteries. For the purposes of running multiple experiments in the tank and avoiding recharging time, a regulated DC power supply from the wall was used instead.

Each foil was attached to aluminum pieces that connected it to a small carriage or car. The car had a ball bearing system and rode on a Thomson Accuglide Rail linear slide. The blocks held nylon bearing mounted pulleys in place. The cable originated from the right side of the car, wound around the pulley several times, wrapped around the drum four times before winding around the other pulley, and connected to the other side of the car. Motors 0 and 1 drove the heave motion by spinning the drum in one direction then the other direction. The chain belt was connected to the motor side sprockets on one end and the universal joint side sprockets that drove the pitching motion of the foils. Motors 2 and 3 were responsible for driving this segment. Figure 2-2 labels the important components of the oscillating foilboat mechanism.
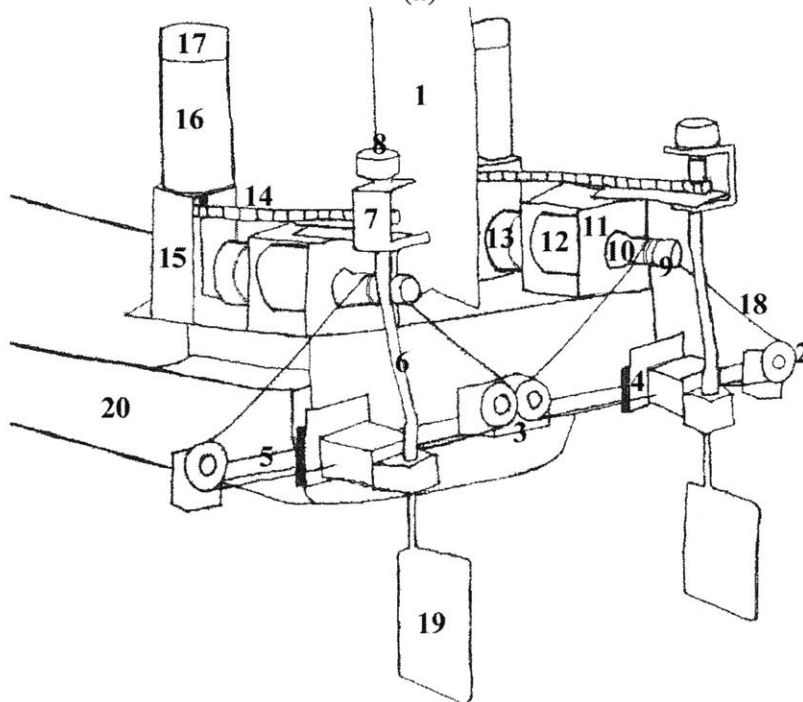
Figure 2-2: (a) Foilboat Mechanism Mounted on the Stern (b) Components of Foilboat Mechanism: 1) camera mount 2) pulley 3) pulley block 4) car 5) rail 6) universal joint 7) potentiometer mount 8) pitch potentiometer 9) heave potentiometer 10) drum 11) heave motor mount 12) heave motor 13) heave motor encoder 14) cable belt 15) pitch motor mount 16) pitch motor 17) pitch encoder 18) wire 19) foil 20) hull

The car could move laterally between the side pulley block and the center pulley block. The spacing between the side pulley block and the middle pulley block is 24.5 cm. The distance between the starting position of the two foils is .3048 m.

The motor proportional integral derivative (PID) gains were set using the MEI interface. The proportional was set first, then the derivative (set roughly twice the proportional), and a very small number for the integral gain.
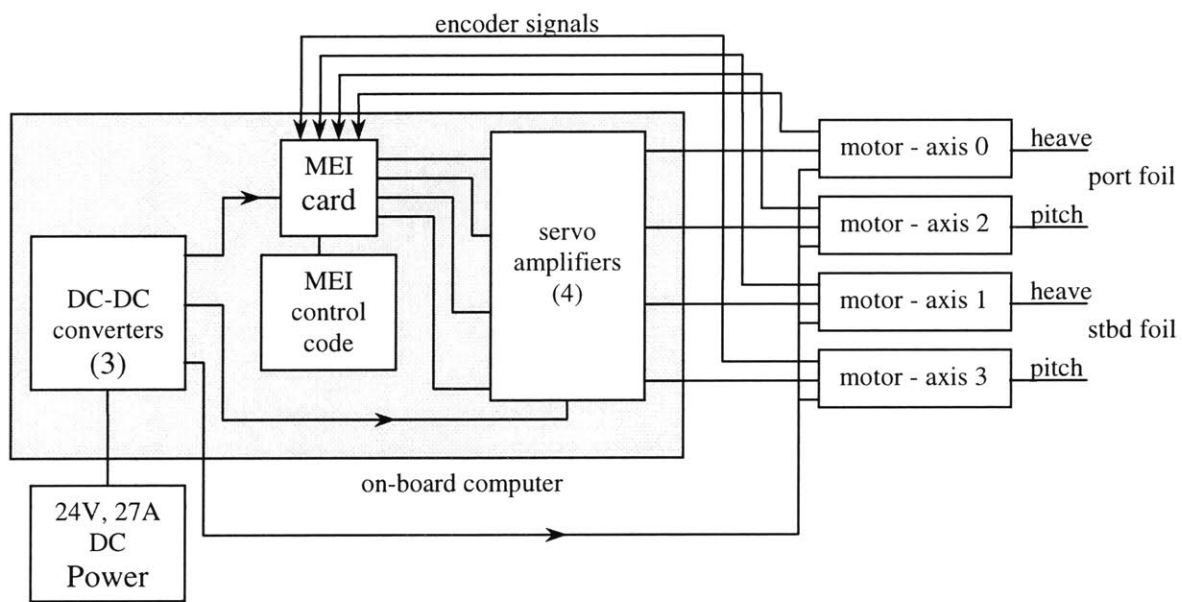

Figure 2-3: Schematic of motion control.

2.6.1 Foils

The two NACA 0012 shape foils were identically cut out of styrene foam by computer guided hot wire and reinforced with several layers of fiberglass. The span (length) of the foil is 17.5 cm and the chord (width) is 7.5 cm. The aspect ratio is 2.45, where aspect ratio is defined as: $AR = s^2/area$, where s is the span and area is the area of one side of the foil. Three holes at varying depths, 4.5 cm apart, were drilled for dye injection. Plastic tubing with inner diameter 1.6 mm was inserted and sealed with epoxy. Steel rods of 0.25 inch diameter were permanently affixed to the foils at the quarter chord point. For smoothness and the top coat, epoxy and black spray paint was used.
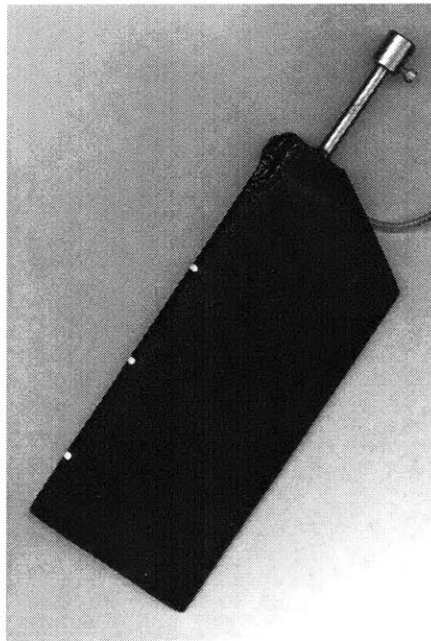

Figure 2-4: The white dots indicate the location of the dye ducts.

2.6.2 Operation

Through the use of the MEI software and system, the foils could heave and pitch precisely in a sinusoidal motion. Axes 0 and 2 were designated masters, whereas axes 1 and 3 were slaves. The slaves were programmed to copy their masters, but in the negative direction. The resulting motion was a symmetric sinusoidal oscillation of foils.

Although the foilboat mechanism mounted on the destroyer could be fully self-propelled, the velocity would not be steady therefore quantitative comparisons would be difficult. By attaching the destroyer to the carriage, the speed was always fixed and controlled.

2.7 Verifying Motion

The potentiometers were installed to serve as an external reference of foil position. They were powered by a 10 V DC power supply. The potentiometers for motor axes 0 and 1 (heave), Bourns series 6657 single-turn conductive plastic, were mounted on the drums, which are directly proportional to the distance in which the foils heave. Bourns series 3541H 10-turn hybrid potentiometers for axes 2 and 3 (pitch) were mounted on brackets, the potentiometer shaft connecting a sleeve coupling to a shaft at the universal joint. (From now on, they will be referred to as pot0, pot1, pot2, and pot3 for abbreviation.)

Because all of the potentiometers were attached to the respective motor shaft, they could be used to determine the position of the foils by relating the raw voltage outputted and the distance traveled. First, the potentiometers were permanently affixed in such a position that their voltage lied in the middle range such that the extremities of their range did not cause the potentiometer shaft to stop turning or a wraparound of voltage to occur. The calibration of pot0 and pot1 were done by commanding the motors to move 4000 counts which was one revolution of the shaft correlating to 50.5 mm. Because pot2 and pot3 were single-turn, the calibration would be thrown off if they exceed 10 V or go below 0 V. Motors 2 and 3 were commanded to move between ±1000 counts, essentially 180 degrees from the starting position, relating the voltage outputted from the potentiometers and the angle of pitch.

Once the calibration constants were obtained, there was a permanent relationship between voltage and position. During each run, the raw voltage was recorded on a bridge computer called Mahi Mahi and converted into position by taking the raw value, subtracting the initial offset, and multiplying by the calibration constant. Also, from the raw data, frequency and phase could be verified.

27

Pot	Calibration Constant
0	50.5 mm/V
1	50.5 mm/V
2	33.9 degrees/V
3	33.6 degrees/V

Table 2-1: Calibration of Potentiometers
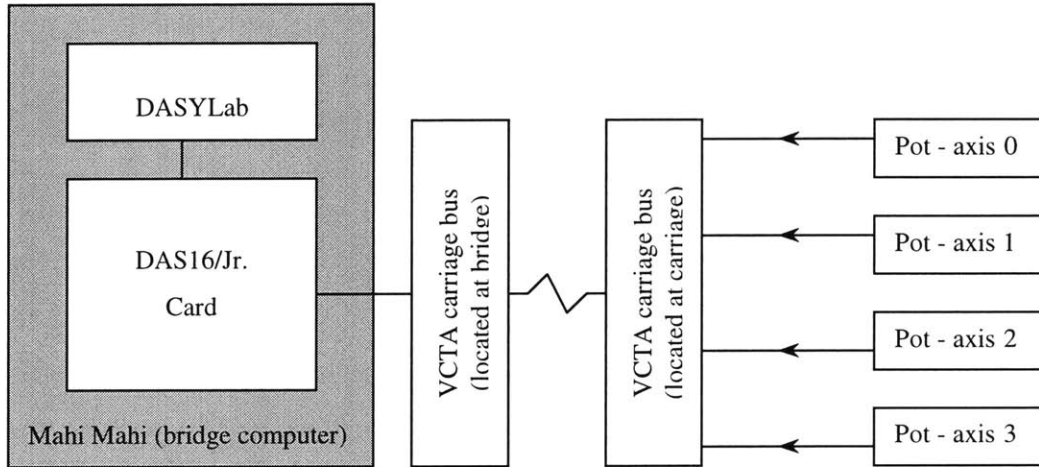
4 analog signal input
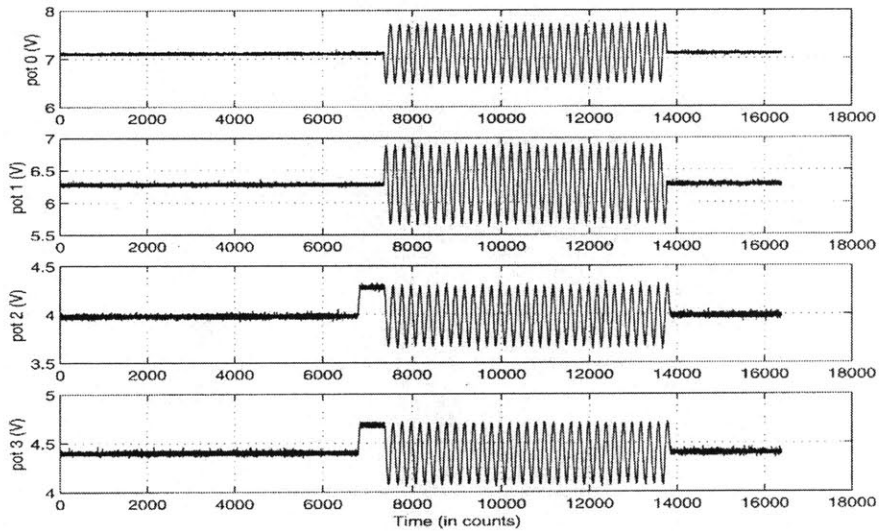
Figure 2-5: Schematic of Data Acquisition

Figure 2-6: Raw data from potentiometers.

2.8 Dye Set-Up

Foils with dye injection ports along the leading edge emitted tracer dye into the water. Fluorescent yellow green dye (Cole-Parmer Model #00298-07) was chosen as the tracer due its exceptional contrast in the water. The dye to water ratio used was 1:40. Air, from a 90 psi capacity tank, was used to drive the dye out of the reservoir at a regulated pressure of 20 psi. A black ultraviolet light hung directly above the foils (attached to the potentiometer mounts) illuminated the dye. This configuration caused a glare on the water surface by the leading edge and produced reflections from metallic parts of the mechanism, but the resulting images from this set-up outweighed the cons. To control dye injection, a switch from the bridge could be flipped on or off. The switch was connected through the bus to a DC relay to an AC solenoid valve which controlled flow of dye exiting the dye reservoir. The tube from the dye reservoir splits into two tubes, with each tube leading to a foil. Experiments were conducted in darkness.
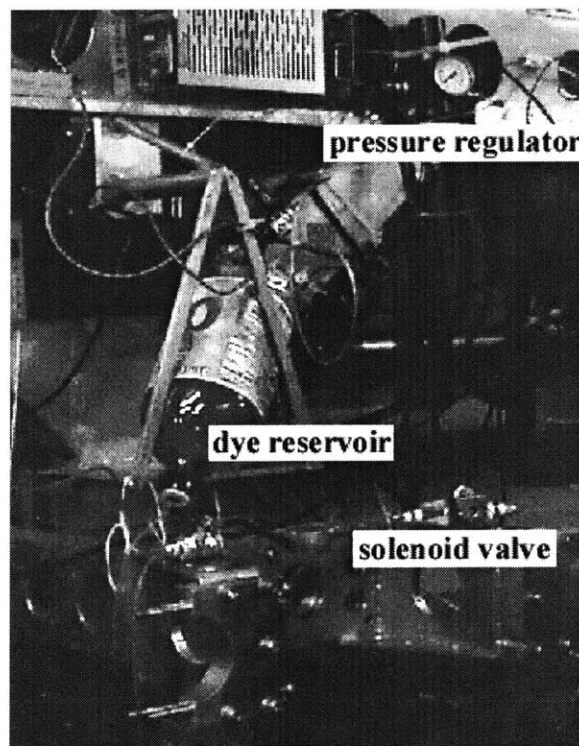

Figure 2-7: Dye Visualization Set-Up

2.9 Video/Digitizing

An aluminum strut, attached to the foilboat mechanism, held a color CCD camera in place 1 m from the water surface. The camera mount positioned the camera for a view of the near wake as the boat moves forward. The camera's field of vision was approximately 0.82 m at 1.2 m.
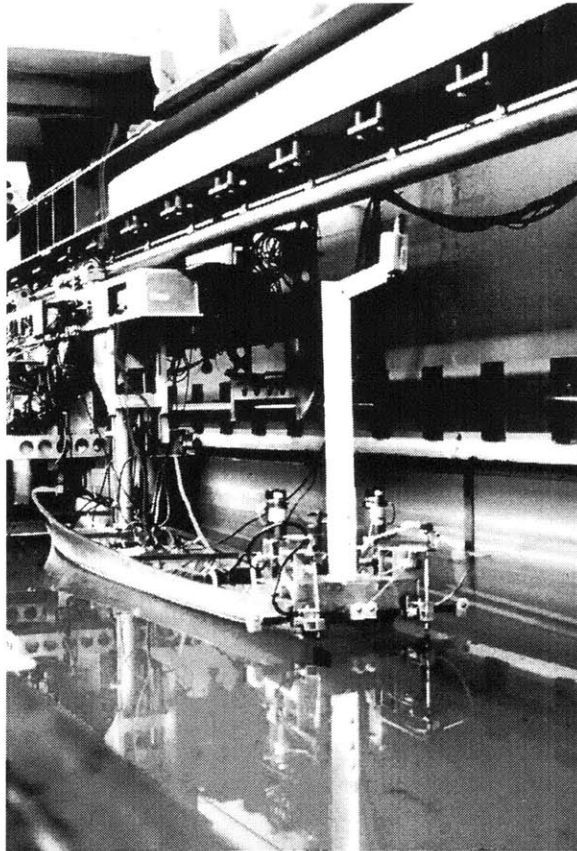

Figure 2-8: Camera mounted on the foilboat mechanism

While experiments progressed, a high quality VHS VCR recorded off of the camera. In order to convert the recorded video footage into still frames for quantification, the XCAP program made by EPIX, Inc. was used. This program streamed live video from a S-VHS VCR and captured it into its frame buffer at a maximum rate of 30 Hz. It had options of skipping a specified number of frames between screen captures. The captured images would be saved as .tif graphics format and later enhanced in Adobe Photoshop 5.0.

Chapter 3

Visualization Experiment

3.1 Test Matrix

Physical parameters that could be controlled by the motion controller include the heave amplitude (h), pitch amplitude (θ), frequency (f), and phase lag between pitch and heave(ϕ). By preselecting the testing speed of the carriage to be $U = 0.2$ m/s, the visualizations would come out cleaner because the dye would not disperse as quickly as if tests were run at higher speeds. Therefore, the chord Reynolds number was fixed at R_C= 15,000 and the ship length remained at R_L= 600,000. h was set at 57 mm, close to the maximum of operable flapping heave amplitude, therefore h/c was held constant at 0.76. For a smaller set of tests, the selections of testing parameters were narrowed to the variation of the maximum angle of attack, St. number, and phase.

To do a rough mapping of the parameter space, a sparse matrix was created for testing. For 90-degree phase lag of pitch to heave, the maximum angle of attack (α) ranged from 10° to 30°, in 5-degree increments, while the Strouhal number varied from 0.1 to 0.5. For phases of 70° and 110°, the testing space was more sparsely spaced, testing Strouhal numbers of 0.2, 0.3, and 0.4, while α varied in 10 degree increments from 10° to 30°.

To find the maximum angle of attack, a MATLAB program (referenced in Appendix A) was used. It required inputting the other parameters and it outputted the closest approximation of the angle of attack.

For some tests, α did not exist using certain parameters and therefore those tests were omitted. The numbers entered into the computer for heave, pitch, and phase had to

31

be integer values, only the frequency could be inputted as a float. Therefore the pitch angle was rounded to the nearest integer. The rounding of the pitch angle and other factors contribute up to an error of ± 5° in angle of attack.

Run #	α (°)	St. #	h (mm)	θ (°)	f (Hz)	φ (°)
1	10	0.1	57	7.45	0.175	90
2	15	0.1	57	2.29	0.175	90
3	10	0.2	57	22.35	0.351	90
4	15	0.2	57	17.19	0.351	90
5	20	0.2	57	12.03	0.351	90
6	25	0.2	57	6.88	0.351	90
7	30	0.2	57	2.29	0.351	90
8	10	0.3	57	33.81	0.526	90
9	15	0.3	57	28.08	0.526	90
10	20	0.3	57	23.49	0.526	90
11	25	0.3	57	18.34	0.526	90
12	30	0.3	57	13.18	0.526	90
13	10	0.4	57	45.26	0.702	90
14	15	0.4	57	37.82	0.702	90
15	20	0.4	57	31.51	0.702	90
16	25	0.4	57	26.36	0.702	90
17	30	0.4	57	21.77	0.702	90
18	10	0.5	57	56.15	0.877	90
19	15	0.5	57	46.98	0.877	90
20	20	0.5	57	39.53	0.877	90
21	25	0.5	57	33.23	0.877	90
22	30	0.5	57	27.5	0.877	90
23	10	0.2	57	31.51	0.351	70
24	20	0.2	57	13.75	0.351	70
25	10	0.3	57	44.12	0.526	70
26	20	0.3	57	32.66	0.526	70
27	30	0.3	57	14.99	0.526	70
28	20	0.4	57	54.43	0.702	70
29	30	0.4	57	27.5	0.702	70
30	10	0.2	57	23.49	0.351	110
31	20	0.2	57	13.18	0.351	110
32	30	0.2	57	2.29	0.351	110
33	10	0.3	57	35.52	0.526	110
34	20	0.3	57	24.64	0.526	110
35	30	0.3	57	14.32	0.526	110
36	10	0.4	57	44.12	0.702	110
37	20	0.4	57	33.23	0.702	110
38	30	0.4	57	22.92	0.702	110

Table 3-1: Foil parameters for dye visualizations

3.2 Experimental Method

Dye was released when the boat accelerated to $U = 0.2$ m/s and when the foils reached a steady state of flapping. At least 6 cycles of each run were recorded on video before stopping the dye injection. The amount of dye injected into the water was kept as low as possible to maintain visibility and prevent early saturation.

The pictures were selected so that approximately one cycle of each run could be shown in 10 frames. In order for this to happen, a calculated number of frames was omitted for each set of St. numbers. Select frames and examples were chosen to illustrate certain phenomena. All of the experiments conducted were digitized, processed and referenced in Appendix B. The distortion due to the camera was ignored, as the effects were assumed to be insignificant.

St. #	Number of frames skipped	Δt (s)
.1	19	.633
.2	10	.333
.3*	7	.233
.4	5	.167
.5	4	.133

* Occasionally, 6 frames were omitted, Δt of .2 seconds.

Table 3-2: Number of frames omitted during screen captures and the corresponding times between frames

As seen in Figure 3-1, the wake dynamics behind the destroyer and flapping foils is extremely complex.
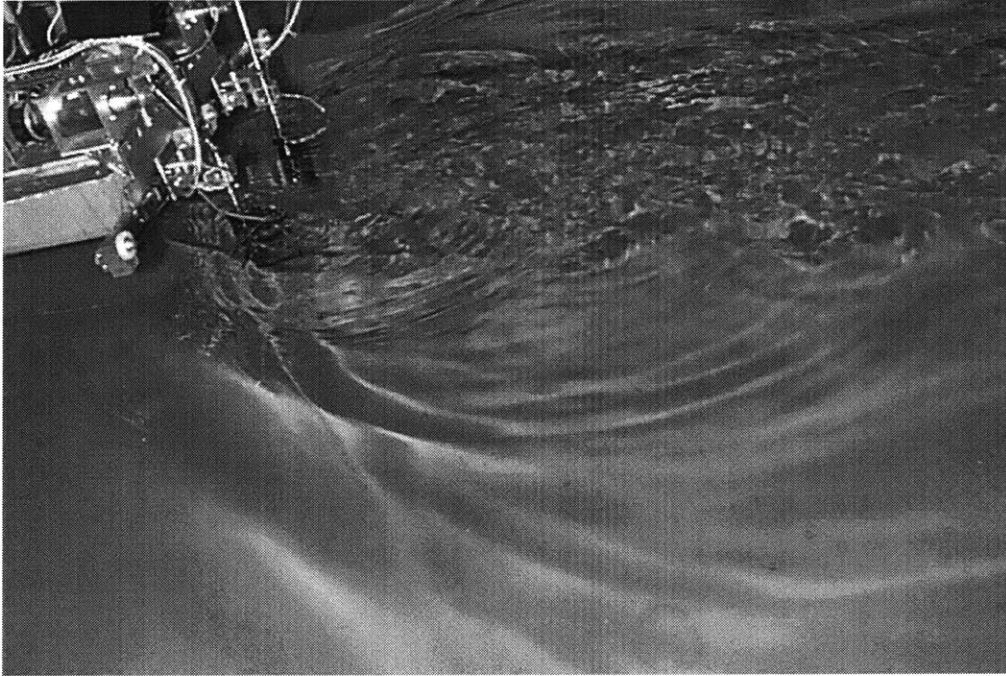
Figure 3-1: Wake of flapping foils with dye injection.

(Picture was taken in darkness.)

Chapter 4

Analysis

The video was transferred into digitized images, similar to the image below. Raw images were then processed by tuning the contrast, adjusting the color, and cropping the image. Unfortunately, because the lighting came from black light above the stern, the vortices that moved downstream are not easily visible. Also, a glare is seen between the foils, which interferes with tracking the progression of dye coming off of the foil. Cropping the picture left a visible area of 0.4 m by 0.55 m, approximately 0.1 m downstream of the leading edge of the foils, rid the image of glare.
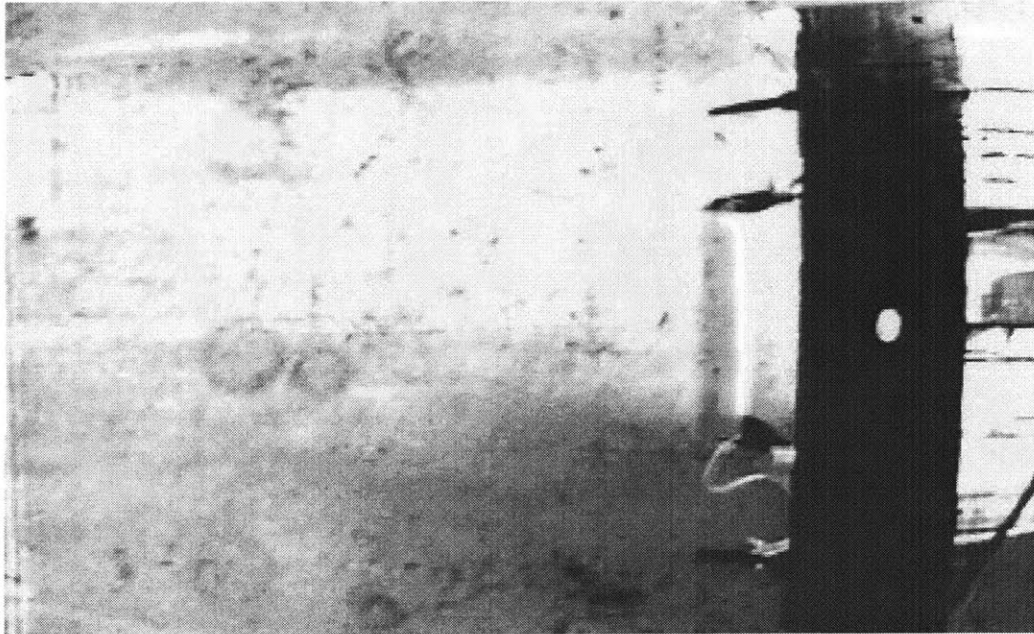
Figure 4-1: Digitized image from the video (prior to cropping).

A good portion of analysis of the images is subjective, using experience to classify the characteristics of the wake. Whereby possible for each run, the wake type was classified, the characteristic wavelength measured, the width of each foil wake

recorded, the distances and angle between distinctive vortices noted, and the wake interaction observed. All measurements have estimated error margins. When an image is not clear, the error margin was increased.

To measure the distance between vortices, the digitized images were processed and measured using the ruler tool in Photoshop. The ruler tool can accurately measure the length and width components and the angles between vortices. The distances were normalized to the foil chord length.

The port (top) side was selected for measurement because of its clarity and ease of identification. The assumption is that the foils oscillate symmetrically and therefore give precise values from the port side.

4.1 Wavelength and Wake Width

The wavelength can be computed directly from linear theory $\lambda = U/f$ where U is the free stream velocity and f is the frequency. Using this method of obtaining the wavelength means that it is independent of α and ϕ. Another method of finding the wavelength is by measuring it from the digitized pictures. The characteristic wavelength was especially difficult to estimate. It was rare that an entire cycle was illuminated at once, especially at the lower Strouhal numbers, where the periods were long. From Figures 4-2 and 4-3, in general, the measured wavelength is longer than suggested by linear theory.

For Table 4-1, the wake width is the spread of the port foil wake. The maximum separation is measured between the outermost dye traces, which indicates the total width of the foil and boat wakes.

The wake width increases proportionally to phase. The larger the Strouhal number, the larger the wake width, and the smaller the wavelength. At a Strouhal number of 0.4, the maximum separation is proportional to the phase. The maximum separation is greater than twice the wake width at Strouhal numbers of 0.1 to 0.3 and is less than two times the wake width at 0.4 and 0.5.

36

Figure 4-2: λ/c vs. St. #, φ = 90°
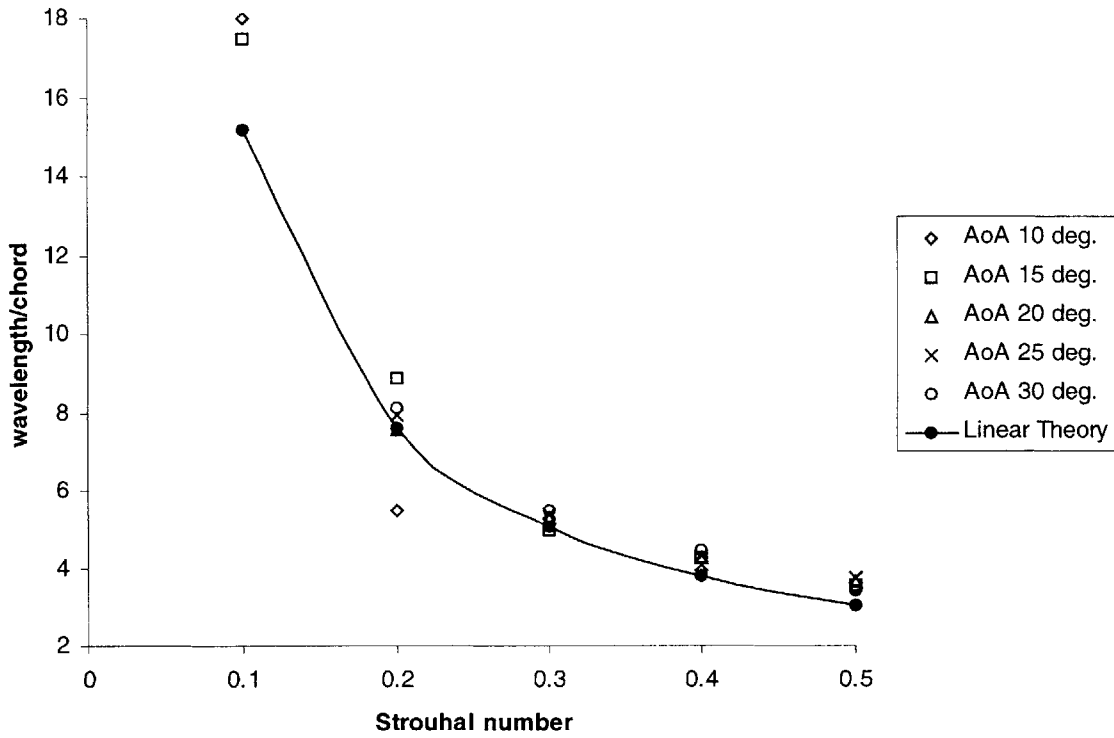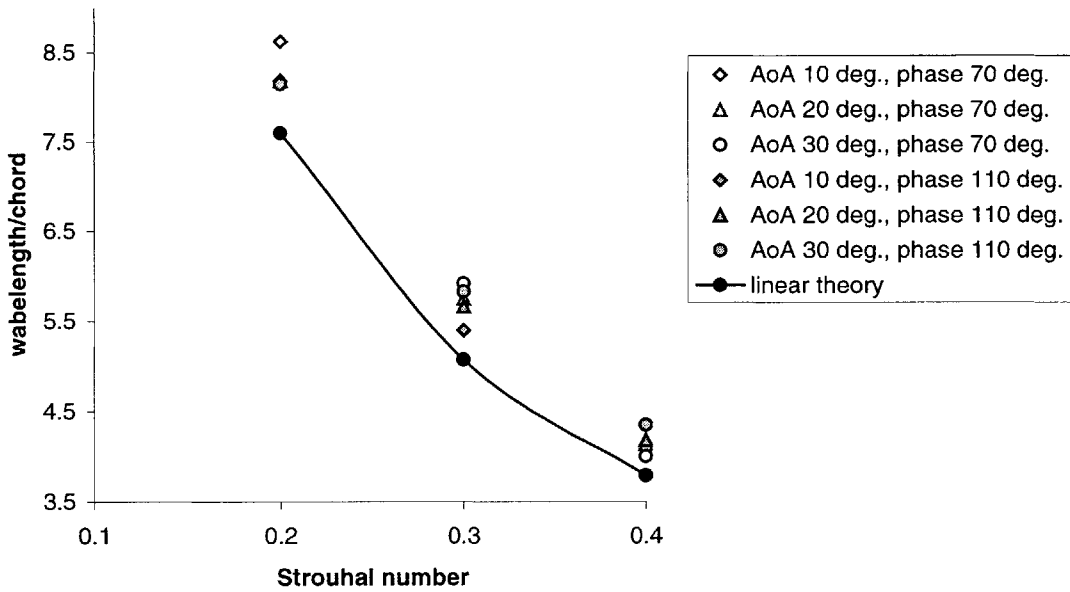
Figure 4-3: λ/c vs. St. #, φ = 70° and 110°

Run #	α (°)	St. #	φ (°)	wave-length	Measured wavelength		wake width		maximum separation	
1	10	0.1	90	15.2	18.02	± 0.09	2.22	± 0.04	5.36	± 0.13
2	15	0.1	90	15.2	17.50	± 0.44	2.57	± 0.22	5.92	± 0.17
3	10	0.2	90	7.6	5.49	± 1.89	3.35	± 0.34	6.75	± 0.30
4	15	0.2	90	7.6	8.88	± 0.17	3.05	± 0.09	6.49	± 0.22
5	20	0.2	90	7.6	7.58	± 0.26	2.92	± 0.13	6.27	± 0.35
6	25	0.2	90	7.6	7.92	± 0.26	3.18	± 0.13	7.23	± 0.26
7	30	0.2	90	7.6	8.10	± 0.26	3.70	± 0.22	7.05	± 0.09
8	10	0.3	90	5.07	5.31	± 0.09	3.35	± 0.22	6.88	± 0.44
9	15	0.3	90	5.07	4.96	± 0.09	3.40	± 0.26	6.53	± 0.09
10	20	0.3	90	5.07	5.31	± 0.09	3.31	± 0.17	6.62	± 0.35
11	25	0.3	90	5.07	5.40	± 0.35	3.00	± 0.22	6.27	± 0.17
12	30	0.3	90	5.07	5.49	± 0.26	3.31	± 0.17	6.62	± 0.17
13	10	0.4	90	3.79	3.92	± 0.09	3.61	± 0.04	7.10	± 0.04
14	15	0.4	90	3.79	4.27	± 0.09	3.48	± 0.17	6.88	± 0.26
15	20	0.4	90	3.79	4.27	± 0.09	3.31	± 0.17	6.70	± 0.09
16	25	0.4	90	3.79	4.31	± 0.13	3.53	± 0.04	6.70	± 0.09
17	30	0.4	90	3.79	4.44	± 0.09	3.61	± 0.04	7.05	± 0.09
18	10	0.5	90	3.04	3.44	± 0.04	4.22	± 0.04	7.88	± 0.04
19	15	0.5	90	3.04	3.57	± 0.09	3.66	± 0.17	7.14	± 0.35
20	20	0.5	90	3.04	3.66	± 0.17	3.7	± 0.04	7.23	± 0.09
21	25	0.5	90	3.04	3.74	± 0.09	3.48	± 0.17	6.79	± 0.17
22	30	0.5	90	3.04	3.40	± 0.09	3.74	± 0.09	7.05	± 0.26
23	10	0.2	70	7.6	8.62	± 0.26	2.31	± 0.04	5.27	± 0.04
24	20	0.2	70	7.6	8.18	± 0.17	3.13	± 0.17	6.62	± 0.17
25	10	0.3	70	5.07	5.40	± 0.17	2.57	± 0.13	5.36	± 0.04
26	20	0.3	70	5.07	5.75	± 0.17	2.83	± 0.13	5.36	± 0.04
27	30	0.3	70	5.07	5.92	± 0.35	3.53	± 0.04	6.92	± 0.13
28	20	0.4	70	3.79	4.14	± 0.04	3.09	± 0.13	6.18	± 0.09
29	30	0.4	70	3.79	4.01	± 0.35	3.22	± 0.09	6.36	± 0.09
30	10	0.2	110	7.6	8.18	± 0.17	3.44	± 0.04	6.36	± 0.09
31	20	0.2	110	7.6	8.18	± 0.17	3.4	± 0.09	6.36	± 0.09
32	30	0.2	110	7.6	8.14	± 0.13	3.44	± 0.04	6.88	± 0.26
33	10	0.3	110	5.07	5.40	± 0.17	3.61	± 0.04	7.05	± 0.09
34	20	0.3	110	5.07	5.66	± 0.09	3.74	± 0.09	6.79	± 0.17
35	30	0.3	110	5.07	5.83	± 0.09	3.92	± 0.09	7.14	± 0.17
36	10	0.4	110	3.79	4.35	± 0.17	4.09	± 0.26	7.75	± 0.26
37	20	0.4	110	3.79	4.18	± 0.17	3.7	± 0.04	7.18	± 0.04
38	30	0.4	110	3.79	4.35	± 0.17	3.74	± 0.26	7.23	± 0.26

*Distances are normalized by the chord length (.075 m).

Table 4-1: Wavelength by Linear Theory, Measured Wavelength, Foil Wake Width, and Maximum Separation

4.2 Wake Structure Classification

While running experiments through this parameter space, wakes exemplified unique characteristics and were classified into several categories. Some of these wakes were placed under the same category even though they have other notable differences. It was decided that five categories would suffice to describe all of the wake patterns observed. Certain runs showed strong characteristics from more than one type of wake and thus were classified with both. Table 4-2 shows pieced-together runs of these formations. Much of the classification was done after viewing the video multiple times to determine in which directions vortices spin.

In type A wake, there was no noticeable vortex formation. Dye traced the foils' sinusoidal paths as they cut through the water. This occurred when the Strouhal number was small.

The type B wake had vortex formations in the form of shear layer instabilities. The pattern resembled type A with additional small vortical disturbances. In the image, along the trace, the dye looked globular where there were little vortices.

Type C wake had 4 vortices per cycle. The mushroom formations were similar to the "2P" formation that Williamson and Roshko [19] described. In general, these formations were angled downstream. Further description and analysis on these formations is included in the Discussion portion of this thesis.

Type D had characteristic large elongated loops and usually multiple distinct vortices convecting. The vortices traveled faster outward and inward than downstream. The assumption was that time did not allow for the vortices to convect downstream. Some of these wakes also underwent a ballooning effect. The vortices were located in various positions along the loop, but convected outwards from the "center." Depending on how strong the individual vortices were, the resultant shape of the loop varied. The C-D type had the shape of the D type wake, but with only one pair of vortices like that of the C type. The B-D type resembled D but had many shear layer instabilities.

The type E wake was unique. The flow resembled a pseudo Kármán vortex street, but the vortices were disorganized, making it difficult to determine the direction of spin. The B-E type followed the general form of E type, but also has shear layer vortices.

39
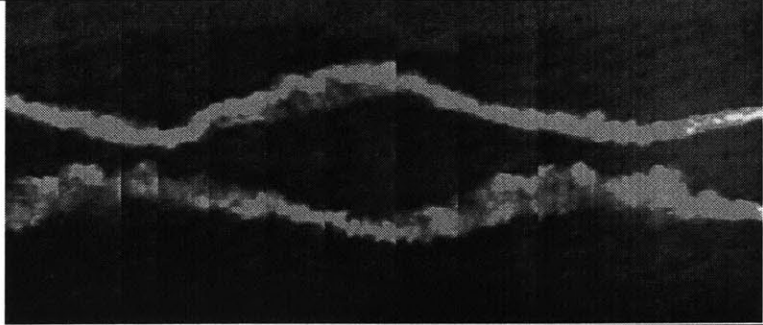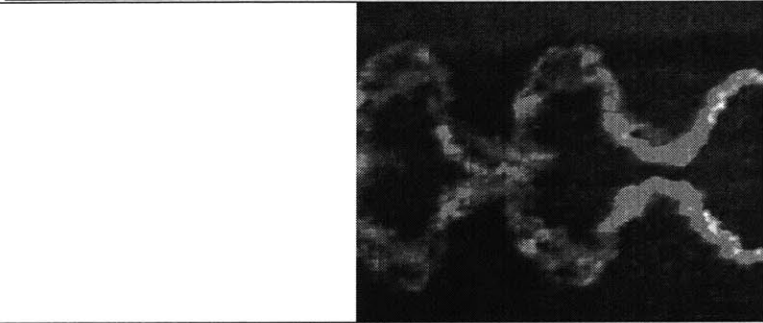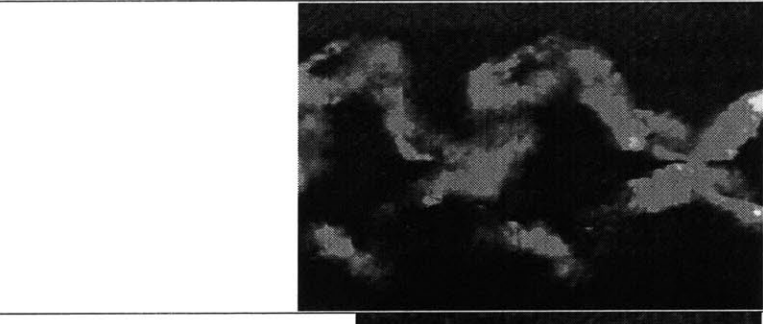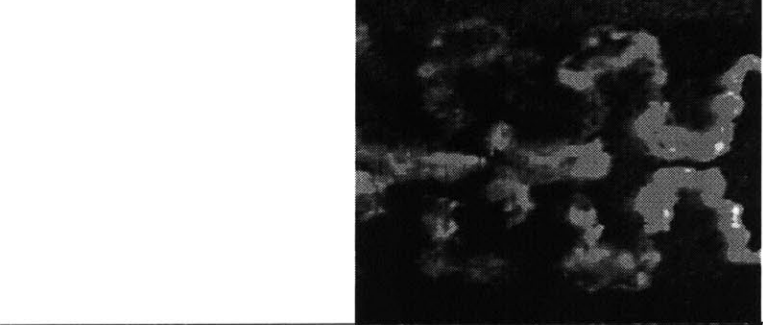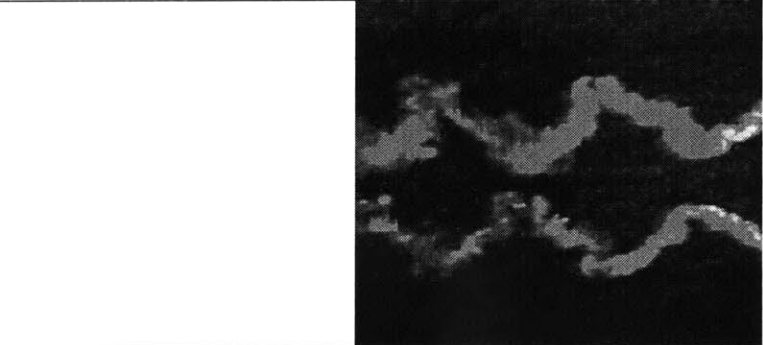
Type A	
Type B	
Type C	
Type D	
Type E	

Table 4-2: Classification of Wakes (direction of flow is right to left)

Max AoA — Phase 90°

Max AoA	.1	.2	.3	.4	.5
30		C	C-D	C-D	C-D
25		C	D	C-D	C-D
20		B-C	D	D	D
15	A	B	B-D	D	D
10	A	B	B	D	D

Max AoA — Phase 70°

Max AoA	.2	.3	.4
30		C-D	C-D
20	C	B-E	B-E
10	A	B-E	

Max AoA — Phase 110°

Max AoA	.2	.3	.4
30	C	C-D	C-D
20	B-C	D	D
10	B	B-D	D

Table 4-3: Characteristic Wakes – Vortex Formations of Experiments

The mapping of parameter space at phase 90° seems to be covered sufficiently to see a semblance of a transition border between regimes. Repeated trials of the wake structures shared the same patterns.

Phase 70° experiments, in general, were not classified under the same wake categories as phase 90°. It would be interesting to note that the 110° runs were almost all identically classified to the phase 90° ones. Upon comparing the actual pictures, there were notable differences, one being that 110° runs had loops with greater angled vortices.

The type A formation occurred at low Strouhal numbers, where the disturbance was relative small. The wakes were mostly of type C and D. The E type wake was almost an anomaly, but repeated runs show the same occurrence. Higher Strouhal number runs were of type D formation. The C type formations only appeared in maximum angle of attack runs of 20° or higher.

4.3 Characteristic Vortex Separation

To determine the distance from one vortex to another, two frames were selected to represent each run. One frame focused on the top vortices and one on the bottom ones. The frame was chosen such that a quarter of the following wavelength showed, thereby selecting frames consistently approximately at the time spacing between. The images in Figure 4-4 were typically chosen for measurements.
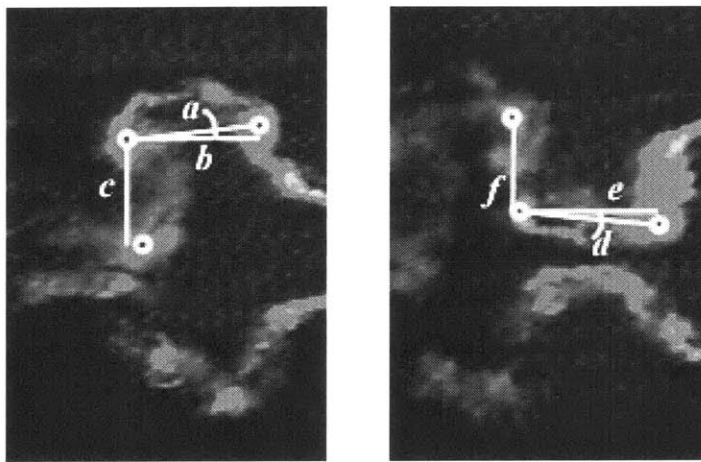
Figure 4-4: Typical images selected for vortical spacing processing.

In Table 4-4, each measurement related to the vortices was given a letter (and drawn on Figure 4-4):

> a is the angle between the outer vortices;
> b is the distance between outer vortices;
> c is the distance between outer and inner vortices;
> d is the angle between the inner vortices;
> e is the distance between inner vortices; and
> f is the distance between inner and outer vortices.

Vortex spacing is one of the more subjective areas of analysis. It is difficult to determine where one vortex begins, where it has traveled, where to pinpoint its center, etc. When encountering these issues, an approximation was made as well as an estimate of the error.

First, using Photoshop's ruler, a vortex's center was pinpointed and selected on the image. Then it was measured to the corresponding vortex's vertical or horizontal projection. The distance obtained was scaled and normalized by the chord length. The angle between the vortices was measured from one vortex's center to another. The same process was repeated by hand, using a protractor and ruler. The two values were averaged. Half the difference of the two values were added as an error margin. The same images were measured, therefore the error was not expected to be large. It would have been more accurate to compare multiple cycles. This process was not done due to the extensive data collection required. However, extra consideration was taken to select a typical or normal cycle for digitization. Some experiments did not generate vortices, therefore those runs did not have any numbers listed for them.

At a Strouhal number of 0.2 and high angles of attack, both *b* and *d* were higher than other parameters. This data regarding the vortical spacing agrees with Freymuth's statement that as reduced frequency decreases, the distance between vortices increases, due to the sluggish rollup [5]. In most of the runs where vortex spacing was obtainable, *a* was positive and *d* was negative, which indicated that the mushroom formation slanted downstream.

Run #	α (°)	St. #	φ (°)	a	b	c	d	e	f
1	10	0.1	90						
2	15	0.1	90						
3	10	0.2	90						
4	15	0.2	90						
5	20	0.2	90						
6	25	0.2	90	16 ± 2	3.49 ± 0.08	1.00 ± 0.22	-9 ± 2	3.70 ± 0.04	1.61 ± 0.13
7	30	0.2	90	11 ± 1	3.83 ± 0.01	1.70 ± 0.22	-6 ± 1	3.63 ± 0.06	1.92 ± 0.70
8	10	0.3	90						
9	15	0.3	90	9 ± 2	1.85 ± 0.46	1.92 ± 0.17	-9 ± 1	2.55 ± 0.07	1.74 ± 0.09
10	20	0.3	90	5.5 ± 1.5	2.48 ± 0.04	1.83 ± 0.09	-6.5 ± 0.5	1.95 ± 0.04	1.65 ± 0.09
11	25	0.3	90	13 ± 3	2.71 ± 0.07	3.22 ± 0.09	-9.5 ± 1.5	2.73 ± 0.12	0.96 ± 0.09
12	30	0.3	90	18.5 ± 3.5	2.78 ± 0.18	1.70 ± 0.39	-15.5 ± 3.5	3.13 ± 0.01	1.92 ± 0.09
13	10	0.4	90	19.5 ± 1.5	1.92 ± 0.09	2.31 ± 0.13	-12.5 ± 1.5	2.10 ± 0.01	1.83 ± 0.44
14	15	0.4	90	21 ± 1	2.04 ± 0.05	1.13 ± 0.09	-12 ± 1	2.06 ± 0.03	2.00 ± 0.09
15	20	0.4	90	22.5 ± 2.5	1.83 ± 0.08	1.31 ± 0.09	-11 ± 1	1.91 ± 0.01	1.96 ± 0.04
16	25	0.4	90	12 ± 2	2.21 ± 0.03	2.05 ± 0.13	-11.5 ± 1.5	2.65 ± 0.05	2.18 ± 0.09
17	30	0.4	90	5.5 ± 2.5	2.25 ± 0.01	2.13 ± 0.13	-6.5 ± 2.5	2.17 ± 0.01	1.39 ± 0.35
18	10	0.5	90	-8 ± 2	2.37 ± 0.19	2.48 ± 0.13	-21.5 ± 2.5	2.06 ± 0.03	2.18 ± 0.09
19	15	0.5	90	11 ± 1	1.98 ± 0.19	2.00 ± 0.09	-17 ± 2	2.29 ± 0.03	2.70 ± 0.09
20	20	0.5	90	22.5 ± 1.5	1.96 ± 0.05	1.70 ± 0.13	8.5 ± 0.5	1.72 ± 0.02	2.70 ± 0.09
21	25	0.5	90	11.5 ± 2.5	2 ± 0.09	1.83 ± 0.09	2 ± 2	1.91 ± 0.01	2.52 ± 0.09
22	30	0.5	90	10 ± 2	1.92 ± 0.17	2.26 ± 0.09	-4 ± 2	2.20 ± 0.11	2.52 ± 0.09
23	10	0.2	70						
24	20	0.2	70	5.5 ± 3.5	2.95 ± 0.1	1.61 ± 0.13	-2.5 ± 1.5	3.38 ± 0.07	2.09 ± 0.09
25	10	0.3	70						
26	20	0.3	70						
27	30	0.3	70	15.5 ± 1.5	2.5 ± 0.11	1.96 ± 0.13	-9 ± 1	3.05 ± 0.08	1.74 ± 0.17
28	20	0.4	70						
29	30	0.4	70	14 ± 4	1.96 ± 0.05	1.92 ± 0.09	-18 ± 2	2.01 ± 0.35	1.48 ± 0.09
30	10	0.2	110						
31	20	0.2	110						
32	30	0.2	110	12.5 ± 2.5	1.91 ± 0.08	2.26 ± 0.17	-2.5 ± 2.5	3.07 ± 0.06	2.44 ± 0.17
33	10	0.3	110	7 ± 1	2.36 ± 0.08	2.26 ± 0.17	-3.5 ± 1.5	3.21 ± 0.08	2.70 ± 0.09
34	20	0.3	110	13.5 ± 3.5	2.43 ± 0.17	1.83 ± 0.09	-9 ± 3	3.09 ± 0.04	2.18 ± 0.09
35	30	0.3	110	6.5 ± 1.5	2.34 ± 0.34	1.83 ± 0.09	-5.5 ± 1.5	2.32 ± 0.40	2.18 ± 0.09
36	10	0.4	110	23 ± 2	1.89 ± 0.02	2.35 ± 0.09	1.5 ± 1.5	2.98 ± 0.02	3.05 ± 0.09
37	20	0.4	110	19 ± 1	2.13 ± 0.14	1.87 ± 0.13	-8 ± 1	2.90 ± 0.06	2.66 ± 0.13
38	30	0.4	110	22 ± 2	2.21 ± 0.14	1.96 ± 0.13	-8 ± 2	2.71 ± 0.01	2.44 ± 0.09

These are values obtained from the upper wake or the port wake.
*Distances are normalized by the chord (.075 m).

Table 4-4: Vortex Spacing

4.4 Wake Interaction

Each run conducted was examined for wake interaction between the two streets generated from the foils. The use of the video was extremely useful for these comparisons. The experiments were categorized into "no," "some," and "yes" wake interaction.

"No" means no observable wake interaction. The two foil wakes are far apart and do not touch. "Some" means that the wakes from both foils do interact but do not interfere. The flow does not appear to be disturbed by the contact.

'Yes' means that there was strong wake interaction. The video showed runs where the inner mushroom formations from both flapping foils collide with each other causing water to shoot out both in the upstream and downstream directions. When the water is accelerated in the upstream direction, drag is produced. At the same time, a jet is created downstream of the drag. It would be interesting to determine whether strong wake interaction causes an overall negative effect.

Figure 4-5: Example of wake interaction

In this series of five images, the wake interaction is strong. The collision of the vortices caused a large blob of dye to eject backwards toward the boat.

The following trends were noted:

- 110° phase angle runs have strong wake interaction
- as the Strouhal number and angle of attack increase, the wake interaction increases

45

Runs 13 and 14 were exceptions to the observed trend because they had small angles of attack, yet had strong wake interactions.

Run #	α (°)	St. #	φ (°)	wake interaction
1	10	0.1	90	no
2	15	0.1	90	no
3	10	0.2	90	no
4	15	0.2	90	no
5	20	0.2	90	no
6	25	0.2	90	no
7	30	0.2	90	some
8	10	0.3	90	some
9	15	0.3	90	some
10	20	0.3	90	some
11	25	0.3	90	some
12	30	0.3	90	some
13	10	0.4	90	yes
14	15	0.4	90	yes
15	20	0.4	90	some
16	25	0.4	90	some
17	30	0.4	90	some
18	10	0.5	90	yes
19	15	0.5	90	yes
20	20	0.5	90	yes
21	25	0.5	90	yes
22	30	0.5	90	yes
23	10	0.2	70	no
24	20	0.2	70	some
25	10	0.3	70	no
26	20	0.3	70	no
27	30	0.3	70	yes
28	20	0.4	70	no
29	30	0.4	70	some
30	10	0.2	110	some
31	20	0.2	110	some
32	30	0.2	110	some
33	10	0.3	110	yes
34	20	0.3	110	yes
35	30	0.3	110	yes
36	10	0.4	110	yes
37	20	0.4	110	yes
38	30	0.4	110	yes

Table 4-5: Wake Interaction

46

4.5 Other Observed Phenomena

Through repeated observations of the video, other phenomena were noted such as: colliding vortices, leading edge separation, merging vortices, three-dimensional effects, and multiple vortices per cycle. Though these were not quantified, recording that these exist may aid in designing future experiments.

4.5.1 Colliding Vortices

At higher St. numbers, colliding vortices were visible. It occurred because there was not sufficient time for the vortices to convect downstream. Wake interaction from the inner vortices from port and starboard sides hit each other hard causing a characteristic wake to form from the upstream vortices while a jet was created by the downstream vortices. The inner downstream vortex from one mushroom formation collided into the inner upstream vortex in the mushroom formation further downstream. The vortices were in opposite directions, which signified that they would induce velocities in the outward direction. However, because the action was downstream and the dye had dispersed significantly, it was difficult to confirm what occurred visually.

4.5.2 Leading Edge Separation

During an experiment where the black light was left off, the foilboat was towed by the tank window with a black light source. The lights were permanently hung along the tank windows, which lined the last third of the tank length. They were located beneath the water line therefore not leaving a glare by the oscillating foils. The UV lights from the tank windows were not used in experiments originally because they were very weak and provided sufficient illumination for the port side of the foilboat only. From this run, leading edge separation was observed. Foils were added to the images to highlight the foil heave position, which was estimated from watching the video.
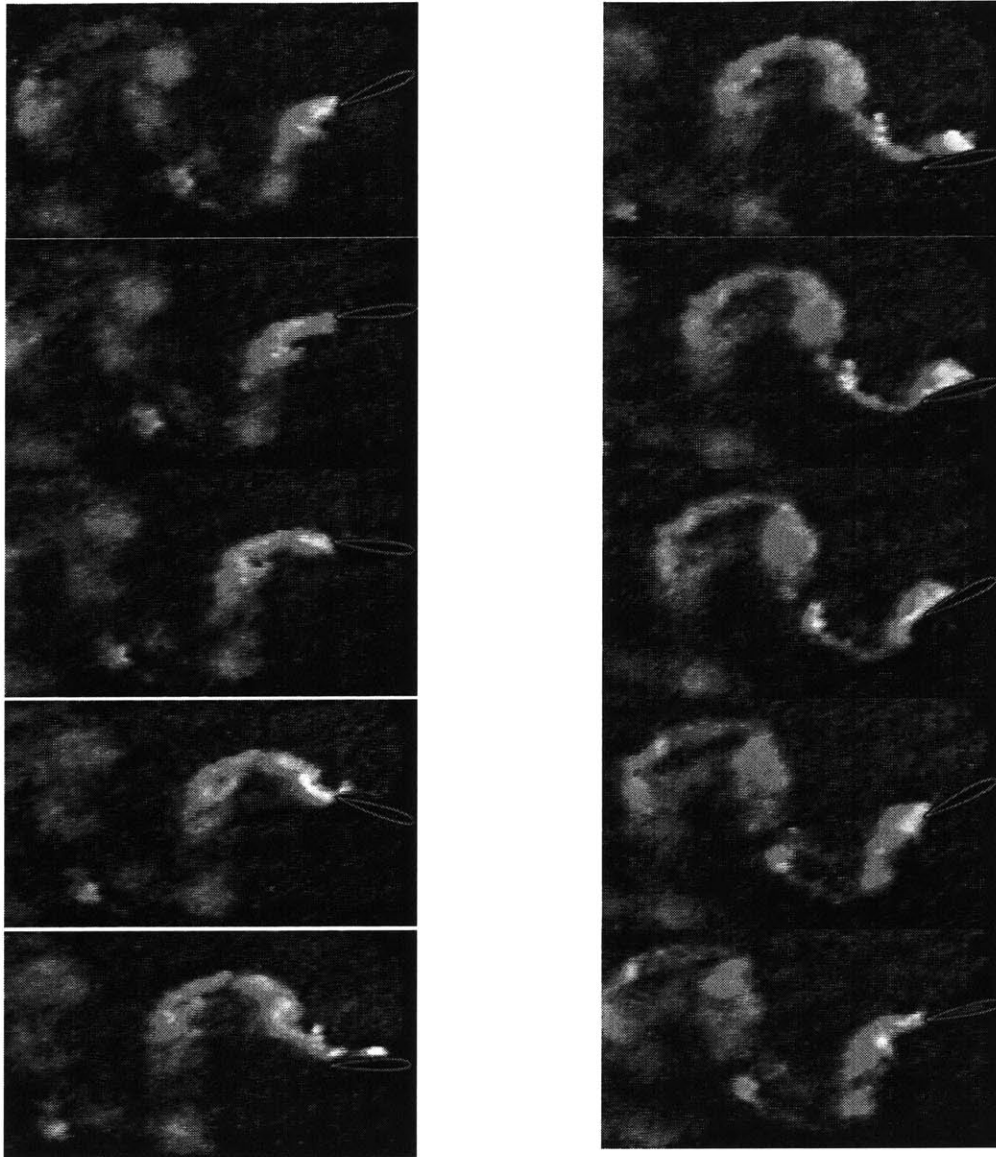
Figure 4-6: Visualization of dynamic stall vortex and trailing edge vortex rolling off of the port foil.

According to air foil experiments performed by Panda and Zaman [14], the dynamic stall vortex (DSV or leading edge vortex) is shed before the trailing edge vortex (TEV), and then they both move upwards in the positive y direction. This occurred when the reduced frequency $k = 0.8$ and in this particular run, $k = 0.83$. The convection of vortices outward could be seen.

4.5.3 Merging Vortices

In Figure 4-7, a vortex could be seen merging with another vortex of the same sign. Half a cycle later in Figure 4-8, the vortex appears to split. This is indicative of three-dimensional flow, which can make them appear to separate. The time step between these images is $\Delta t = 0.133$ s and the sequence is continuous from one sequence to another. The arrows point to the area of interest.
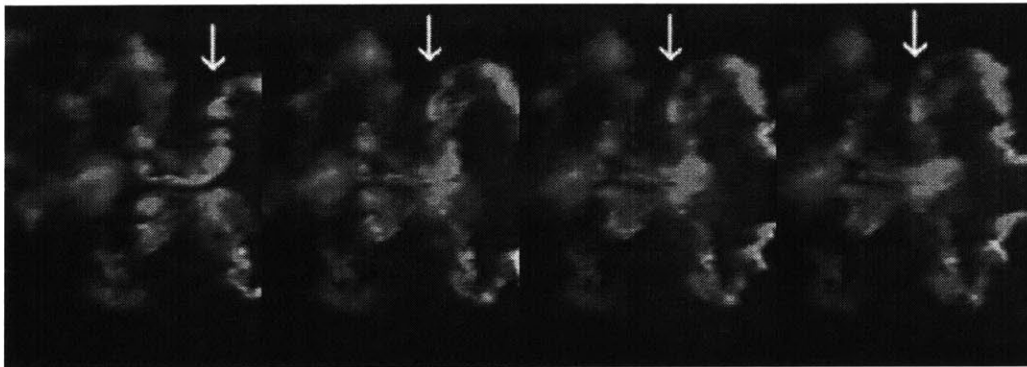
Figure 4-7: Merging Vortices
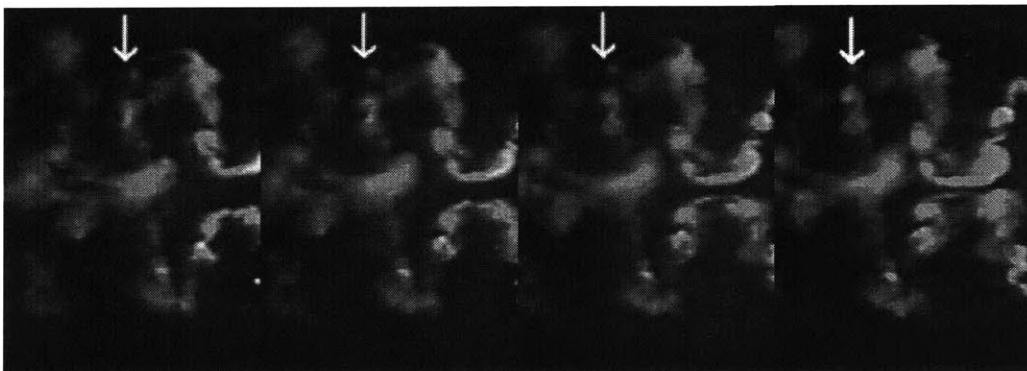
Figure 4-8: Vortices that appear to split.

4.5.4 Three-Dimensional Effects

The dye fluid trace surrounding the dye ports on the foils showed that the flow around the foils was not uniform. Three-dimensional effects could be seen in the lower Strouhal

number experiments. From the camera view, there should only be two traces in the water. However, the deeper dye traces dispersed in the outward direction.
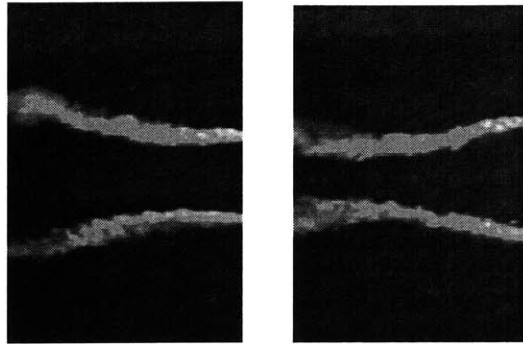
Figure 4-9: Dye traces show 3-D effects.

4.5.5 Multiple Vortices Per Cycle

In runs with the D type wake structure, there were generally 4 or more vortices within the convecting loop. Loose vortex filaments were visibly connecting the vortices. The vortices were separate entities, not ready to coalesce. Koochesfahani reported encountering six vortices per cycle [10] and Anderson stated that multiple vortices are related to shear layer instability [2]. Typical experiments with multiple vortices occurred at Strouhal numbers of 0.3 or greater, maximum angle of attack of 20° or less, and phase angle of 90° and 110°, as shown in Figure 4-10.
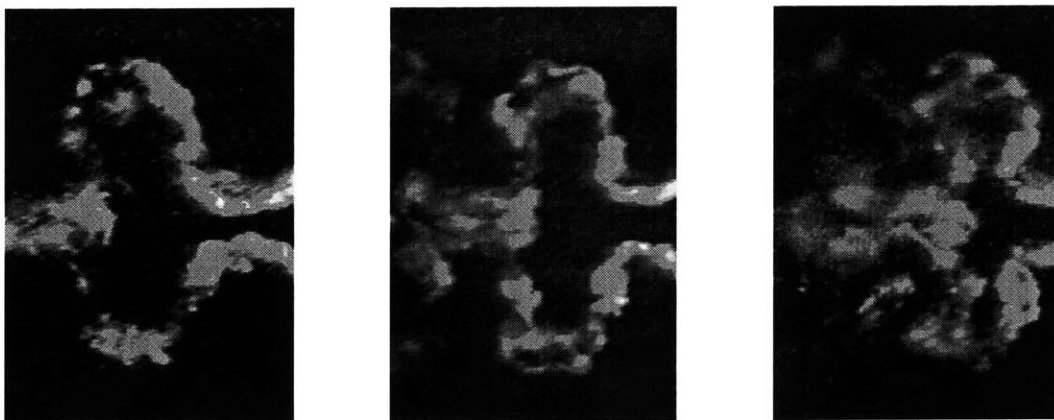
Figure 4-10: Three runs with multiple vortices per cycle.

4.6 Discussion

4.6.1 Vortex Pairing

According to Gopalkrishnan, vortex pairing was the most sensitive and difficult to reproduce in his cylinder-foil vortex interaction experiments. Unlike Gopalkrishnan, much of the obtained results of the flapping foilboat runs consist of vortex pairing. The mushroom formations in type C wakes convected out from both foil wakes in a similar fashion to Gopalkrishnan's vortex pairing mode. Unfortunately, the vortices spinning from the destroyer's wake were not visible before reaching the leading edge of the foils.
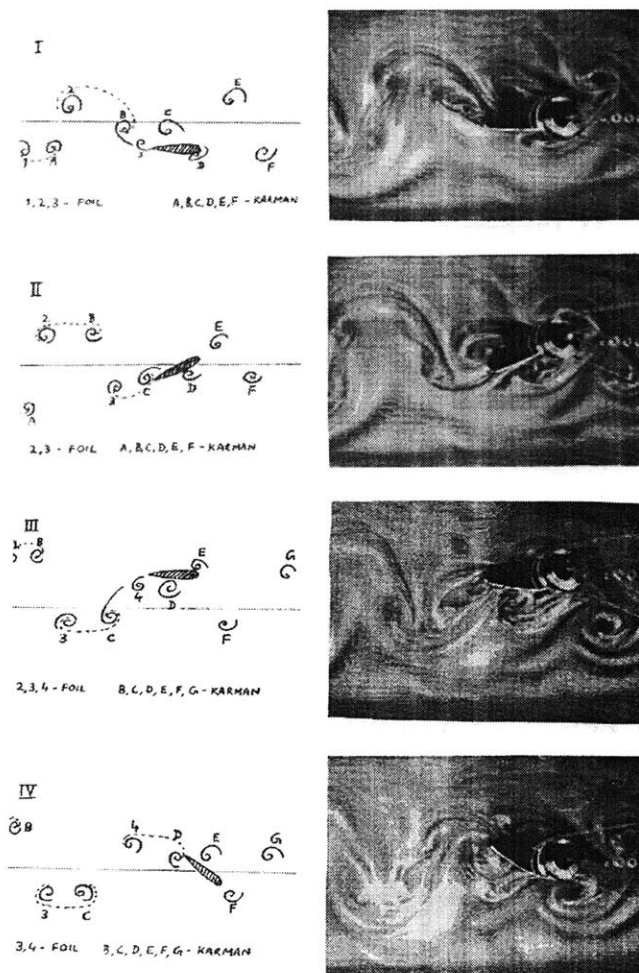
Figure 4-11: Vortex pairing as described by Gopalkrishnan

51

In the current experiments, none of the constructive and destructive vortex modes that Gopalkrishnan and Anderson described were encountered. There were two explanations that may explain why their results were not repeated here. First, the destroyer hull's unique wake was extremely different from that of a bluff body's. Second, the wake interaction between the two foil wakes may have played a larger role than expected and interfered in what would have been constructive or destructive vortex merging.

4.6.2 Four Vortices Per Cycle

During an experiment with an airfoil pitching sinusoidally about the quarter-chord point at an amplitude of 4° and frequency of 1.85 Hz., Koochesfahani noticed a wake pattern of four vortices per cycle (Figure 4-12). From the simultaneous mean velocity profile, he determined that the pattern corresponded to a double-wake structure. In many of the dye experiments performed with the foilboat, results shared a similar mushroom structure. The difference is that the vortices in Koochesfahani's case shed and convected upstream, whereas the vortices in the foilboat experiments convected downstream.
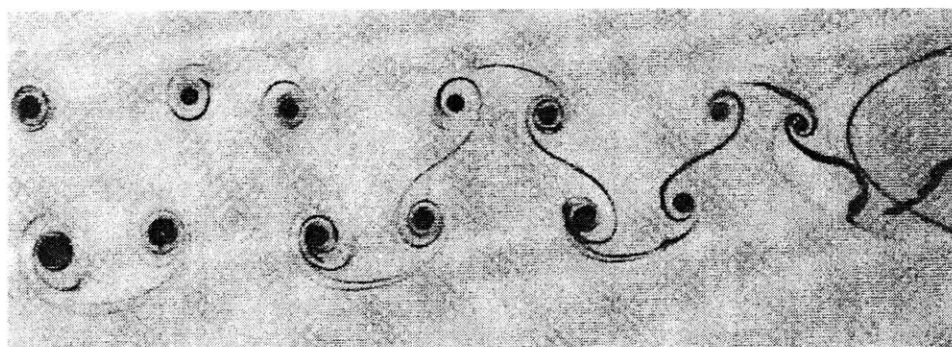
Figure 4-12: Wake of a NACA 0012 airfoil.

Another way to evaluate such a wake pattern is by looking at the slant or skew of the mushroom formation. If it slanted toward the upstream direction, it is indicative of drag production. If it slanted in the opposite direction, it is indicative of thrust

generation. Based on this premise, a schematic shown in Figure 4-13, was created to describe the activity in the wake of a typical run behind the foilboat. The vortex locations that are shown were straight from a run thus preserving the spacing for precise analysis. The thick arrow represents the induced velocity between two neighboring contra-rotating vortices and is the resultant of the two vectors, shown by dashed arrows, representing components of both lift and thrust. Summing the vectors, the lift components cancel each other yielding little or no net lift. However, the thrust components add to a net force in the downstream direction, which is indicative of a jet.
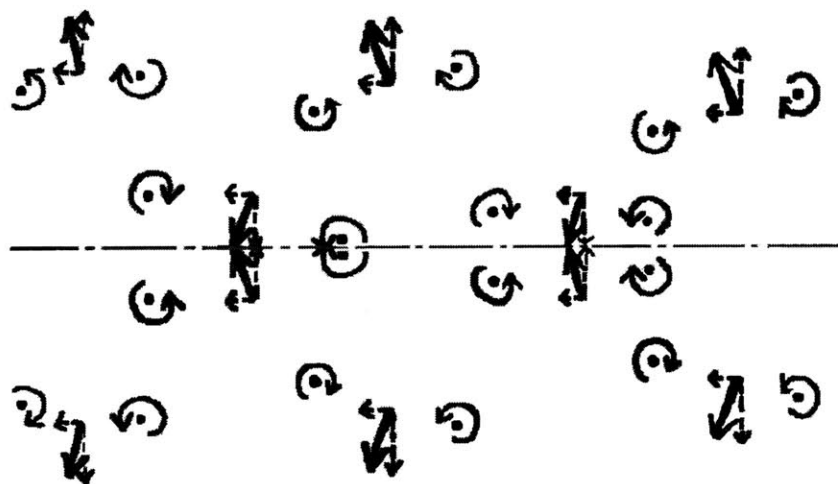
Figure 4-13: Schematic of four vortices per cycle formation in a thrust wake.

Though simplified this schematic yields interesting information about the foilboat wake. Other issues to consider that may affect the model include strength of vortices, vortex location, wake interaction, and three-dimensional effects, and also, force and/or velocity profiles in the wake, which were unavailable at this time.

4.7 Experimental Errors and Future Improvements

The dye visualization experiments were conducted as controlled as possible. However, as with any testing environment, errors could result from a variety of factors. In future experiments, these improvements may make a difference in obtaining better visualizations.

Most runs had asymmetric foil signatures. This may be due to the imprecision of the mechanism during its construction, that the foils may not be aligned in the vertical direction. Also, the profile of the foils could be smoother and refined. Hydrodynamic effects and interaction between vortices may have caused some asymmetry. The asymmetry should not have a large influence on the vortical characteristics.

These experiments were conducted with dye injection from each foil at three dye ports located at different depths. A better method of testing would be to test at each depth, especially since the hull was not uniformly shaped in draft.

For better images, the water could have been given more time to settle in between runs and more time for the dye to fully disperse.

The glare prevents viewing the dye as it rolls off the foils. If transparent watertight housings for the UV lights were available, they could be placed on the tank bottom as well as the sides, providing a significant increase in illumination for the dye without producing the interfering glare on the water surface.

Chapter 5

Conclusion

5.1 Summary

The oscillating foilboat mechanism had been partially redesigned, improved, and tested. The conducted experiments gave a preliminary insight into the complex interactions between the ship and foil wakes when operating at specific parameters. The runs consisted of varying the Strouhal number, maximum angle of attack, and phase.

Analysis was focused in four main categories: wavelength and wake width, wake structure classification, vortex spacing, and wake interaction. Characteristics of propulsive signatures were highlighted. Observations of other phenomena were pointed out, described and explained in the flow visualizations. Lastly, comparisons were made to previous visualization work.

5.2 Closing Remarks

Images from dye visualization can show patterns that are characteristic of drag and thrust. Though no data related to force or velocity was obtained in these experiments, by understanding the physics of the flow and several fundamental hydrodynamics concepts, certain assumptions could be made to evaluate the propulsive abilities of the foilboat mechanism. However, due to nonlinear effects and incomplete visualizations, pieces of the complex puzzle of oscillating foil propulsion requires further scrutiny.

The results from this project were encouraging, but more testing and research are called for to fully investigate the propulsive potential of the oscillating foilboat. This project is a good basis for designing other propulsive devices of similar nature.

5.3 Recommendations for Further Work

As the oscillating foilboat project currently stands, there is much room for improvement, as mentioned in the previous chapter. Similar and related projects can improve the design for efficient propulsion.

To test for transition regions between regimes, the parameter space could be densely covered as an opportunity to examine how sensitive the flow is to small variations in parameter. The dye visualization tests reported in this thesis are only part of a sparse matrix. By exploring the parameter space more thoroughly, other wake structures may appear.

Much of the literature described experiments with varying h, which in the conducted experiments, was fixed as a semi-arbitrary parameter to limit the testing space. Previous research has shown that h is a factor that is significant in the behavior of the wake. If h/c is reduced from 0.76 to 0.5, wake interaction effects would probably reduce due to the smaller widths of the foil wakes. Testing at various h/c would offer more insight into wake interaction.

The next logical step after visualizations is to obtain force measurements. Successfully combining flow visualization and force measurements is what Gopalkrishnan calls the "Holy Grail" of experimental hydrodynamics [6]. Dye visualization is successful only at low Reynolds numbers; while at higher Reynolds numbers, the dye disperses too quickly due to increased turbulence. Force measurements are obtainable at high Reynolds numbers where the force is of measurable magnitudes. However, if assuming the Reynolds number is not the determining factor in the way vortices behave, then scaling by Strouhal number, appropriate corresponding tests at low Reynolds numbers and high Reynolds numbers would be feasible.

DPIV is a technique that obtains a planar velocity field by using a laser to illuminate particles for video capture. It uses the cross correlation function with position of particles to determine how far they have traveled. The fluid is seeded with neutrally buoyant particles that are small enough to not disturb the flow. The strength of vortices could be determined by how long the velocity vectors are, essentially looking at how fast the particles swirl. The figure below illustrates the DPIV algorithm.

56

Spatial Cross Correlation

$$\Phi_{fg}(m,n) = \frac{\sum_{k=-\infty}^{\infty}\sum_{l=-\infty}^{\infty}f(k,l)g(k+m,l+n)}{\sum_{k=-\infty}^{\infty}\sum_{l=-\infty}^{\infty}f(k,l)\sum_{k=-\infty}^{\infty}\sum_{l=-\infty}^{\infty}g(k,l)}$$

Gaussian Peak Finding

x

y

f(m,n)   g(m,n)

Image A   Image B
time t   time t+dt

$\Delta x, \Delta y$
Displacement Data
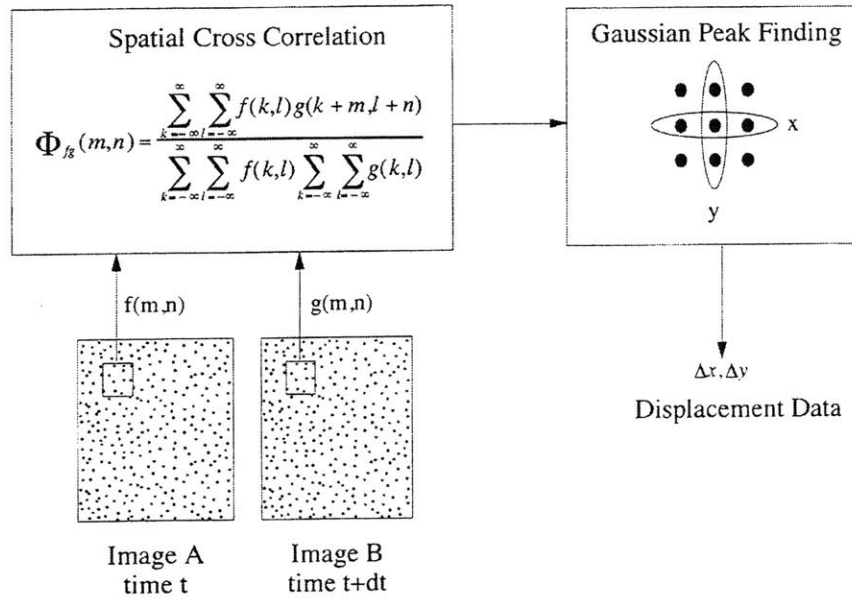
Figure 5-1: DPIV Algorithm

Three-dimensional visualization research is useful in determining the effects of increases in depth. Since the destroyer hull is non-uniform in shape, it is expected that vortical patterns are extremely complex and difficult to determine purely by looking at the water surface. In Techet's tapered cylinder experiments, she determined that the shedding patterns between the top larger diameter portion of the cylinder and the bottom smaller diameter differed [16]. Though the destroyer hull is not a cylinder, the assumption can be made that there are transitions from variations in hull contours. By using DPIV, three-dimensional patterns can be visualized.

Spring-driven foils for oscillating foil propulsion have been suggested and investigated by Harper, et al [8]. Typical actuation systems are not designed to recover energy when negative work is performed therefore the power generated is usually dissipated. Springs can temporarily store energy which can be used later on. A dynamic model for an oscillating underwater foil have been developed using a set of linear ordinary different equations. From these equations, optimal spring constants have been found. A comparison has been done with an optimal lateral spring in series with an actuator verses an actuator without the spring. The difference in energy used is 33%. If such a system is implemented for the foilboat mechanism, the efficiency may increase.

An addition of a surface plate can inhibit splashing therefore prevent certain energy loss. Essentially, it will act like a stern flap, an appendage which reduces the power required to propel a ship through water. The result is a reduction in the propulsion consumed and an increase in efficiency. Usually it is placed at the hull bottom surface aft of the transom. Through model scale testing, Cusanelli and Hundley reported the Navy has already investigated and found it feasible to install a stern flap behind the existing transom wedge for the Arleigh Burke class destroyers [3]. Implementing a similar design for the destroyer hull and operating the foilboat with this improvement can also increase the efficiency.

Upon closer examination of various aquatic animals, most of them have a rounded fin or flipper. For example, fast swimming fish tend to have a lunate tail. Identifying the most compatible shape with the oscillating foilboat can potentially increase its efficiency and attractiveness as an alternative to propellers.

Fish and penguins do not have rigid appendages, but semi-flexible ones instead. As summarized in the first chapter, Yamaguchi found that a partly flexible propulsor is more efficient than a rigid one or propellers [20]. Liu [11] confirms Yamaguchi's findings through extensive simulations on both chordwise and spanwise flexible foils and found that they are more efficient than rigid foils. Liu also performed simulations with whale flukes, which have specific shapes and chordwise and spanwise flexibility. This research is fitting for the oscillating foilboat as it may increase its efficiency.

Maneuverability is a distinct advantage that foils have over propellers. However, it has not been quantified. Read [15] has performed large pitch biased experiments to a single flapping foil to obtain significant lift and brake forces. The foilboat mechanism's effect on the destroyer hull's maneuverability can be an interesting and beneficial study.

Many such ideas can be implemented to enhance the operation of the oscillating foilboat. Further investigation into adapting projects for foilboat use is recommended.

Appendix A – MATLAB Script to Find θ

```
% aoa.m
% written by Franz Hover  12/99
% find theta required to achieve max. AoA
%     input phi, h, St, U, AoA

clear all;

phi = 90/180*pi ; % phase angle, rad
h0 = .057 ;      % heave amplitude, m
st = .2 ;        % strouhal number
alpha_des = 10/180*pi ; % desired max angle of attack, rad
u = .2 ;      % speed, m/s

% first solve for frequency from strouhal number
f = st*u/2/h0 ;       % hz
w = 2*pi*f ;       % rad/s

tf = 1/f/2 ;        % time of one-half cycle, s
tvec = 0:tf/20:tf ;
th0vec = 0:.01:1 ;   % range of pitch angles to check, rad

% go through one-half cycle, noting the alpha that you achieve
% with the trial pitch angle; compute an error between the desired
% maximum value of alpha with the actual value.
disp('working...');
for j = 1:length(th0vec),
   for i = 1:length(tvec),
      alpha(i) = -atan(h0*w*cos(w*tvec(i))/u) + ...
         th0vec(j)*sin(w*tvec(i)+phi) ;
   end;
   err(j) = (max(alpha) - alpha_des)^2 ;

   % how much does atan(...) exceed the pure pitch -- positive
   % values lead to thrust
   rel_angle(j) = atan(h0*w/u) - th0vec(j)*sin(phi) ;
end;

% present the best few solutions - first two are probably desired
[junk,ind] = sort(err) ;
disp(' ');
disp('6 Best Solutions (pick the one with rel_angle > 0:');
for i = 1:6,
   disp(sprintf('%2d.  theta:%5.3f  error:%7.2e  rel_angle:%5.2f',i,...
      th0vec(ind(i))*180/pi, err(ind(i)), rel_angle(ind(i))*180/pi )) ;
end;
disp(' ')

plot(th0vec,log10(err)) ;
xlabel('theta');
ylabel('log(error)');
```

Appendix B – Visualization Experiments

Note:

The images are oriented in landscape form.

The 10 images progress in time from left to right, in the specified time increments.

The flow is from right to left.
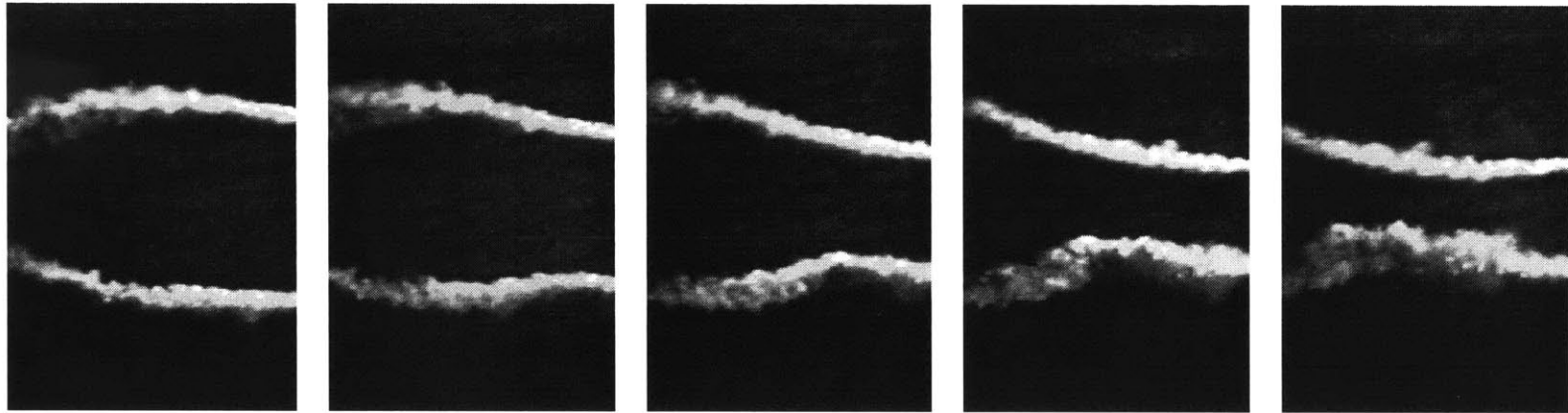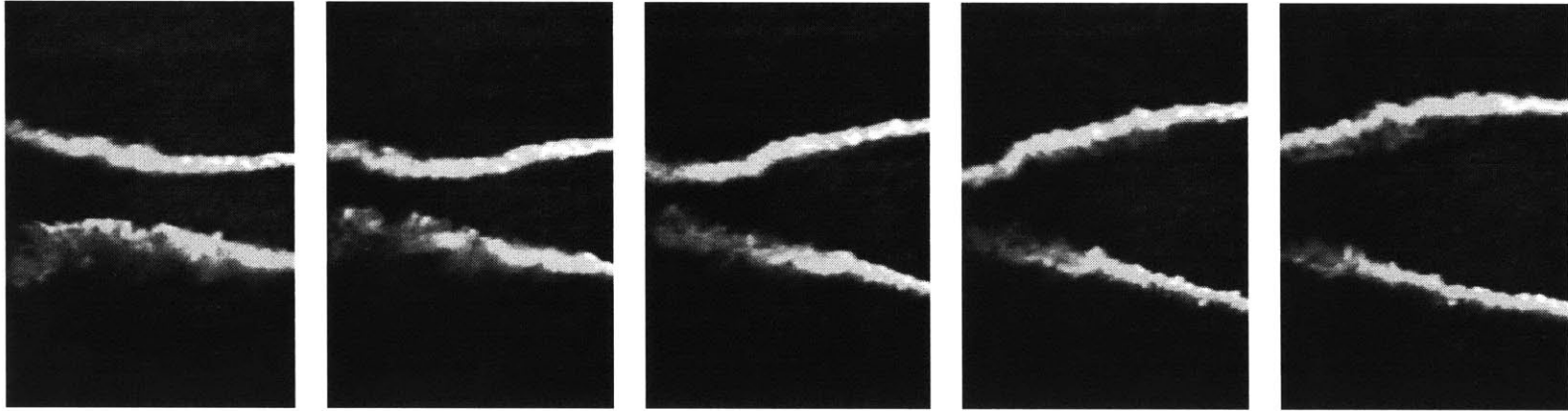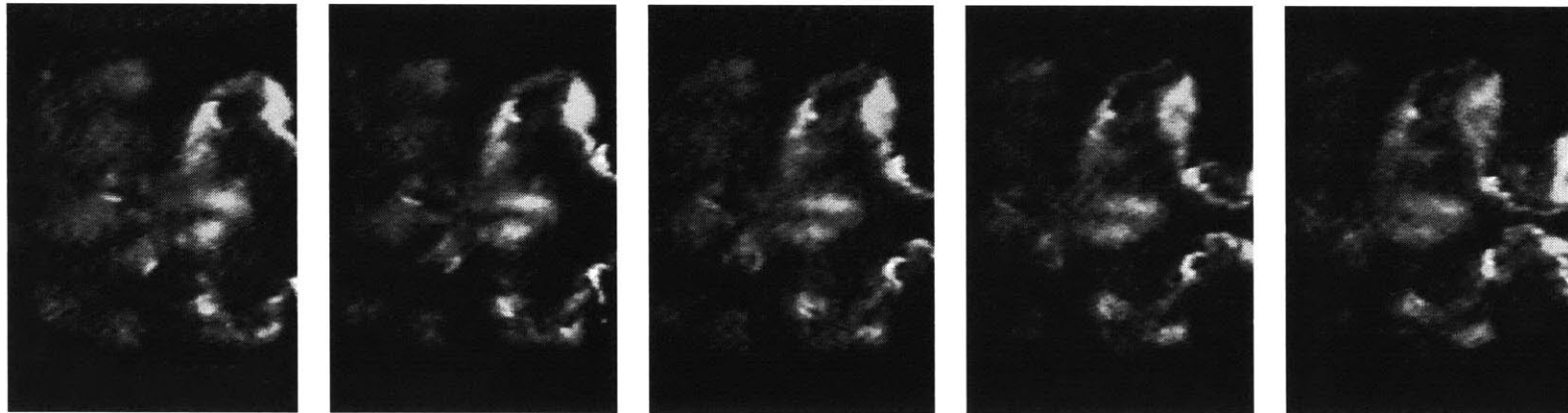
Run 1 : $\alpha = 10°$, St. # = 0.1, $\phi = 90°$ between each frame $\Delta t = 0.633$
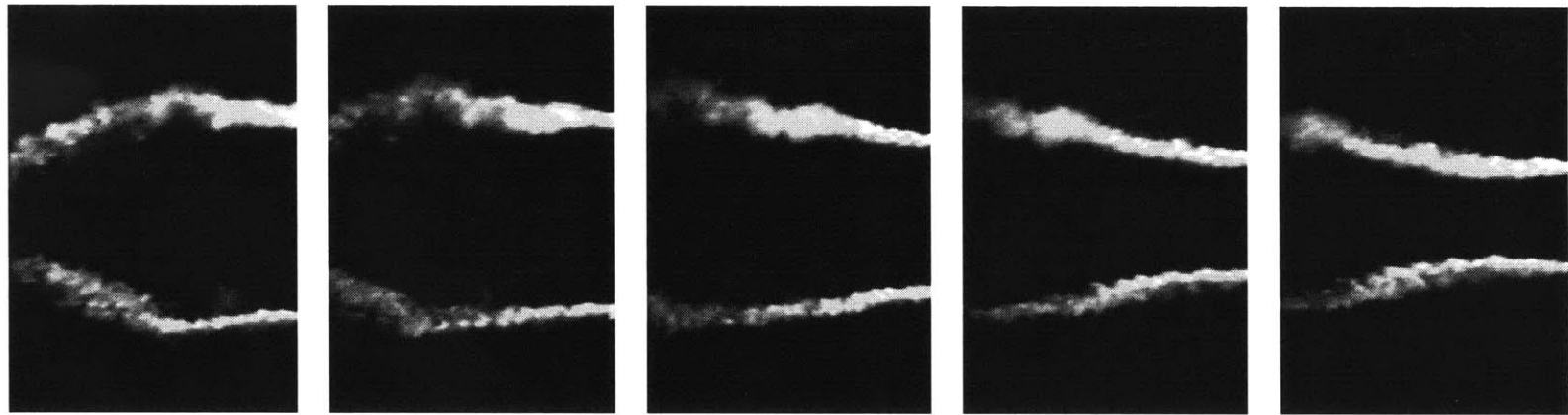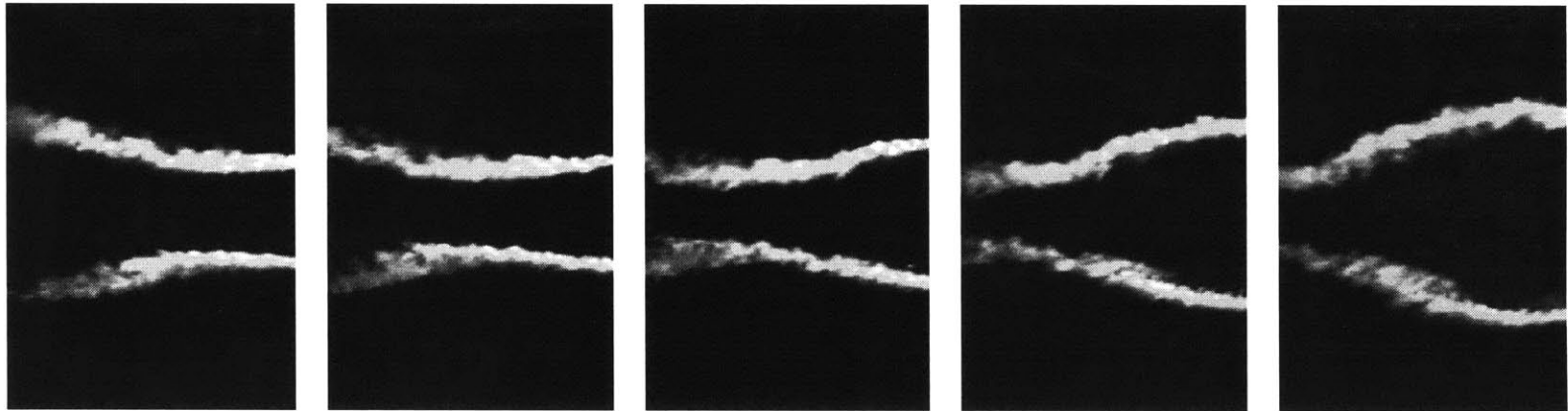
Run 2 : $\alpha = 15°$, St. # $= 0.1$, $\phi = 90°$ between each frame $\Delta t = 0.633$
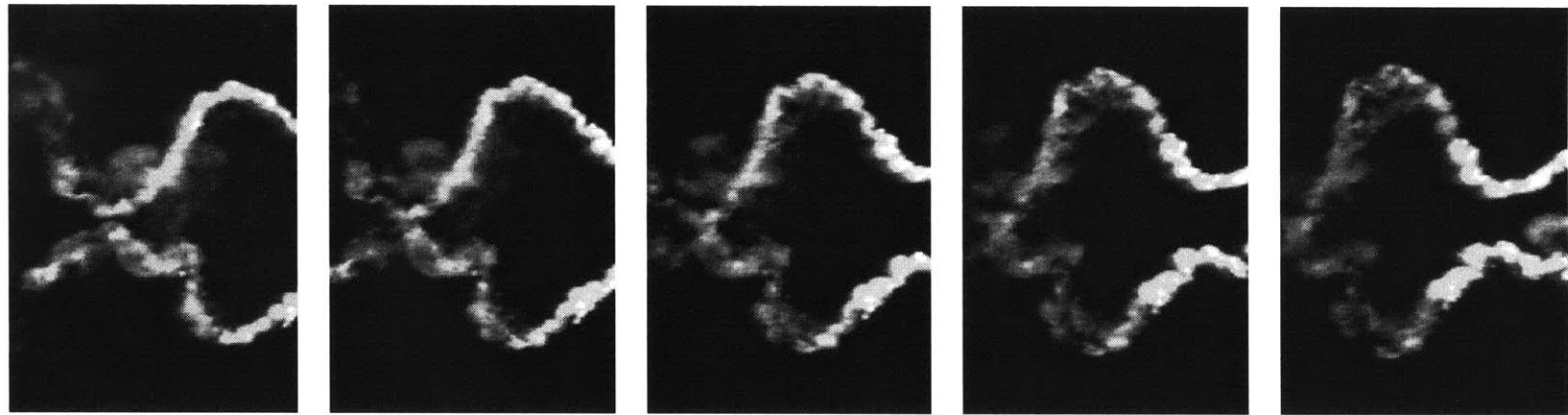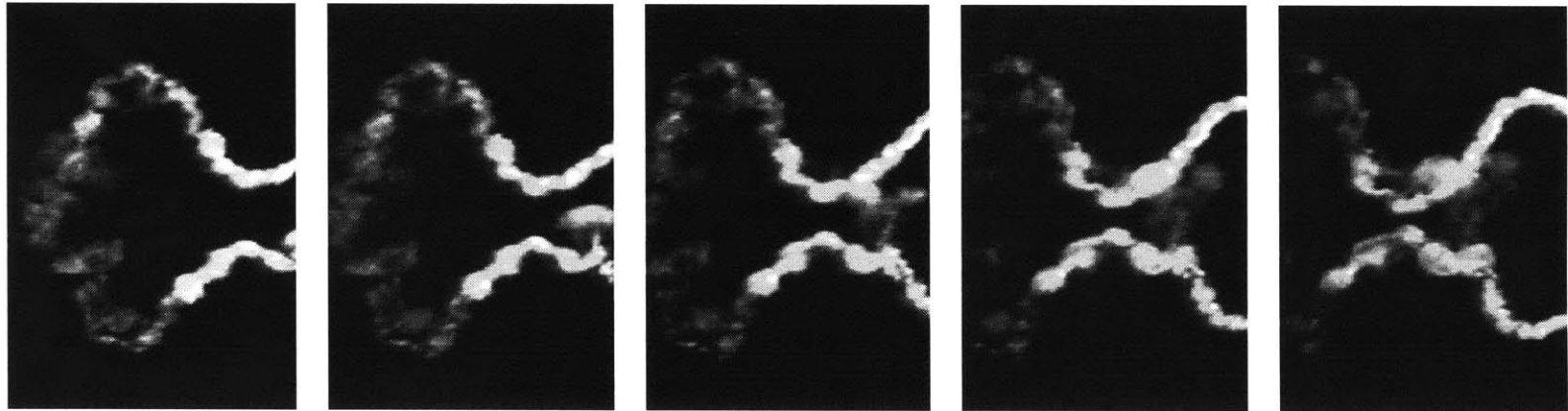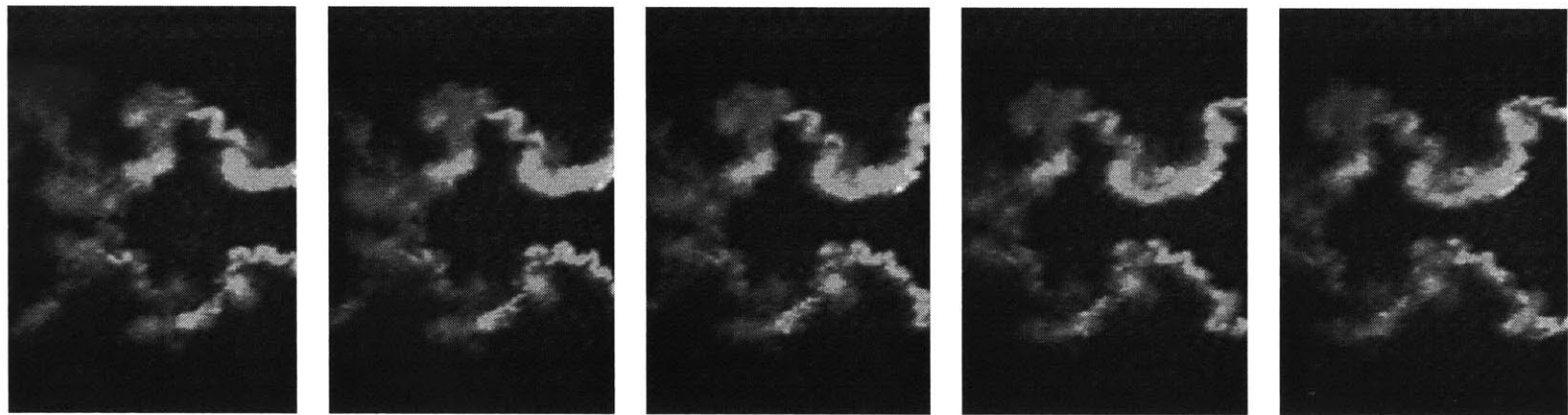
Run 3 : α = 10°, St. # = 0.2, φ = 90°   between each frame Δt = 0.333
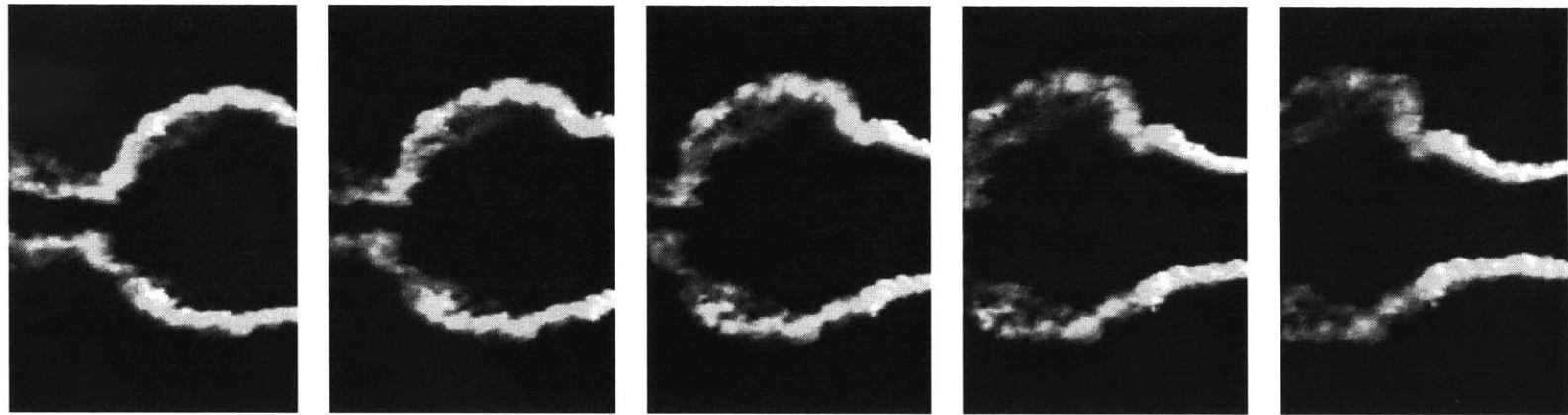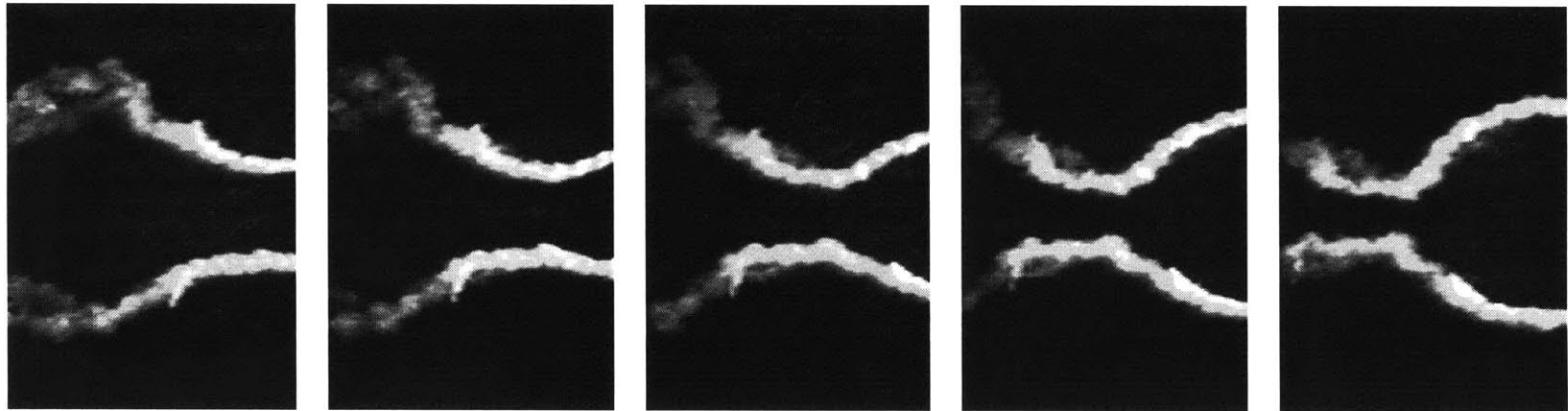
Run 4 : $\alpha = 15°$, St. # = 0.2, $\phi = 90°$ between each frame $\Delta t = 0.333$
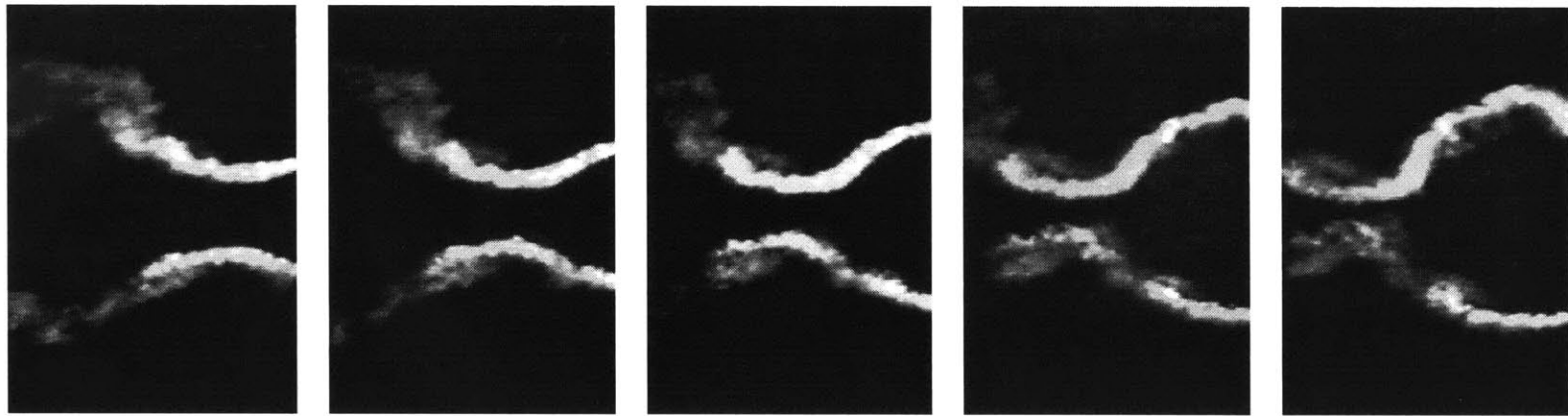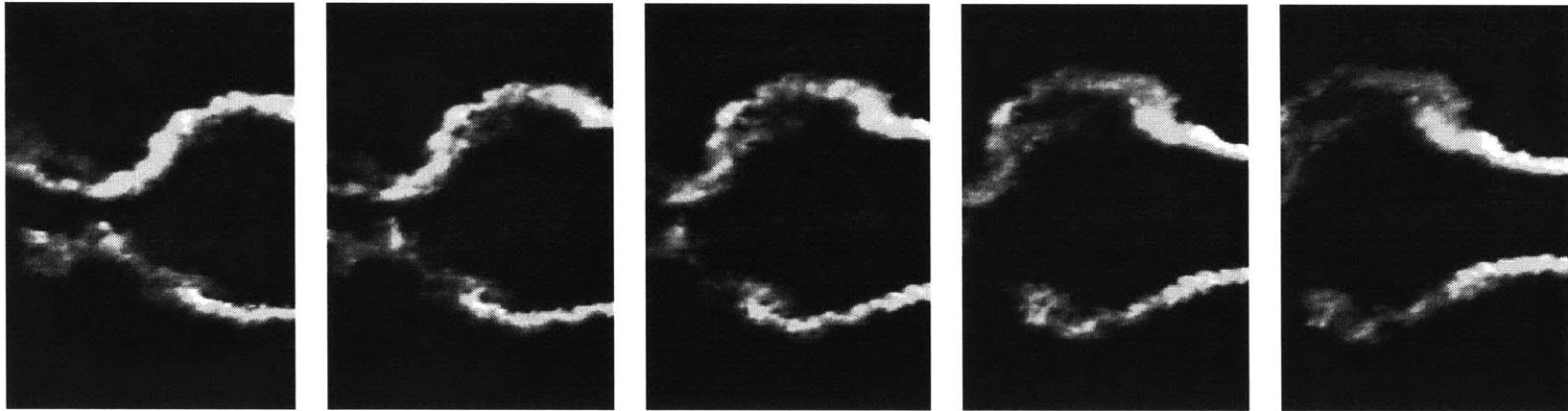
Run 5 : $\alpha = 20°$, St. # = 0.2, $\phi = 90°$ between each frame $\Delta t = 0.333$
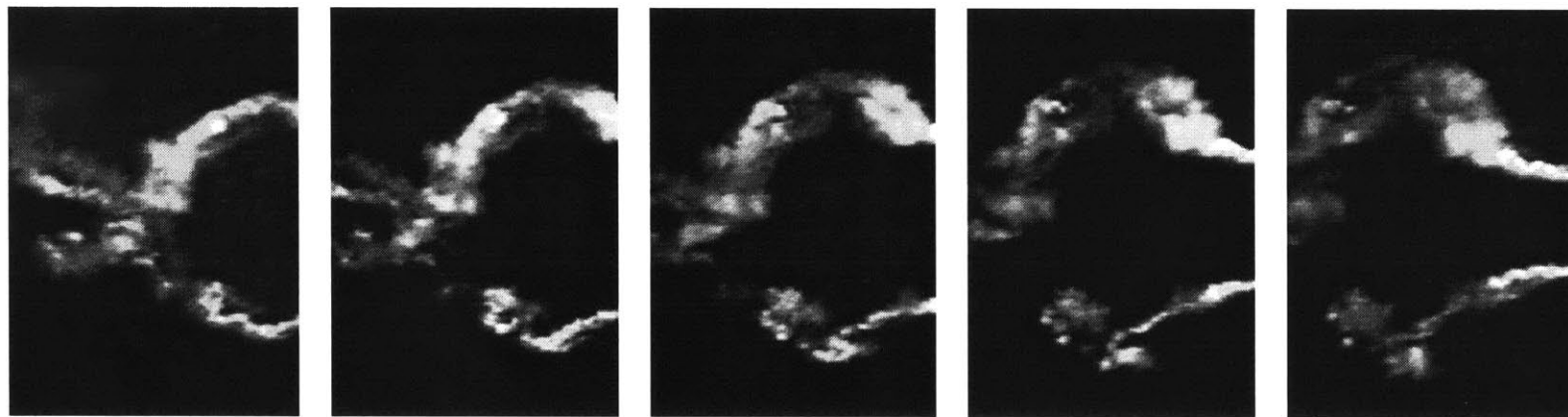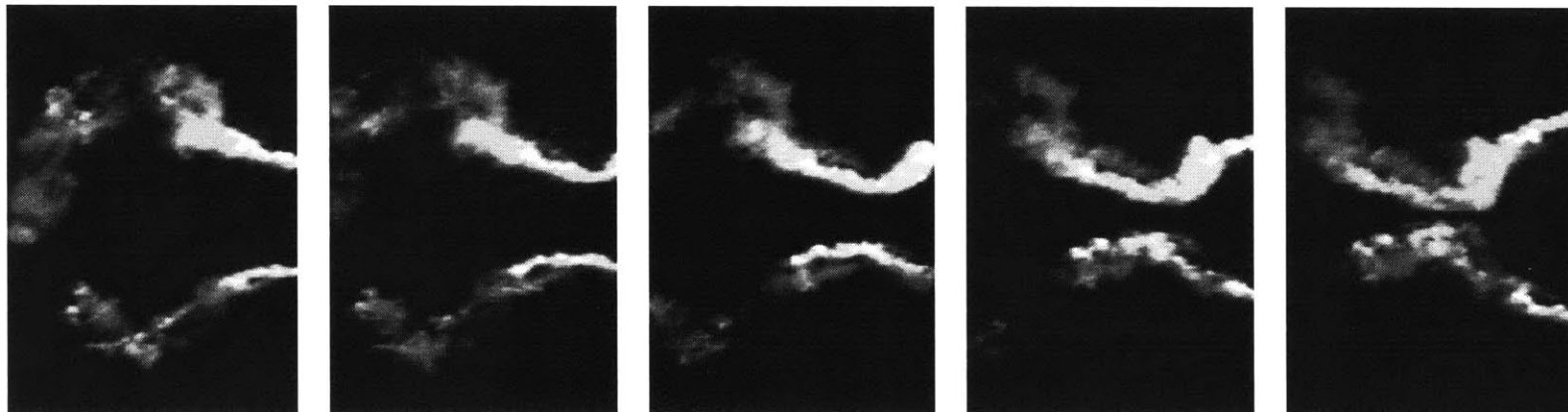
Run 6 : $\alpha = 25°$, St. # = 0.2, $\phi = 90°$ between each frame $\Delta t = 0.333$
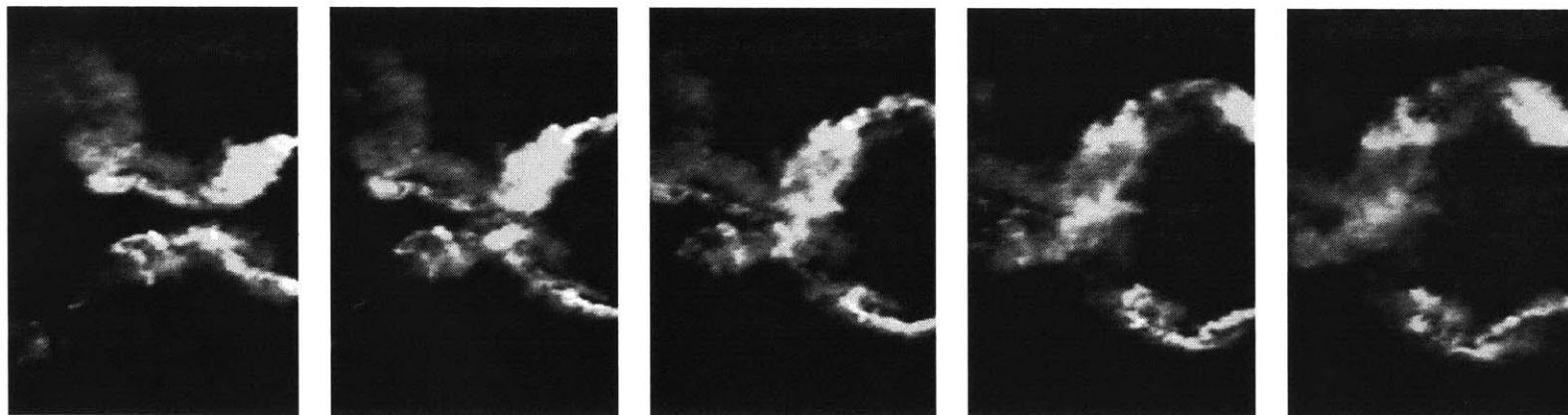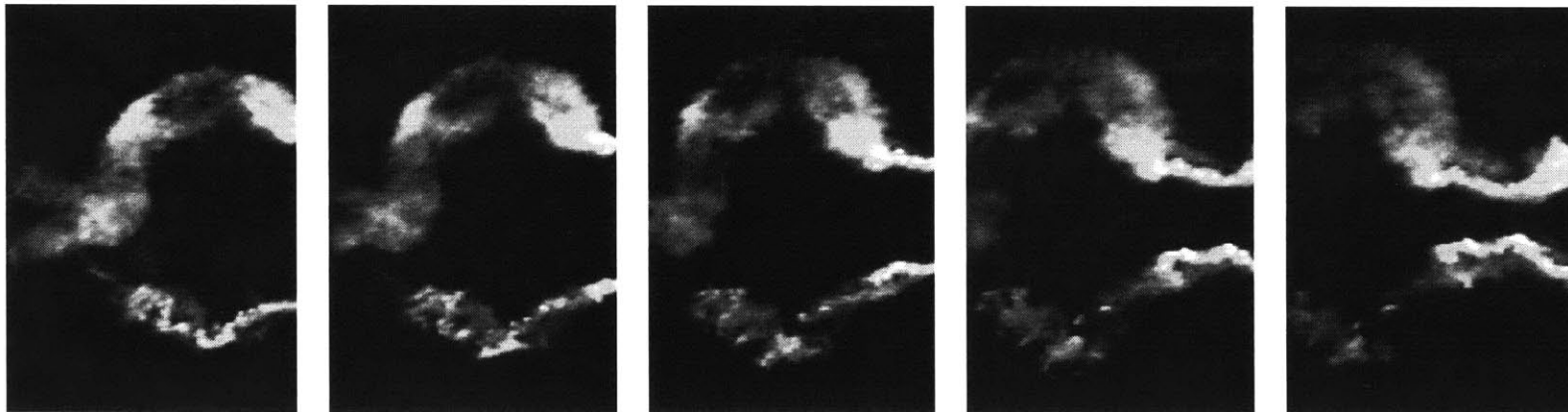
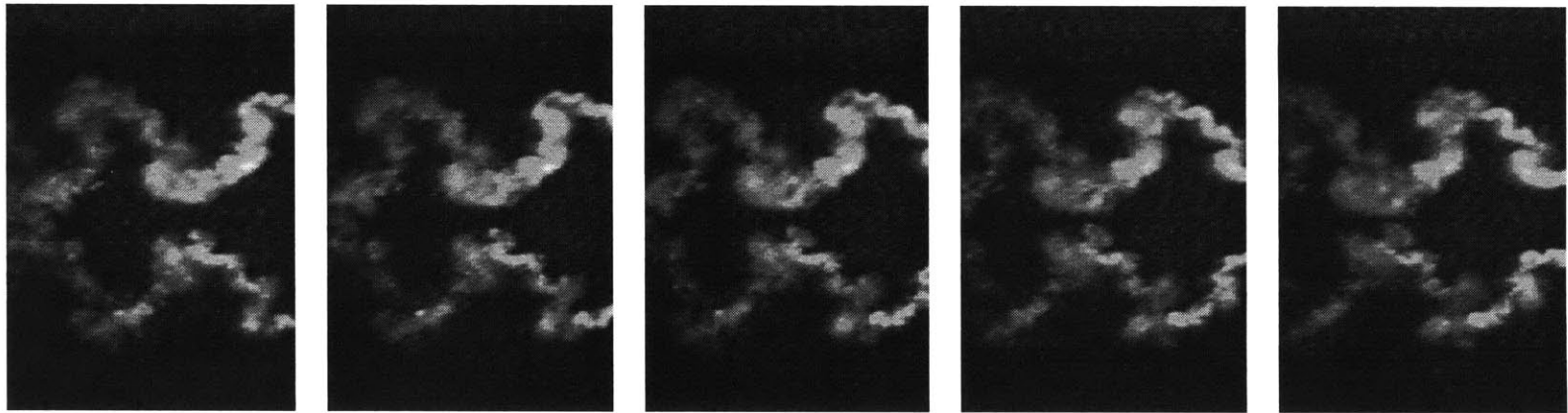Run 7 : $\alpha = 30°$, St. # = 0.2, $\phi = 90°$ between each frame $\Delta t = 0.333$
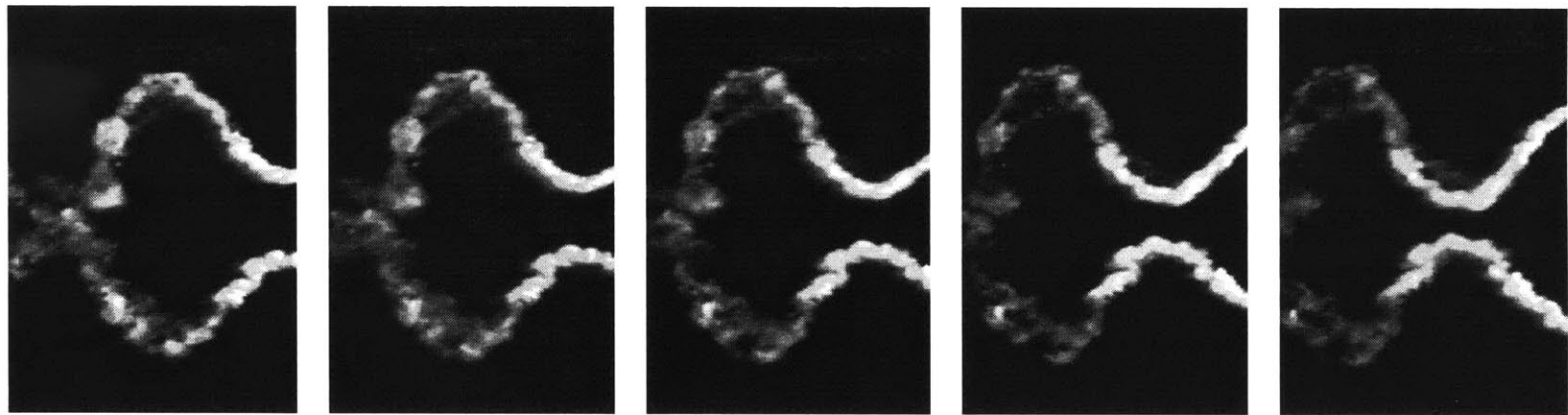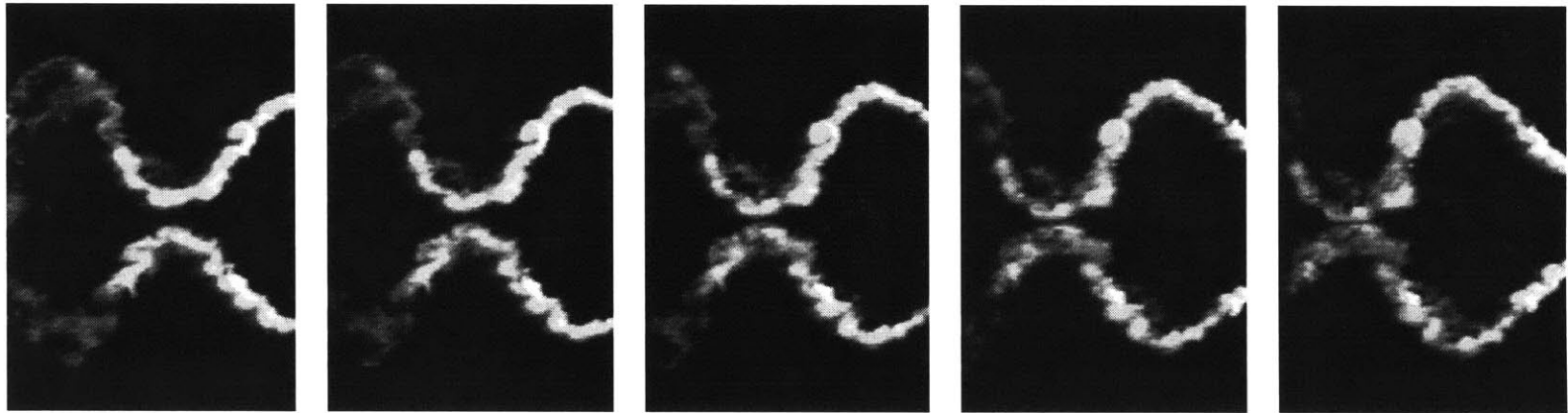
Run 8 : $\alpha = 10°$, St. # = 0.3, $\phi = 90°$ between each frame $\Delta t = 0.233$
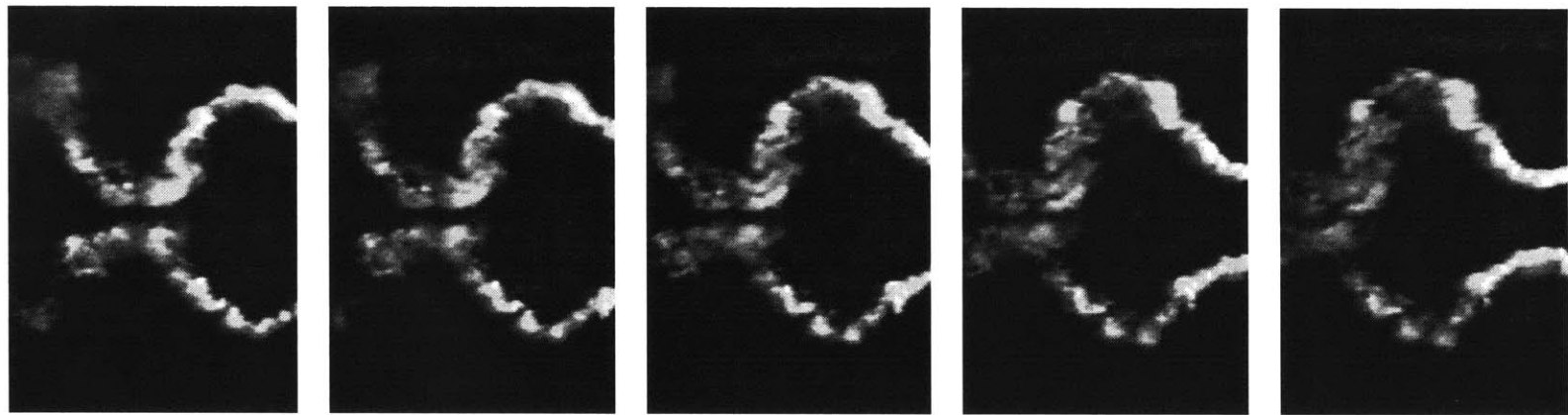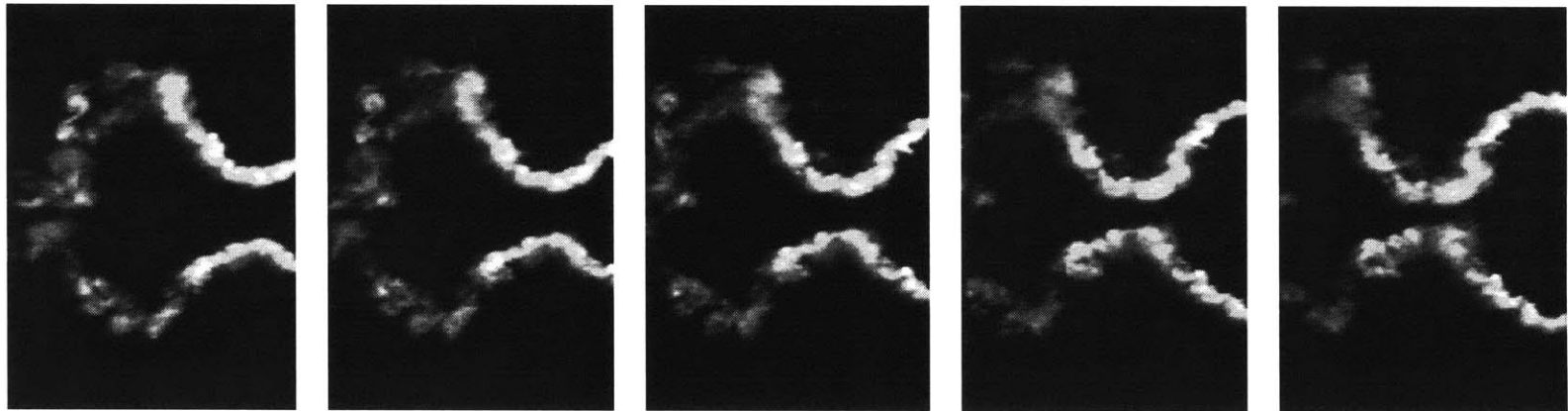
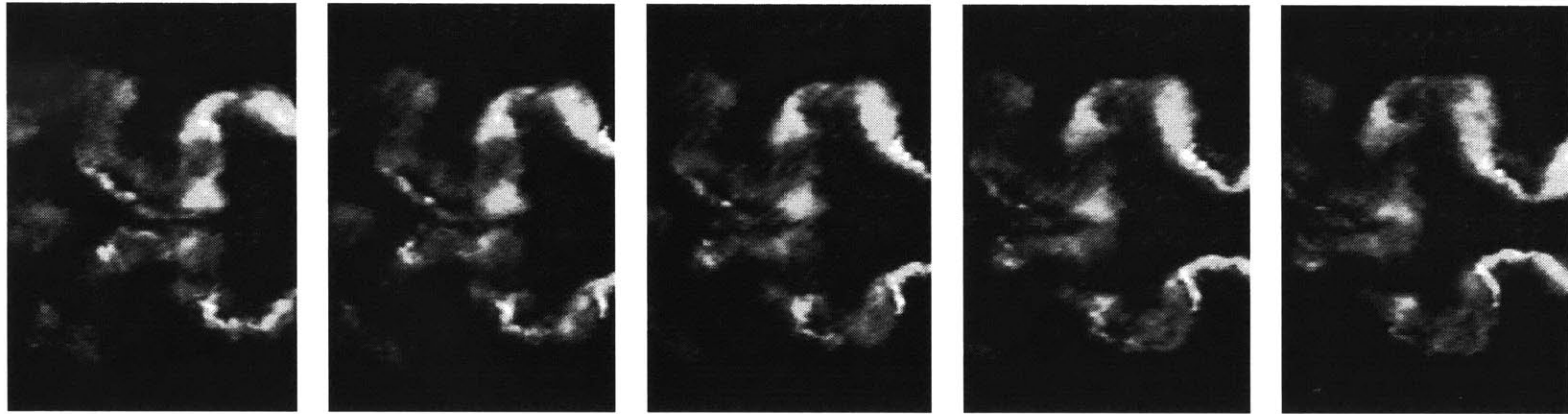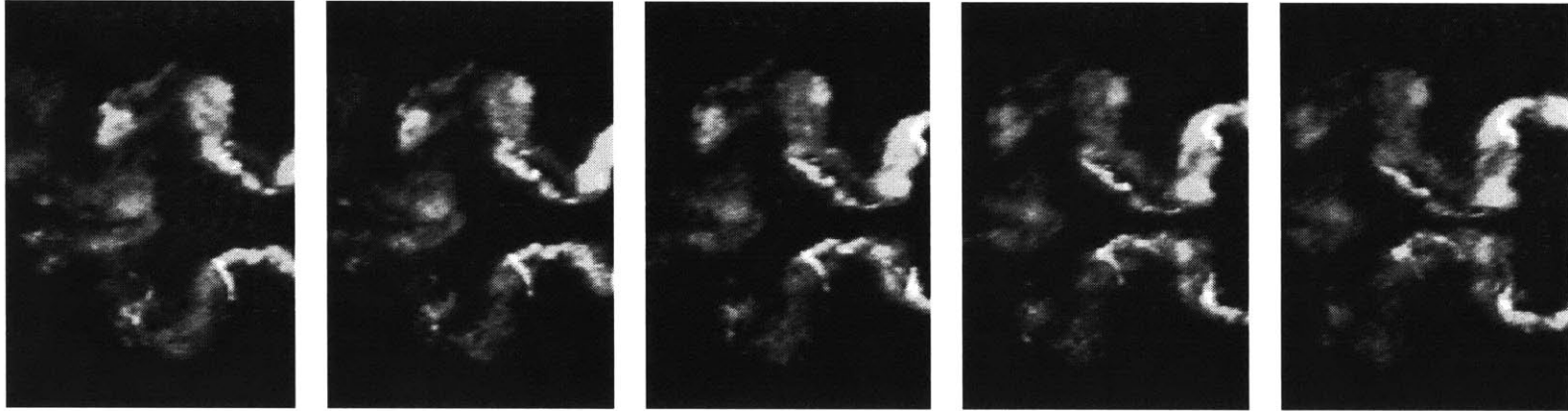Run 9 : $\alpha = 15°$, St. # = 0.3, $\phi = 90°$ between each frame $\Delta t = 0.233$
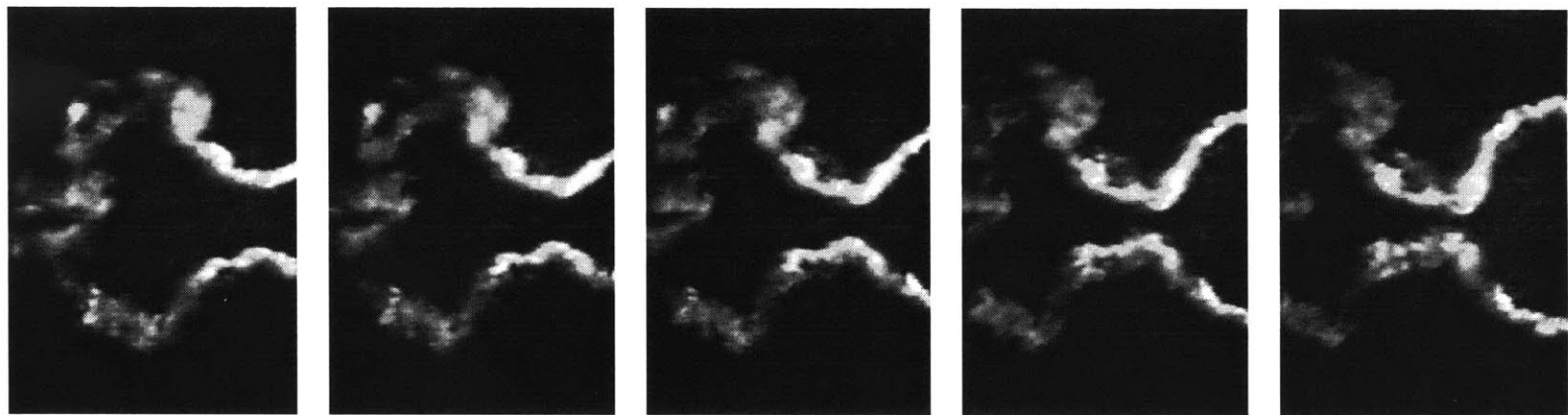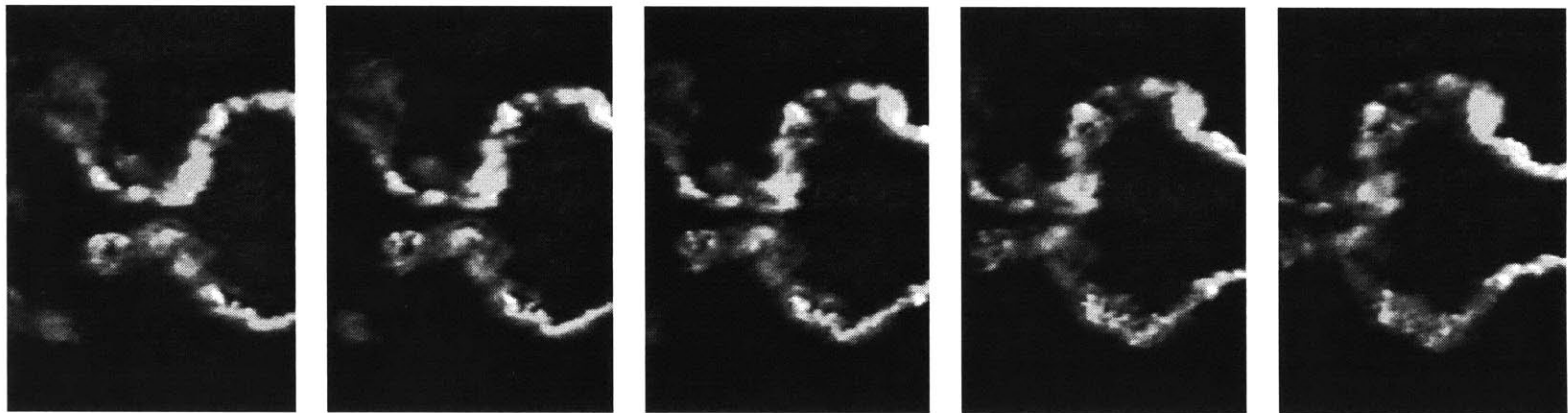
Run 10 : $\alpha = 20°$, St. # = 0.3, $\phi = 90°$ between each frame $\Delta t = 0.233$
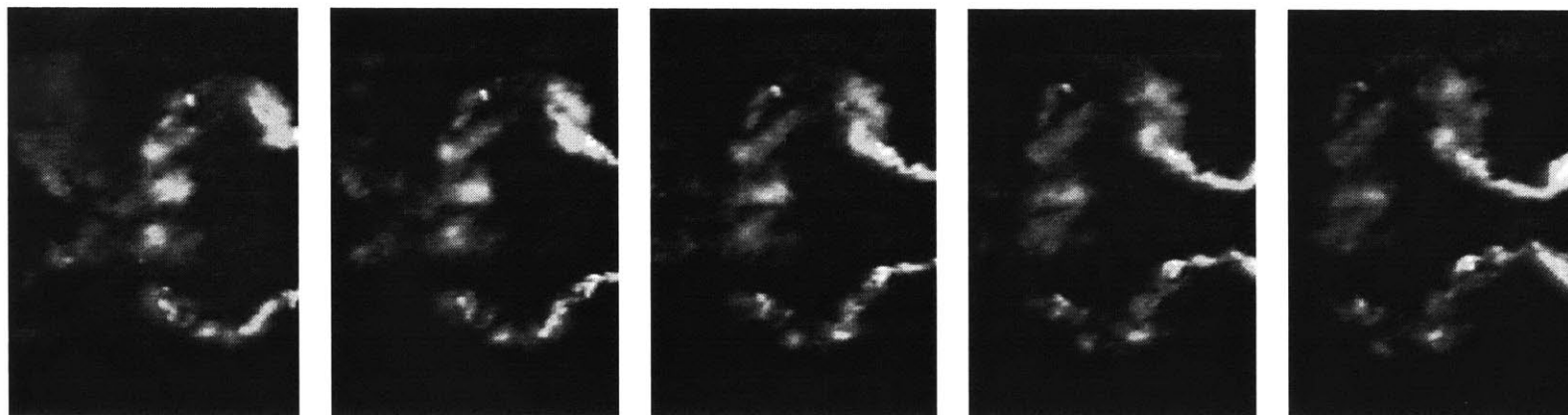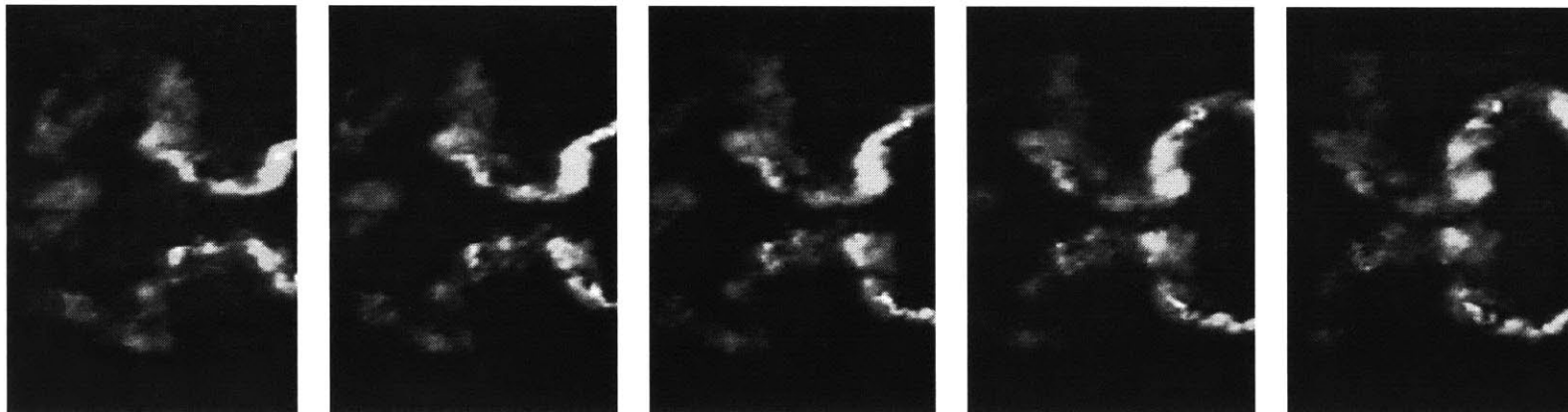
Run 11 : $\alpha = 25°$, St. # = 0.3, $\phi = 90°$ between each frame $\Delta t = 0.233$
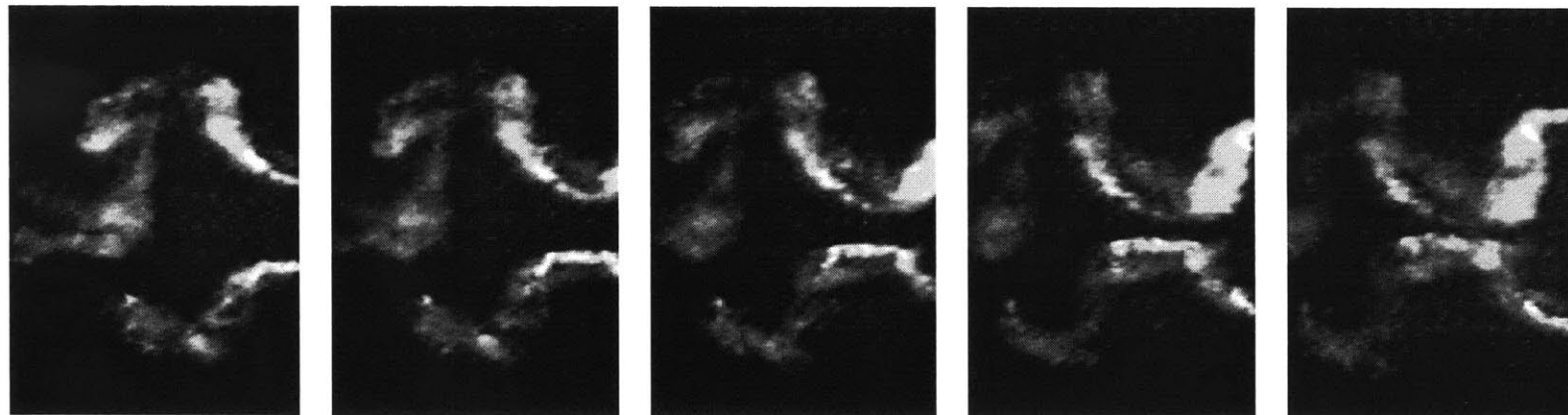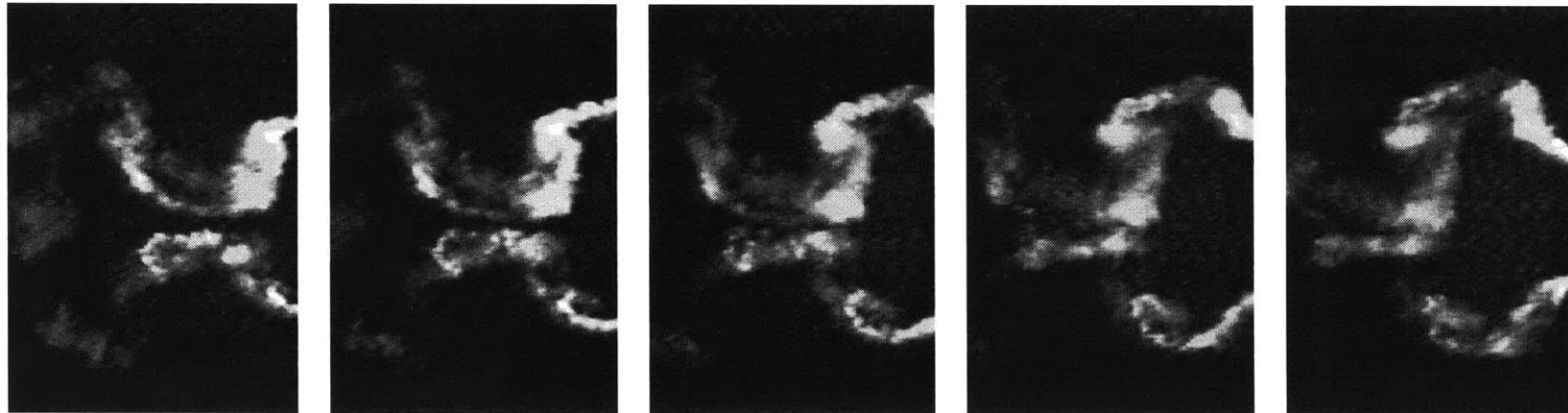
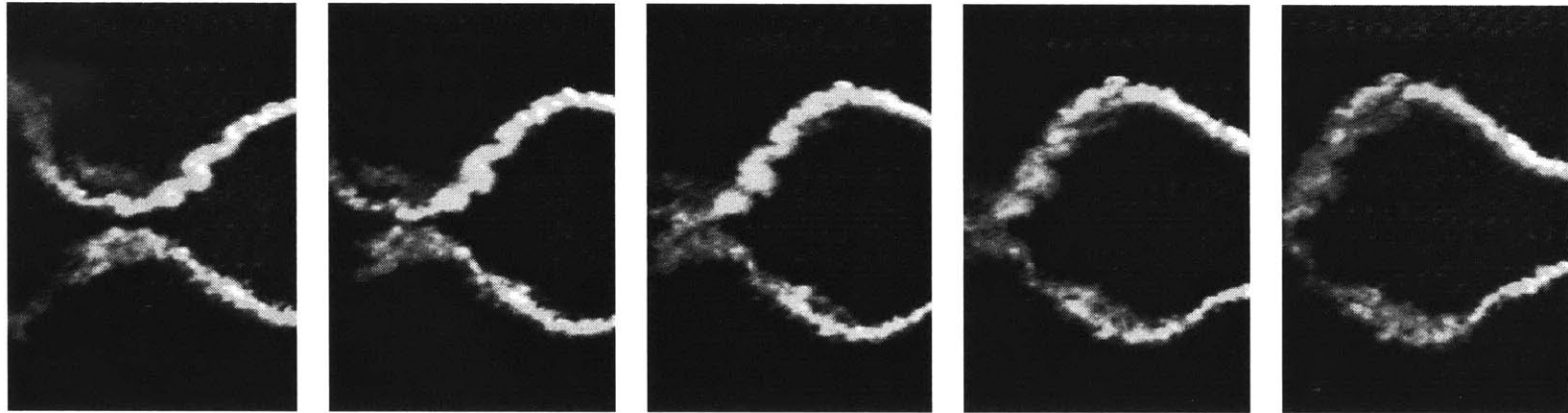Run 12 : $\alpha = 30°$, St. # = 0.3, $\phi = 90°$ between each frame $\Delta t = 0.233$
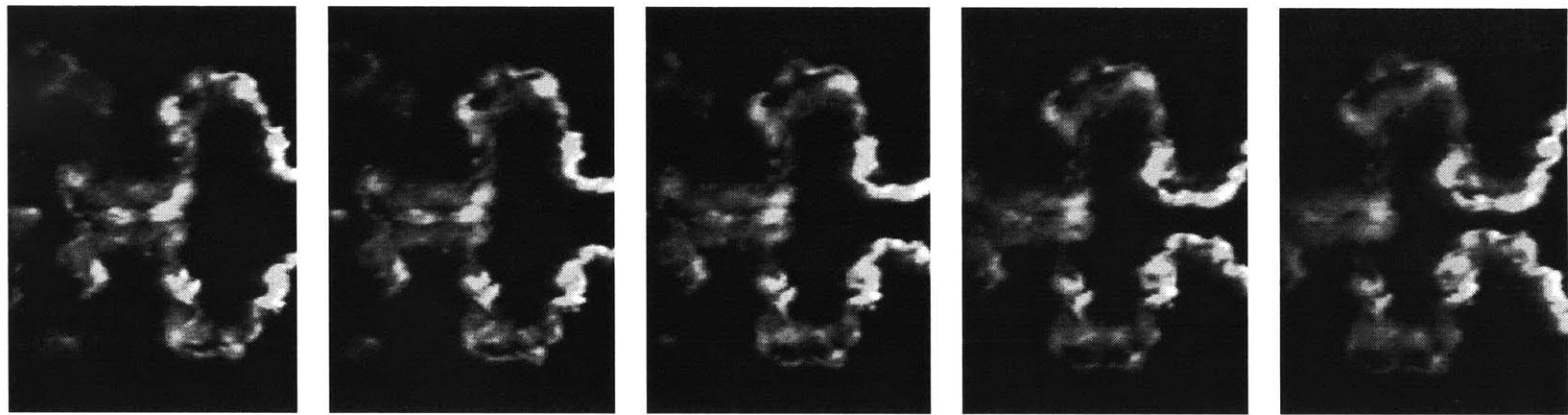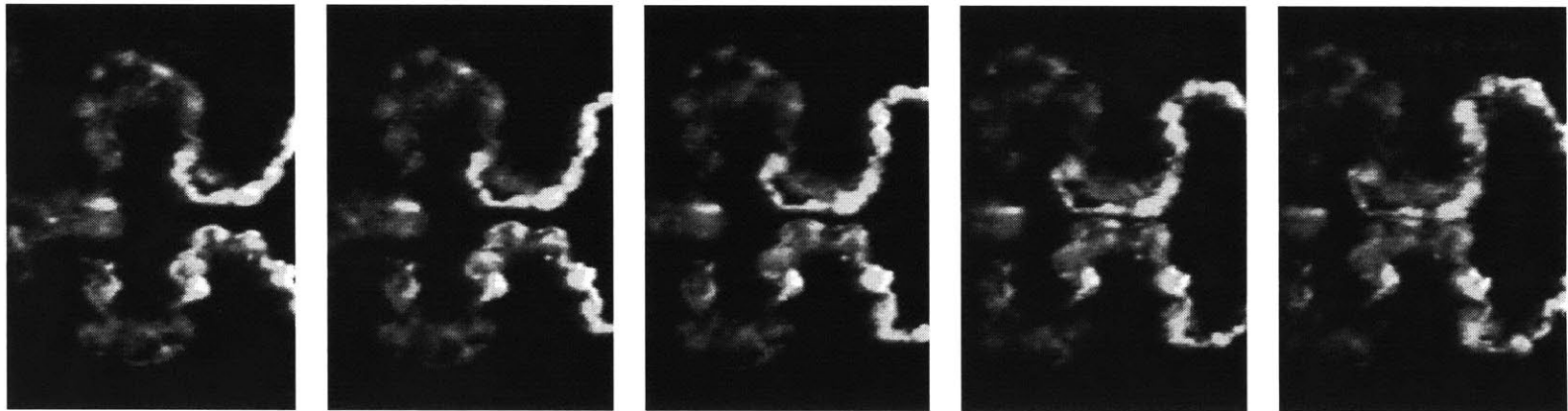
Run 13 : $\alpha = 10°$, St. # = 0.4, $\phi = 90°$ between each frame $\Delta t = 0.167$
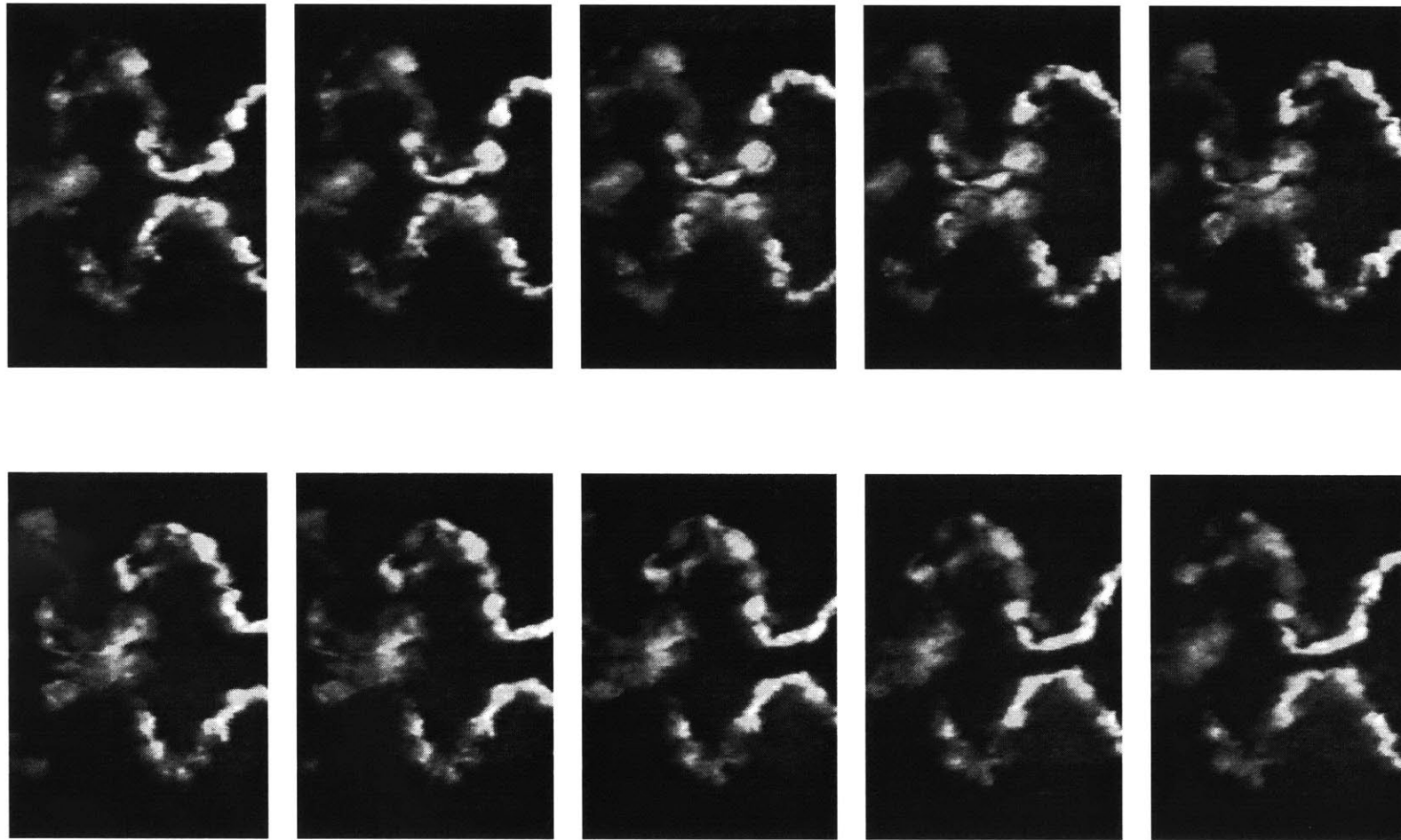
Run 14 : $\alpha = 15°$, St. # = 0.4, $\phi = 90°$ between each frame $\Delta t = 0.167$
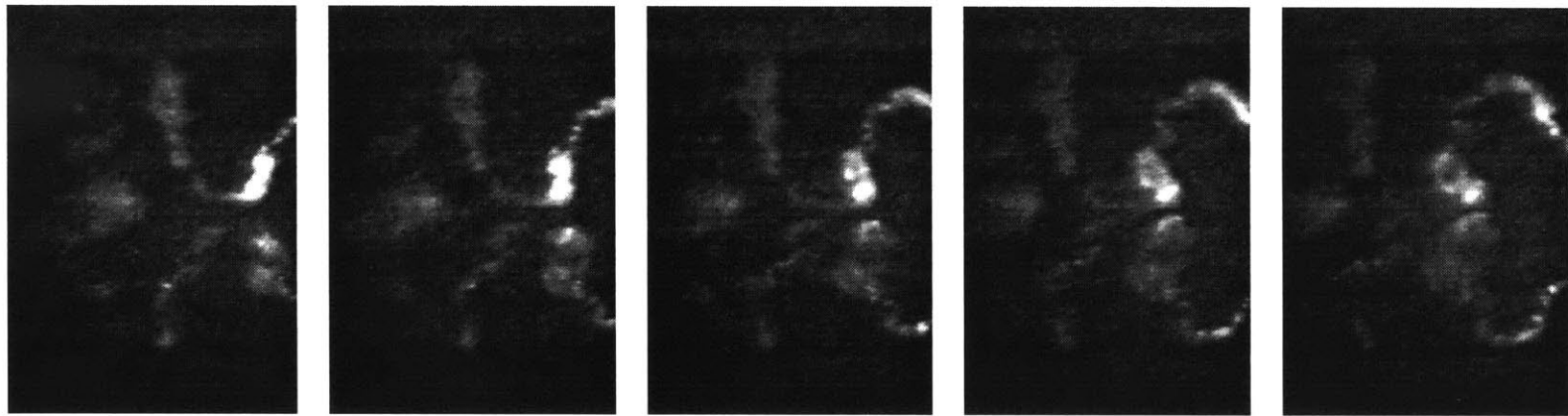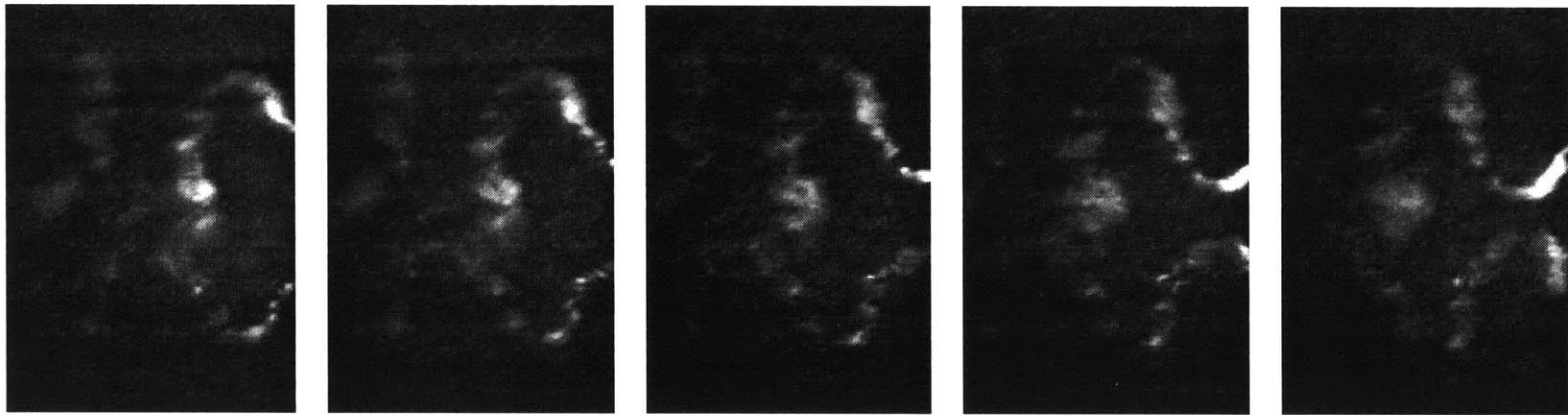
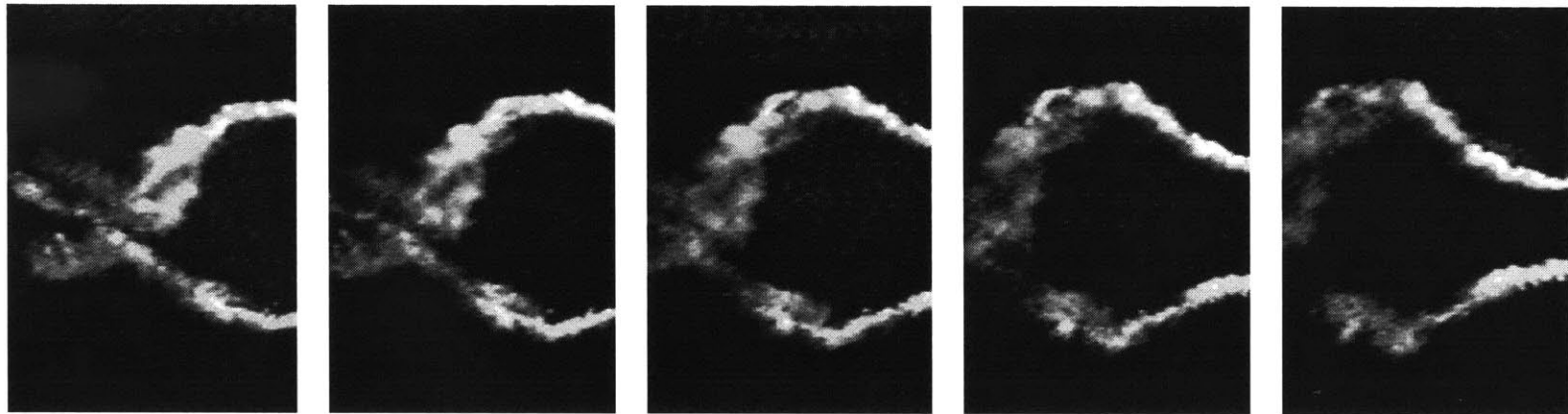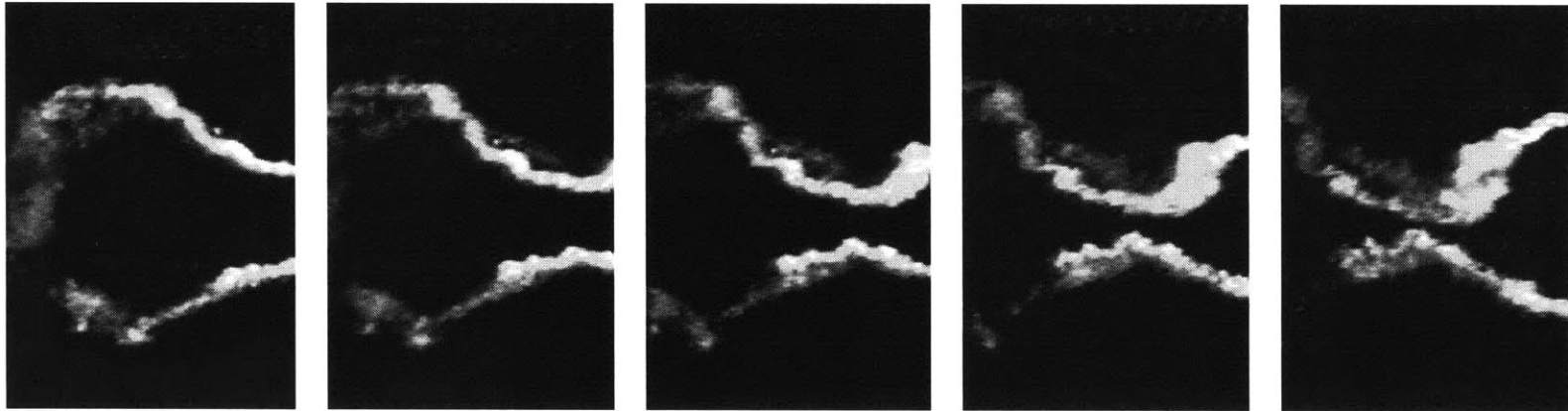Run 15 : $\alpha = 20°$, St. # = 0.4, $\phi = 90°$ between each frame $\Delta t = 0.167$
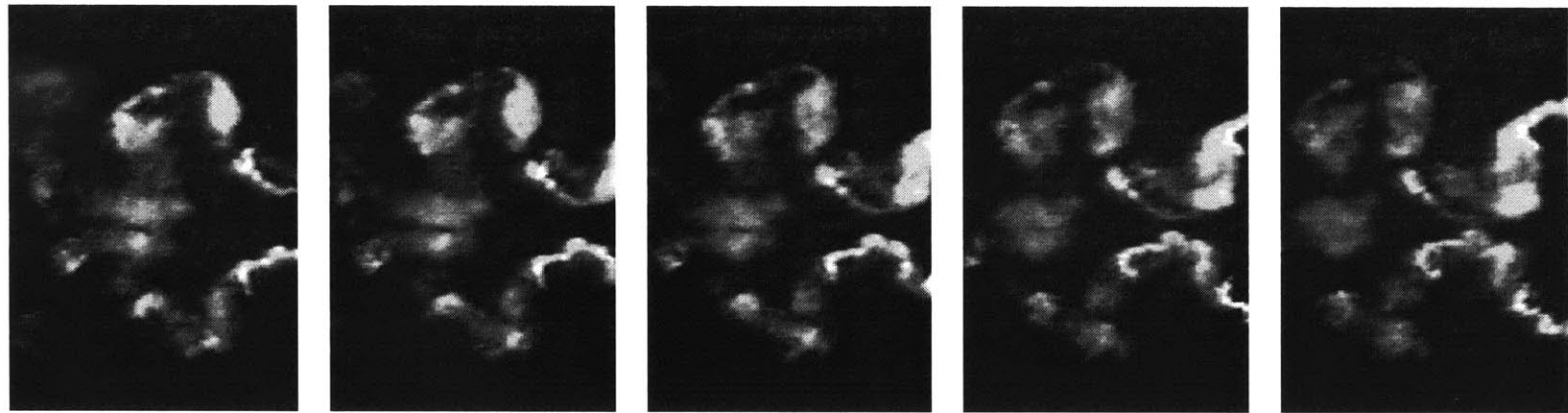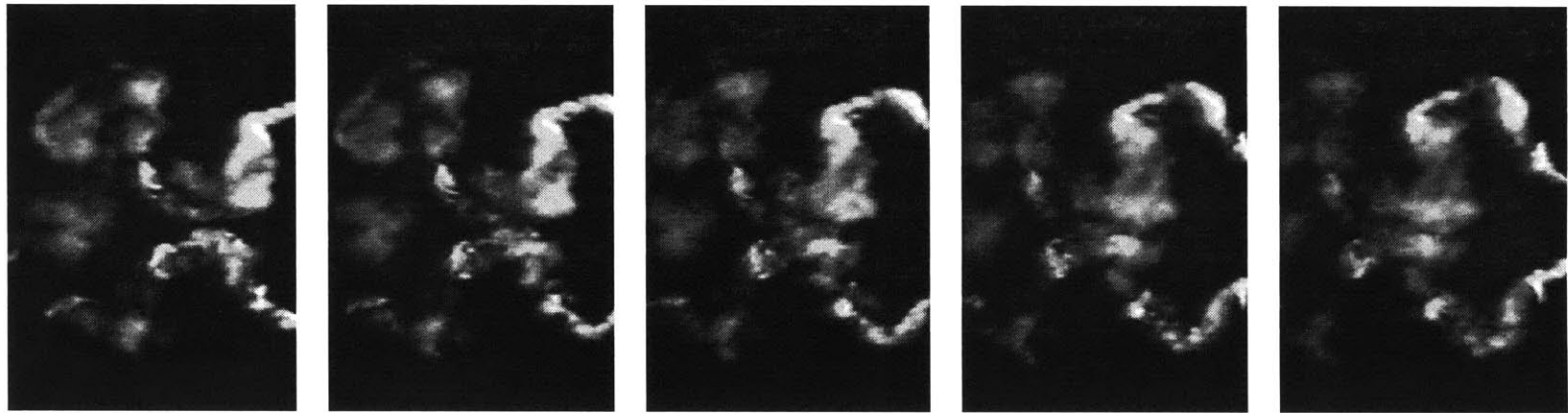
Run 16 : $\alpha = 25°$, St. # $= 0.4$, $\phi = 90°$ between each frame $\Delta t = 0.167$
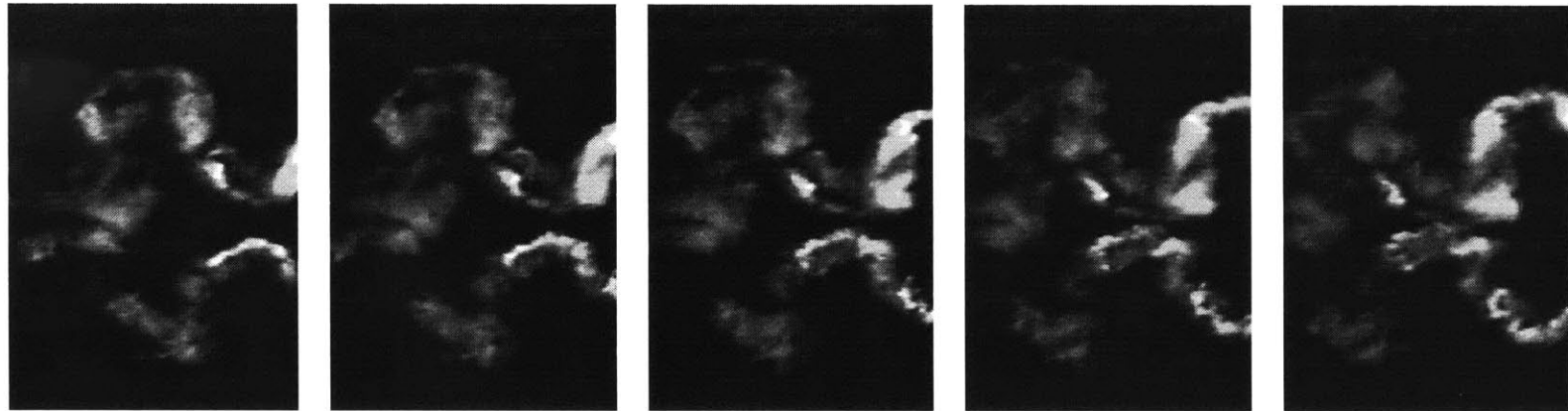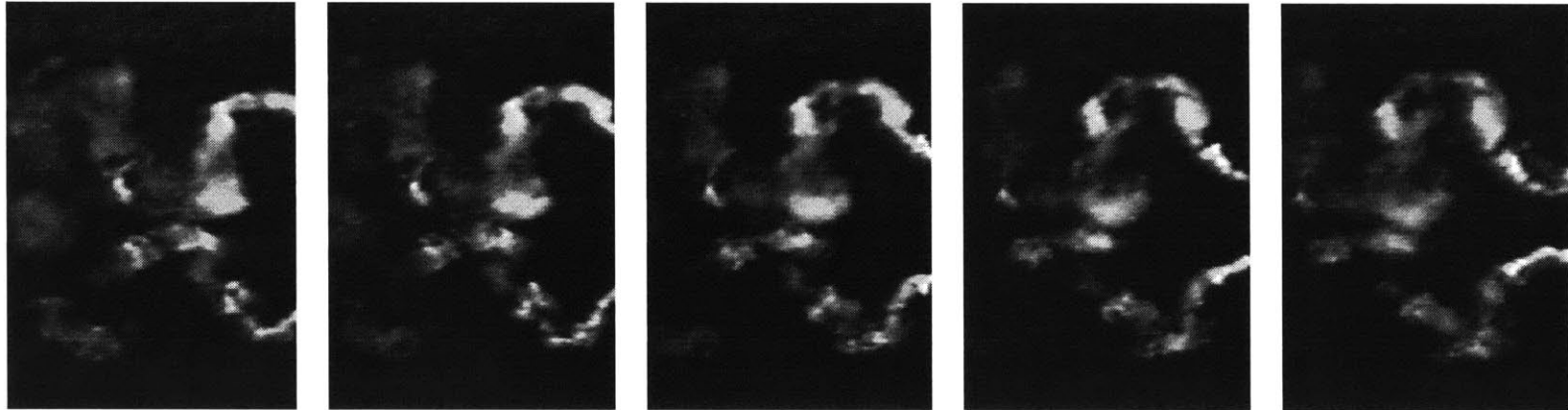
Run 17 : α = 30°, St. # = 0.4, φ = 90°   between each frame Δt = 0.167
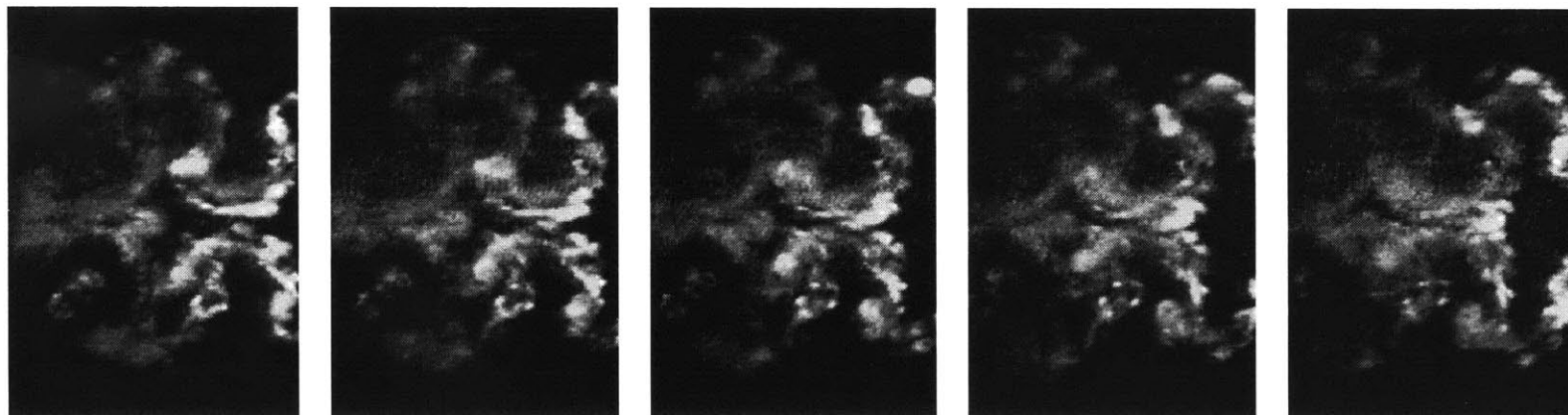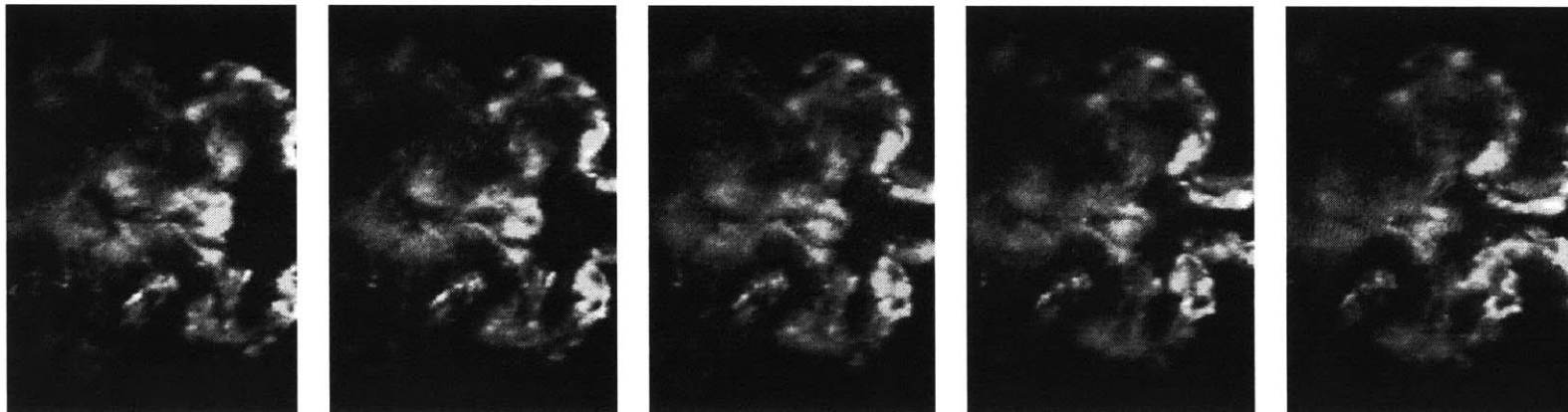
Run 18 : $\alpha = 10°$, St. # = 0.5, $\phi = 90°$ between each frame $\Delta t = 0.133$
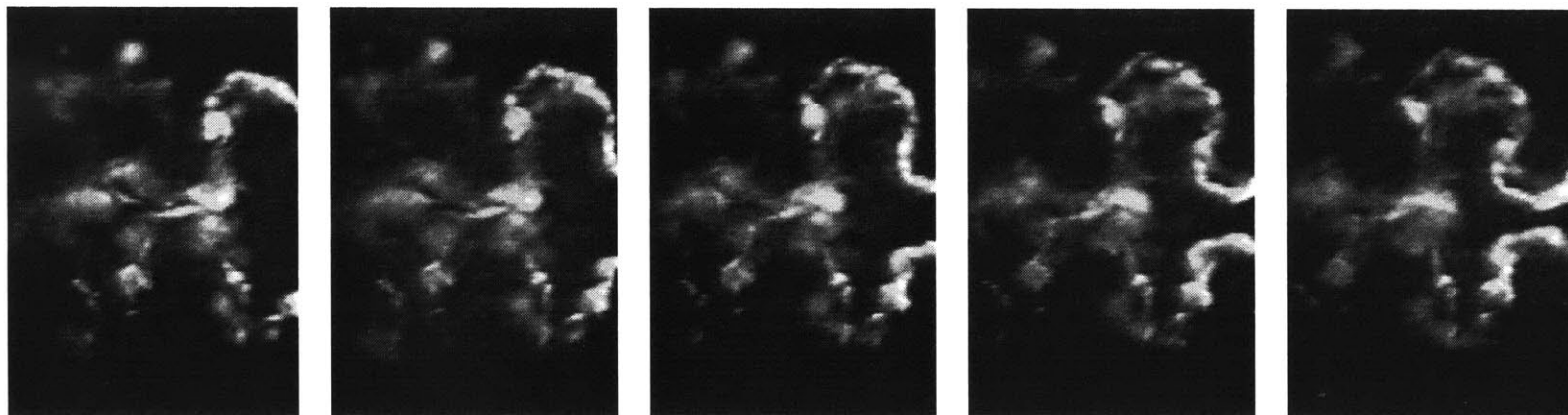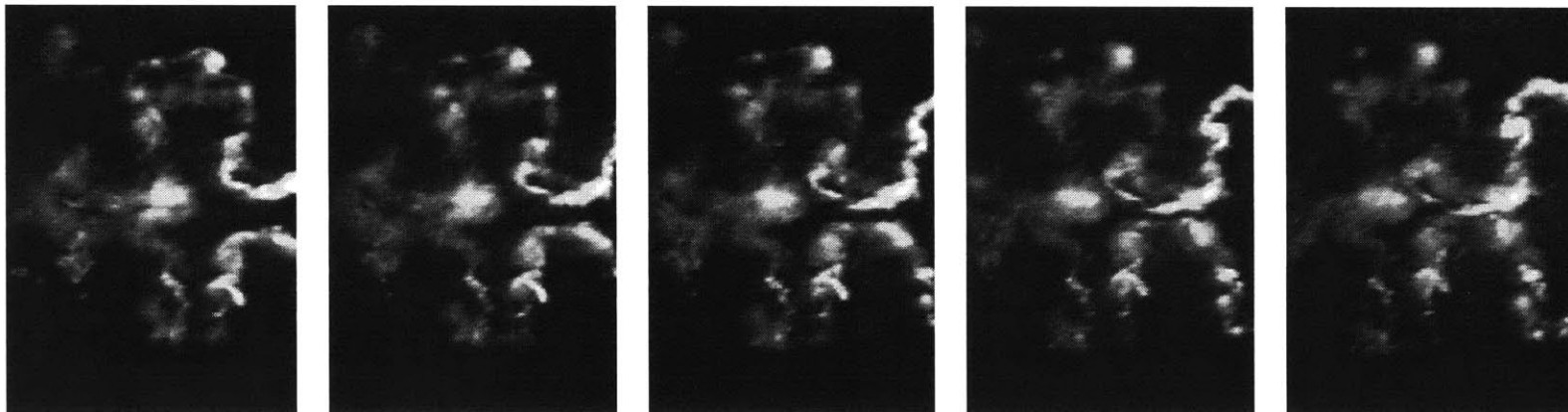
Run 19 : $\alpha = 15°$, St. # = 0.5, $\phi = 90°$ between each frame $\Delta t = 0.133$
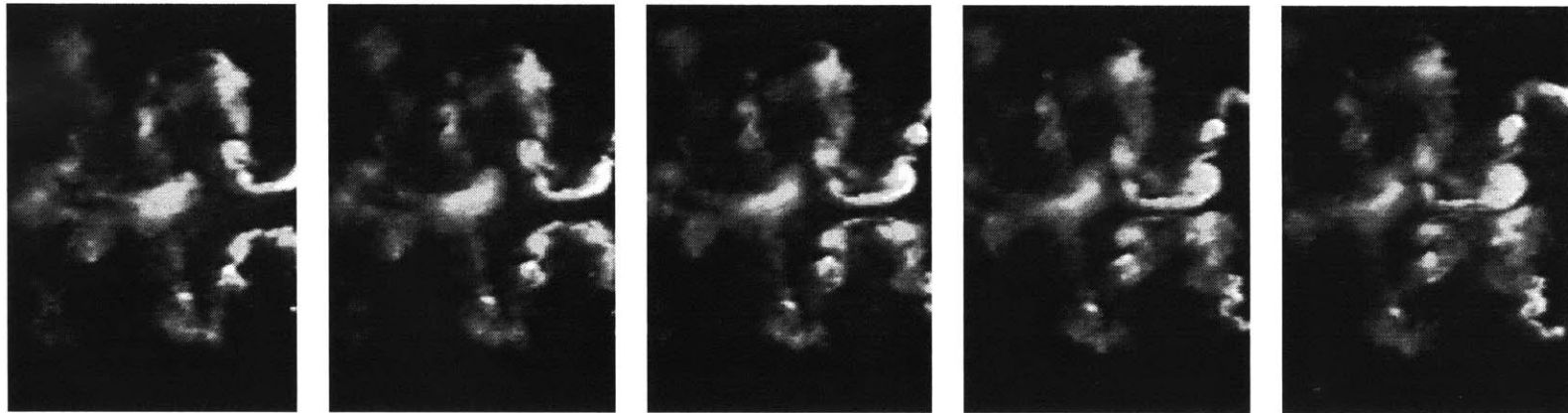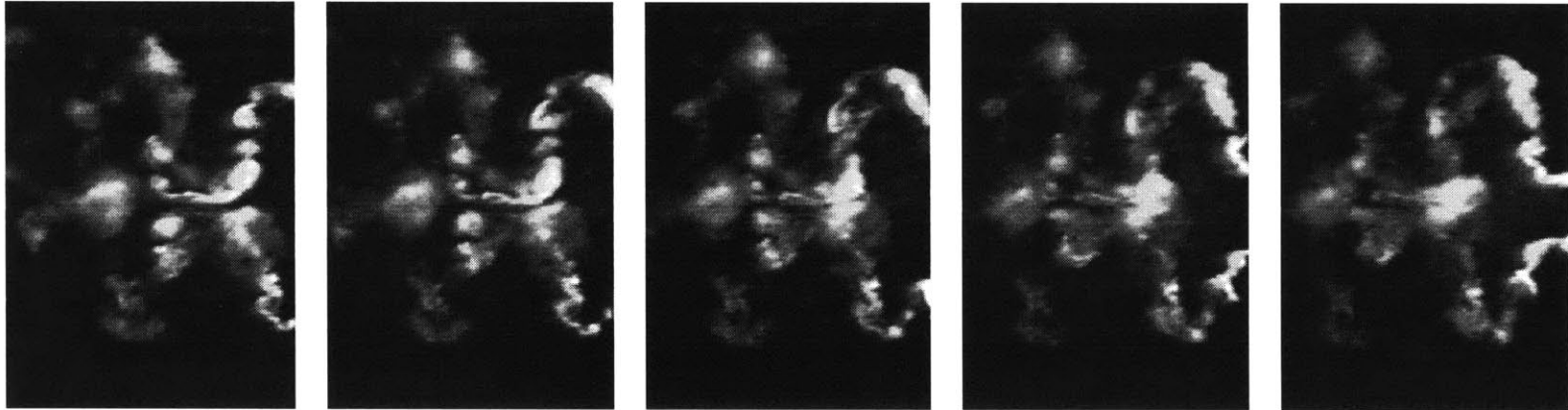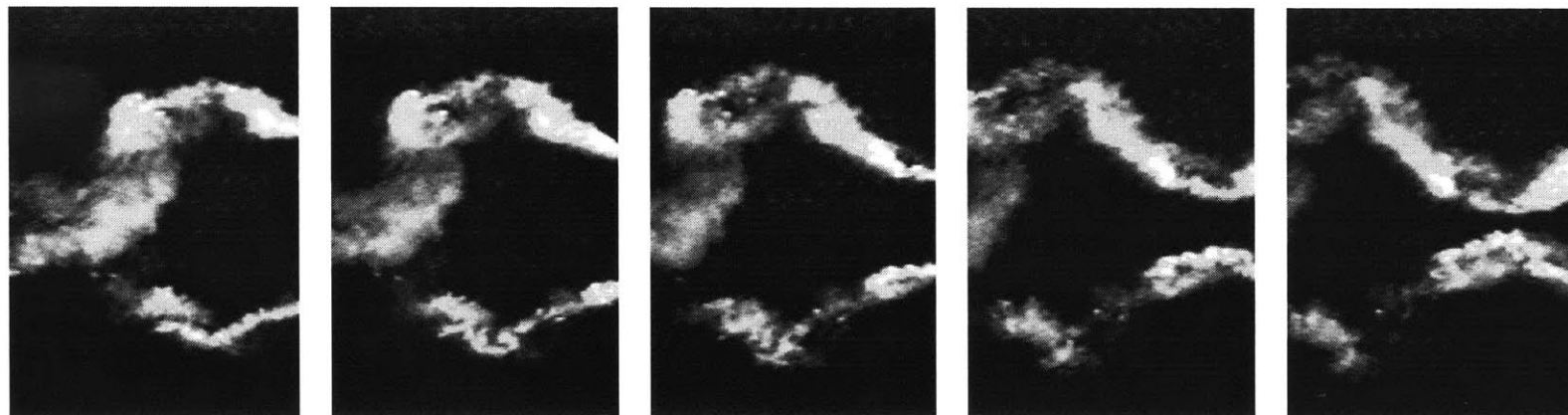
Run 20 : $\alpha = 20°$, St. # = 0.5, $\phi = 90°$ between each frame $\Delta t = 0.133$
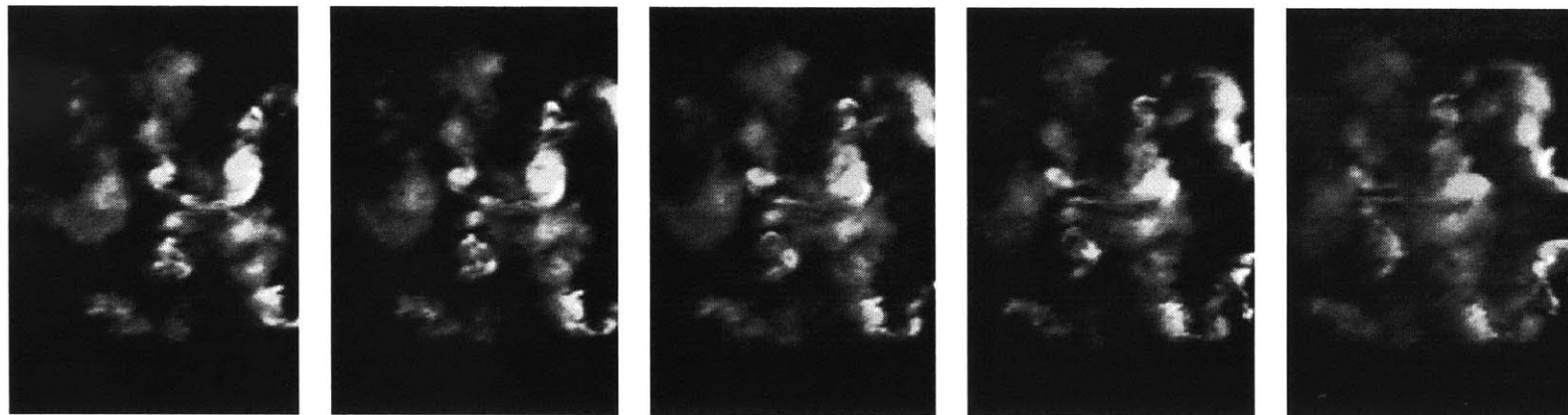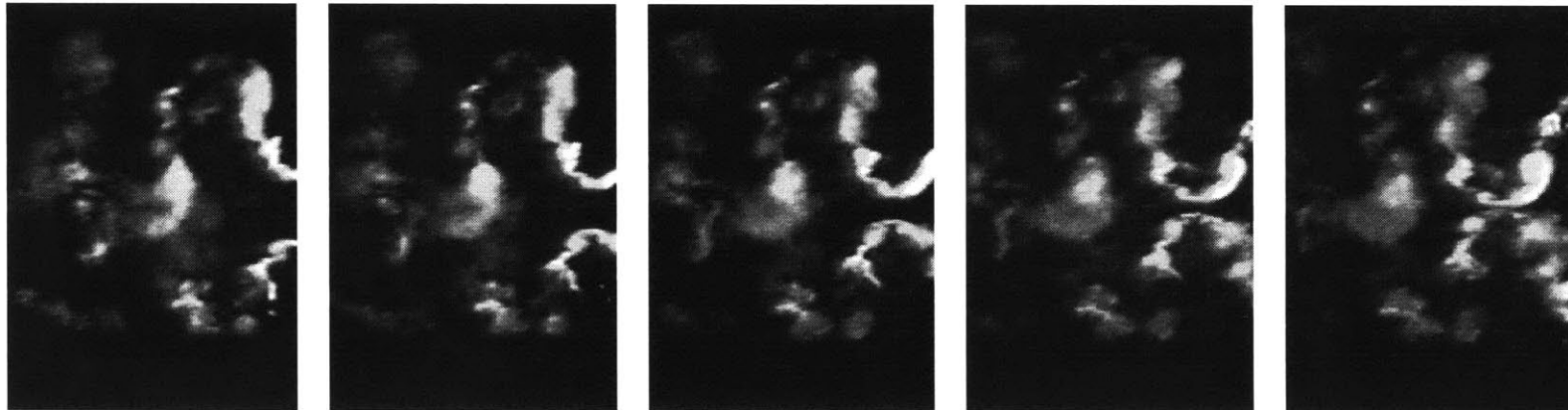
Run 21 : $\alpha = 25°$, St. # = 0.5, $\phi = 90°$ between each frame $\Delta t = 0.133$
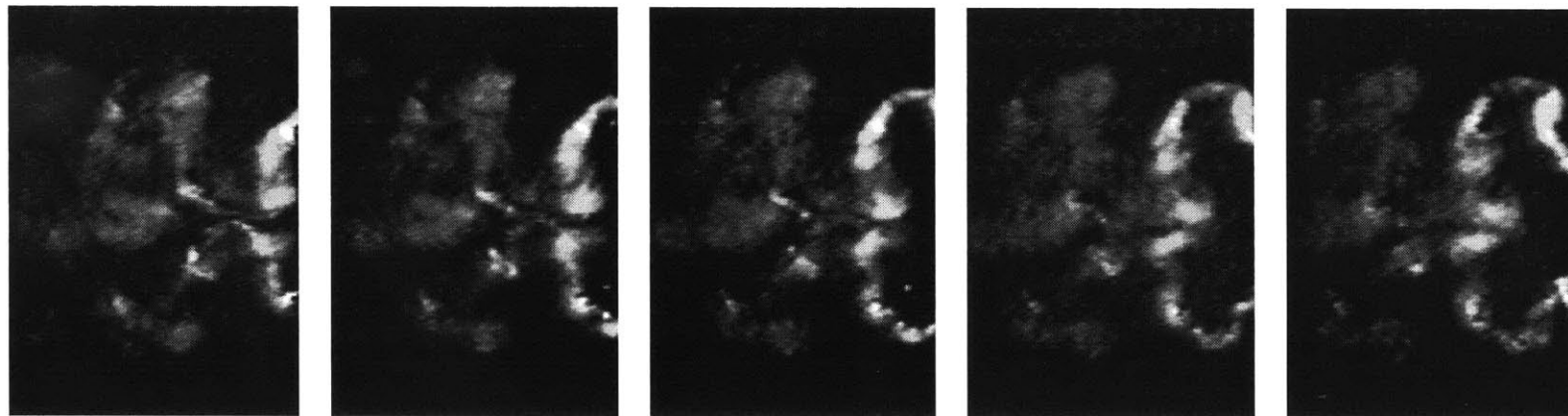
Run 22 : $\alpha = 30°$, St. # = 0.5, $\phi = 90°$ between each frame $\Delta t = 0.133$
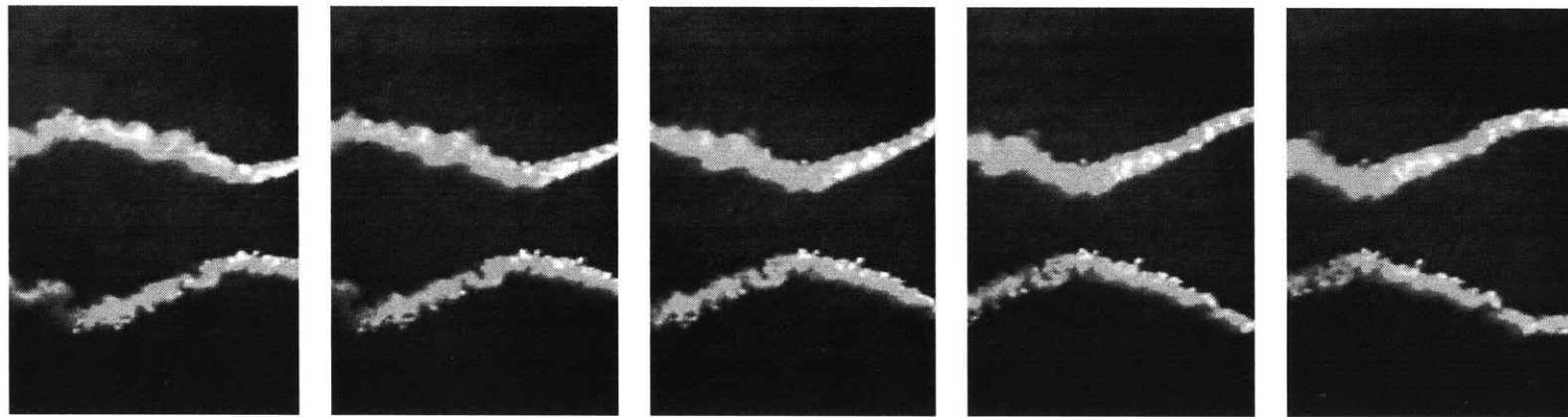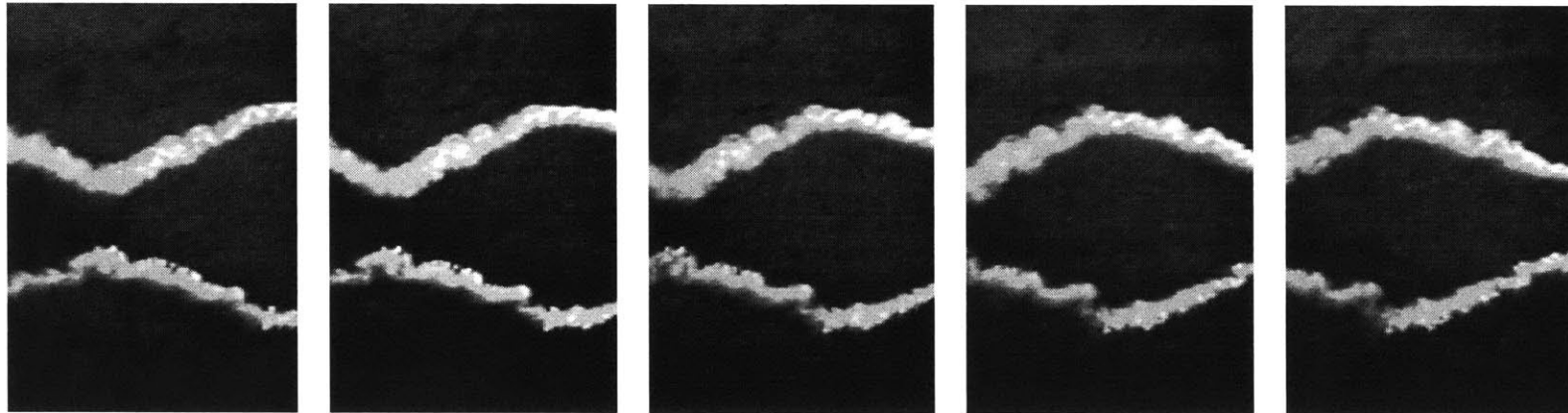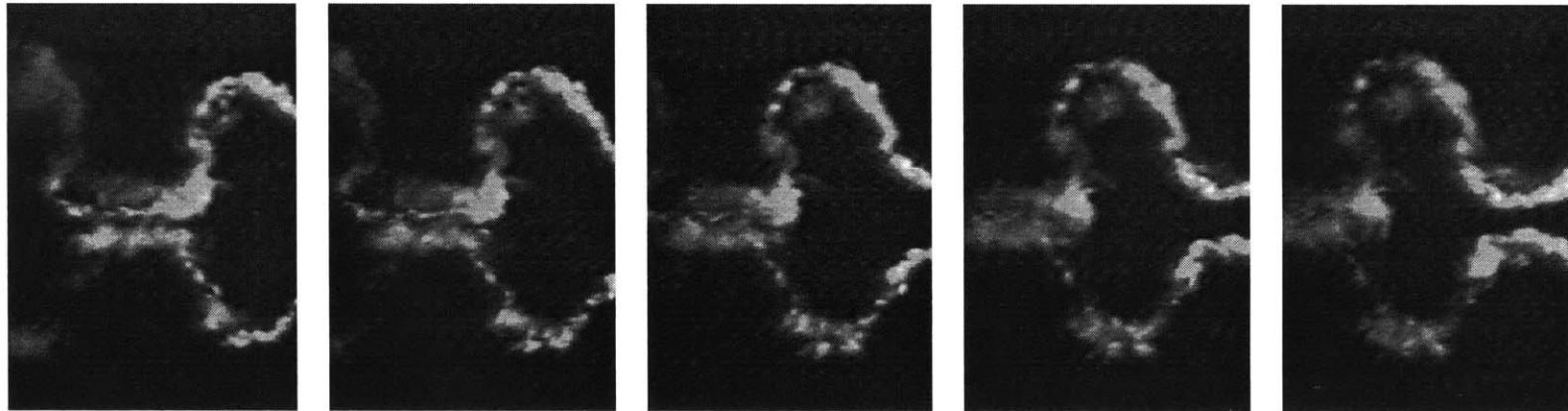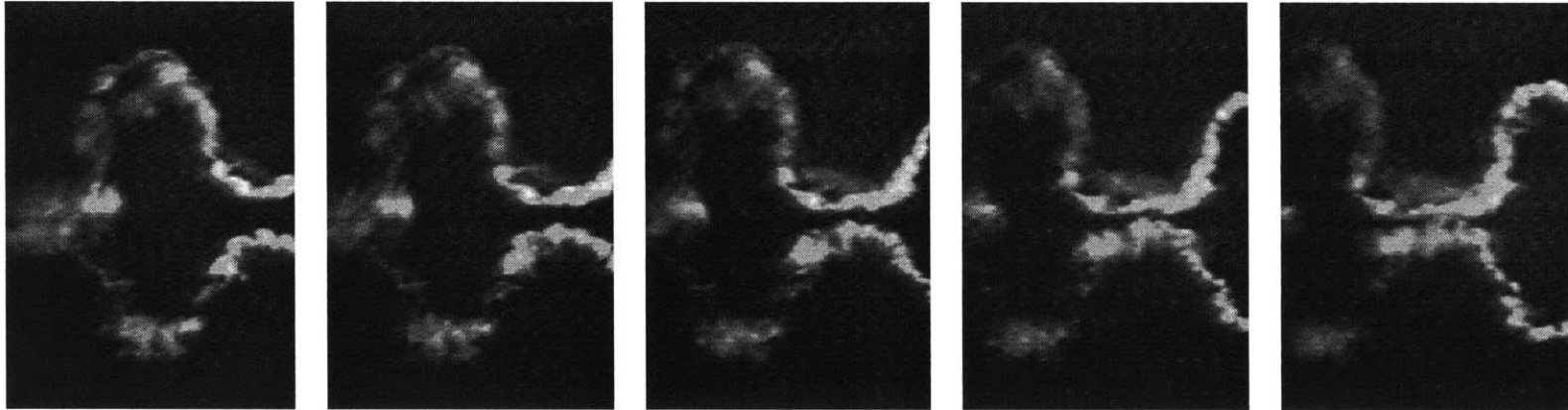
Run 23 : $\alpha = 10°$, St. # = 0.2, $\phi = 70°$ between each frame $\Delta t = 0.333$
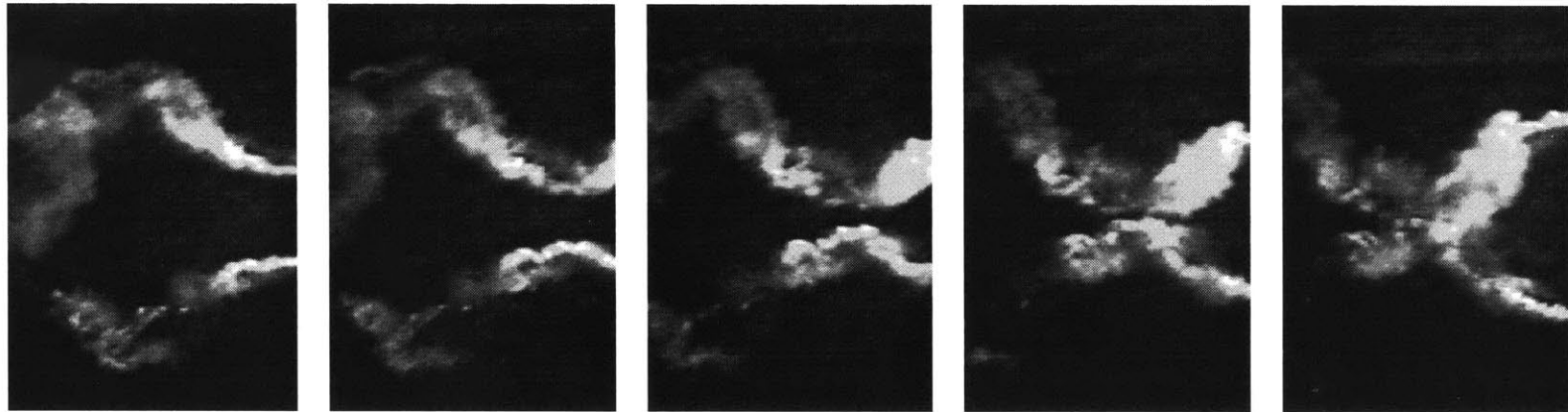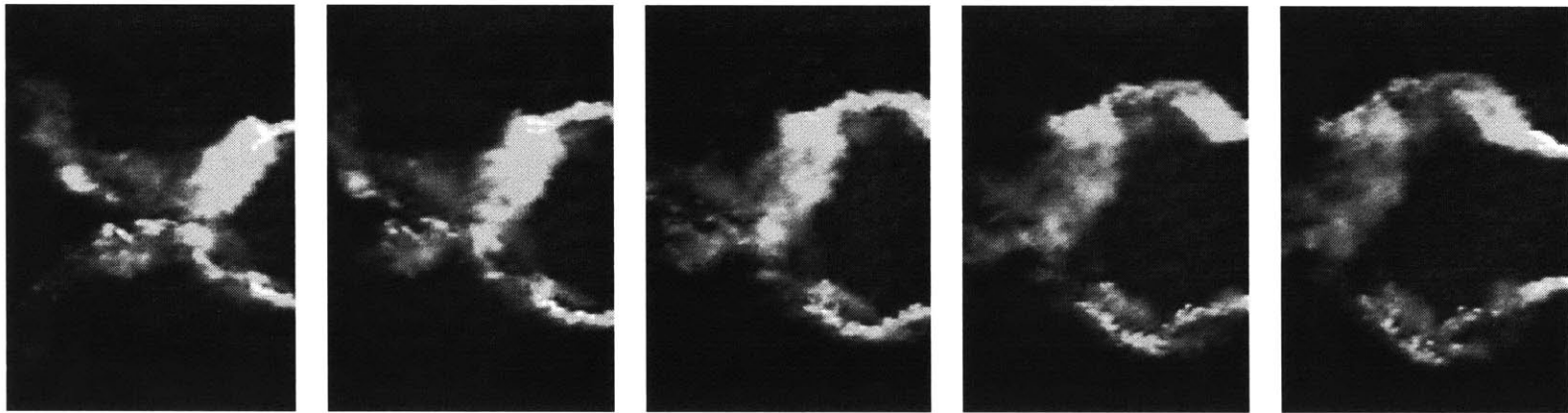
Run 24 : $\alpha = 20°$, St. # = 0.2, $\phi = 70°$ between each frame $\Delta t = 0.333$
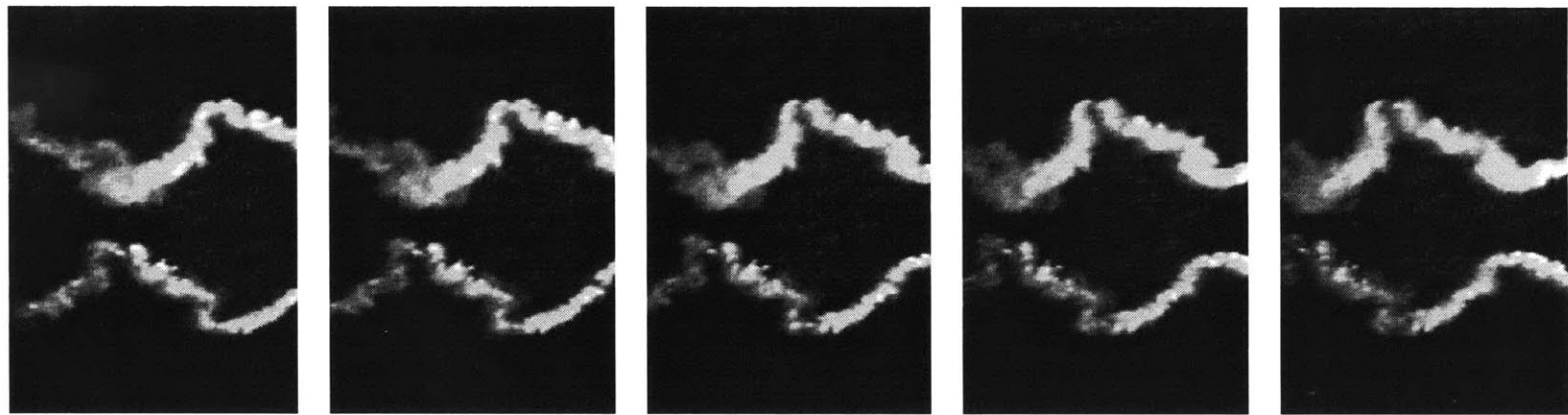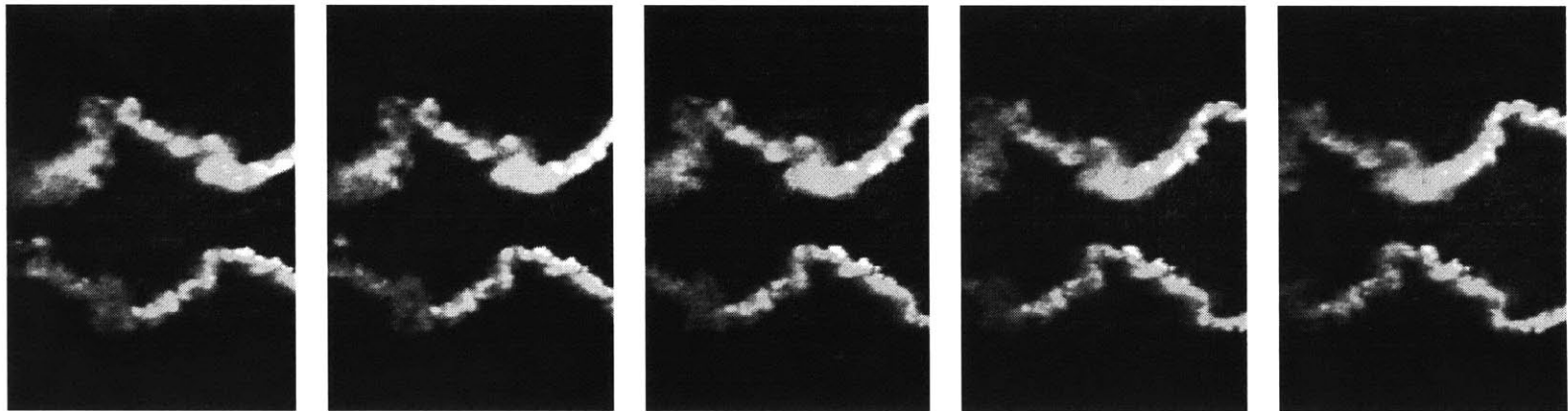
Run 25 : $\alpha = 10°$, St. # = 0.3, $\phi = 70°$ between each frame $\Delta t = 0.233$
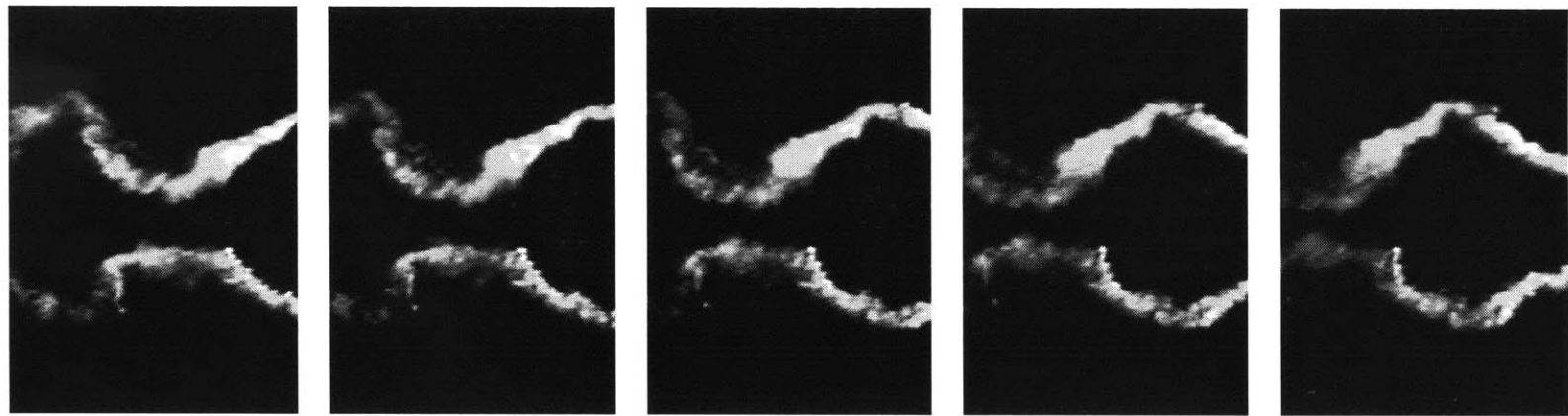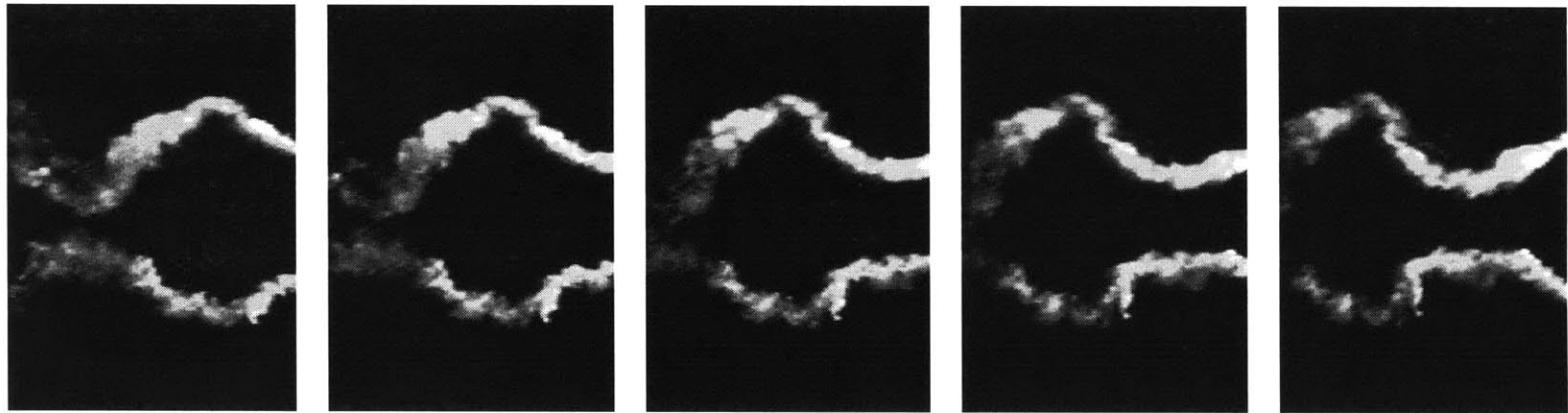
Run 26 : $\alpha = 20°$, St. # = 0.3, $\phi = 70°$ between each frame $\Delta t = 0.233$
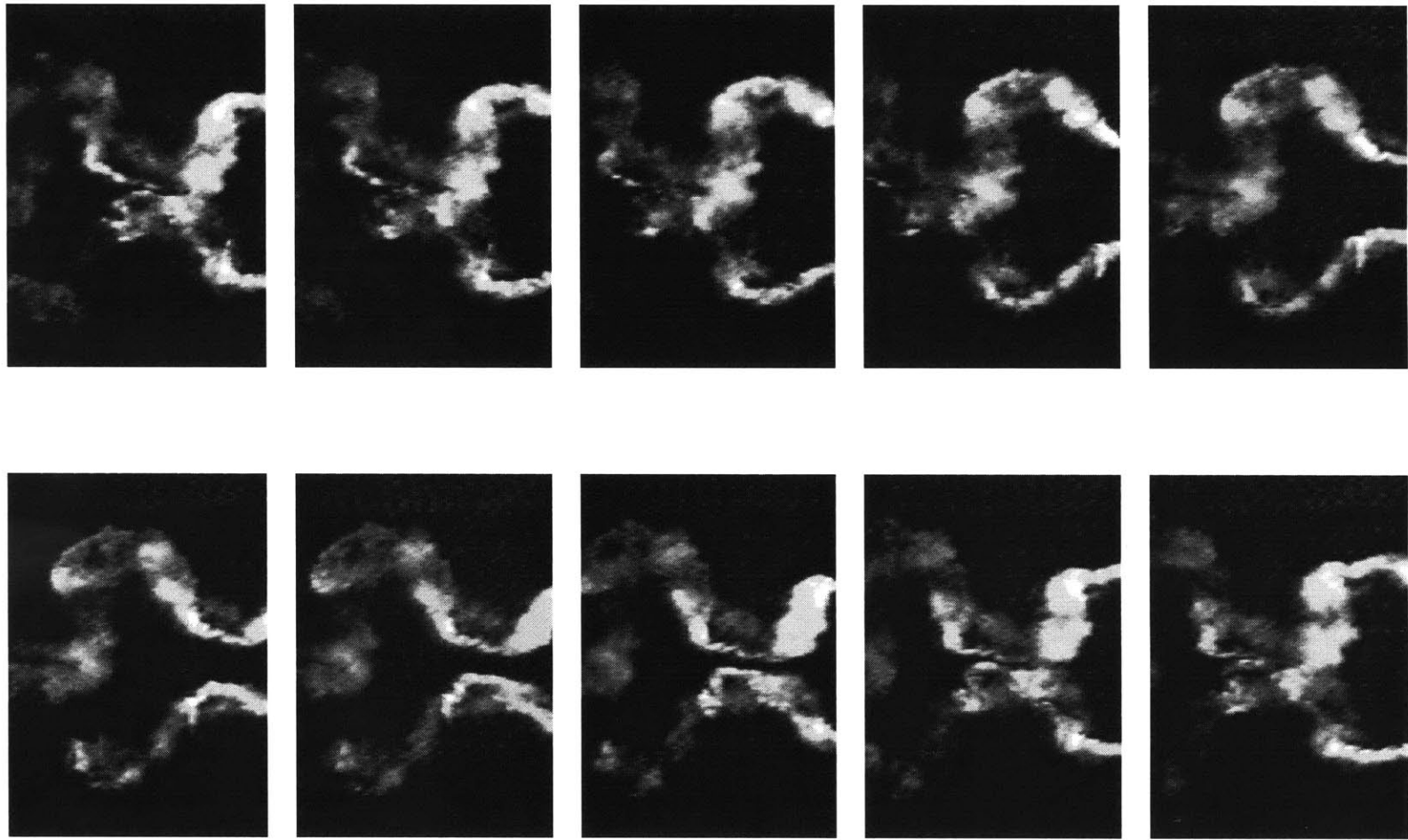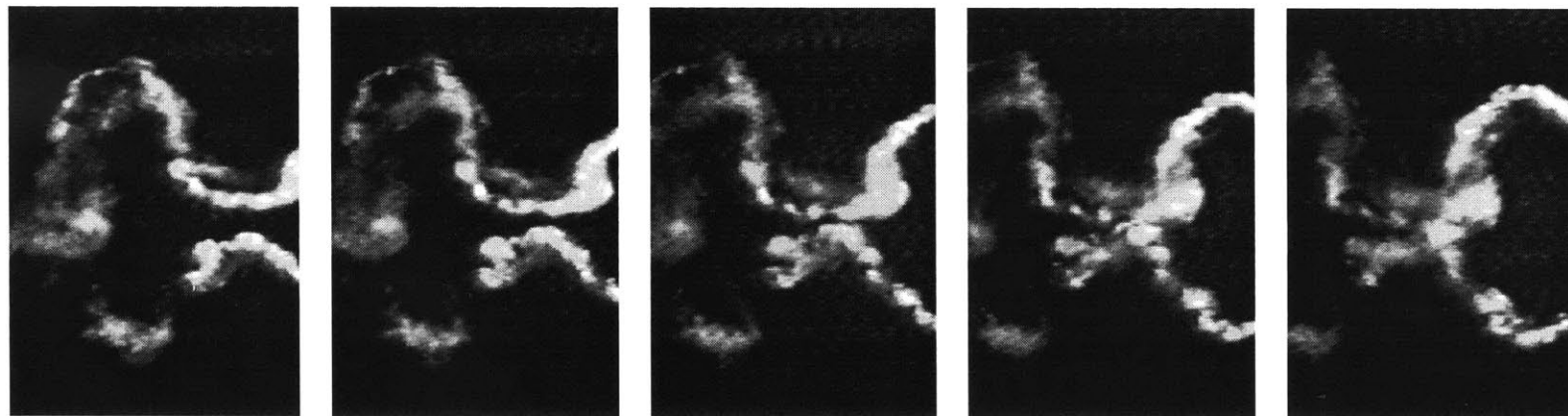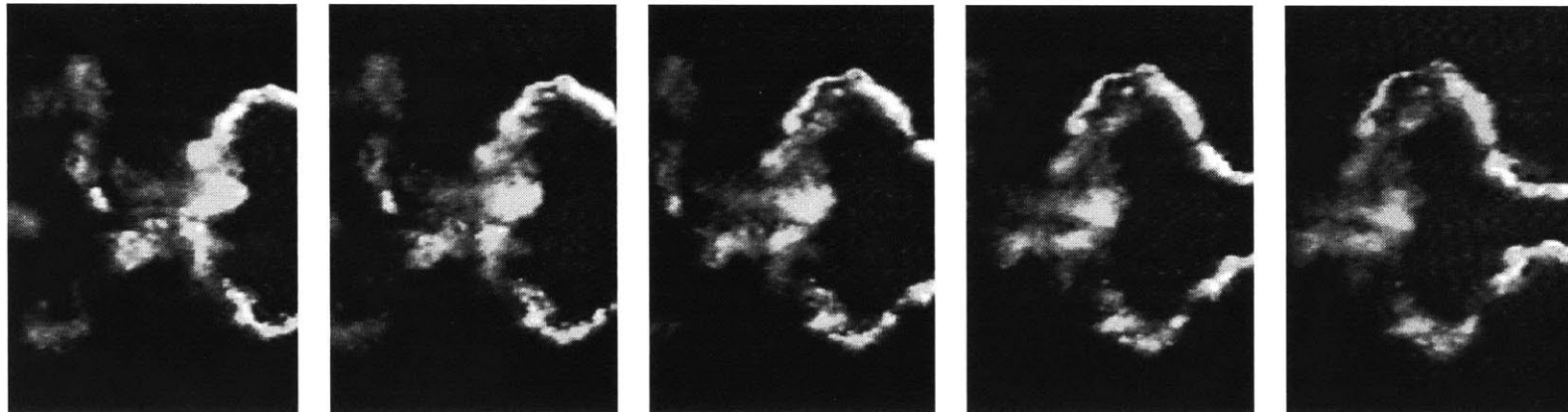
Run 27 : $\alpha = 30°$, St. # = 0.3, $\phi = 70°$ between each frame $\Delta t = 0.233$

Run 28 : $\alpha = 20°$, St. # = 0.4, $\phi = 70°$ between each frame $\Delta t = 0.167$

Run 29 : $\alpha = 30°$, St. # = 0.4, $\phi = 70°$ between each frame $\Delta t = 0.167$
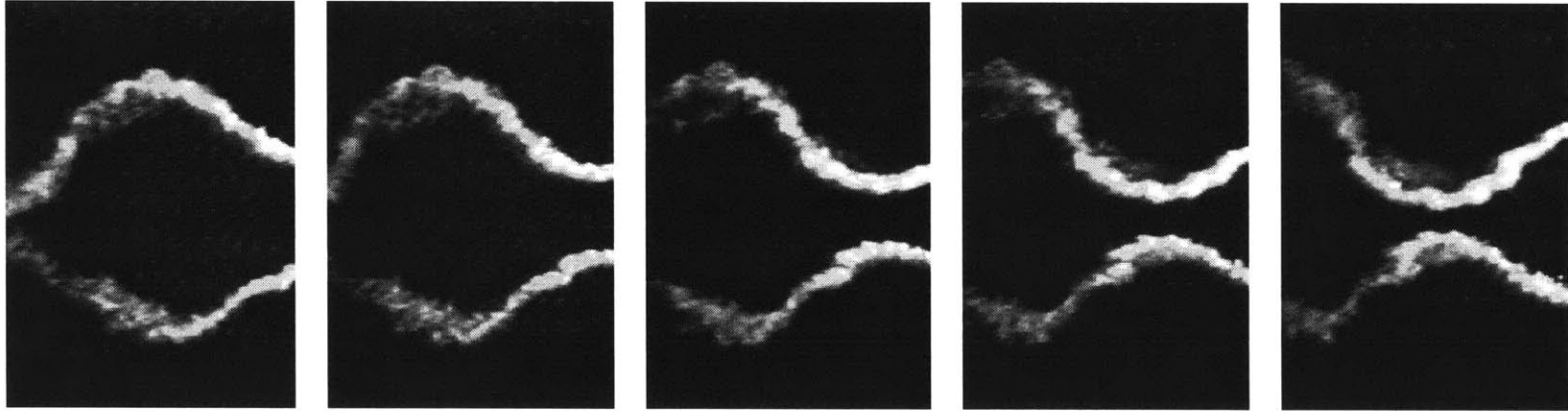
Run 30 : α = 10°, St. # = 0.2, φ = 110°   between each frame Δt = 0.333

Run 31 : $\alpha = 20°$, St. # = 0.2, $\phi = 110°$ between each frame $\Delta t = 0.333$
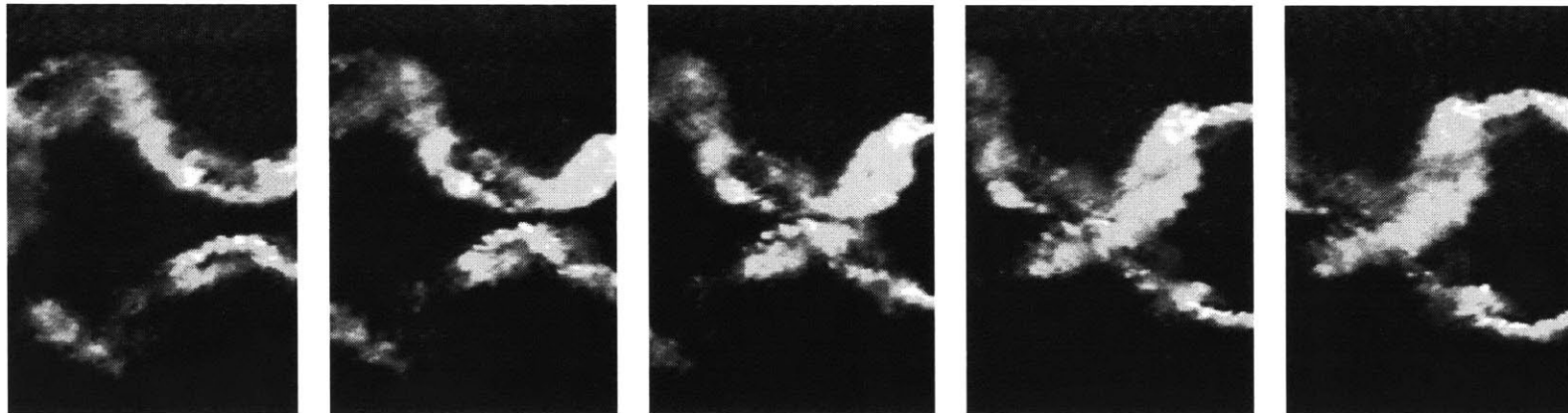
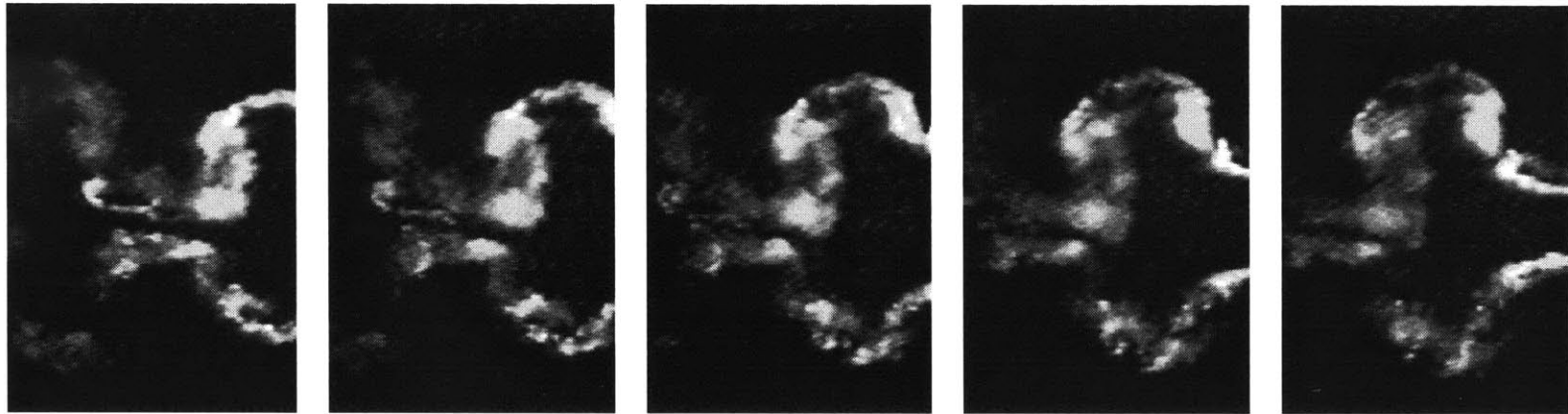Run 32 : $\alpha = 30°$, St. # = 0.2, $\phi = 110°$ between each frame $\Delta t = 0.333$

Run 33 : α = 10°, St. # = 0.3, φ = 110°   between each frame Δt = 0.233

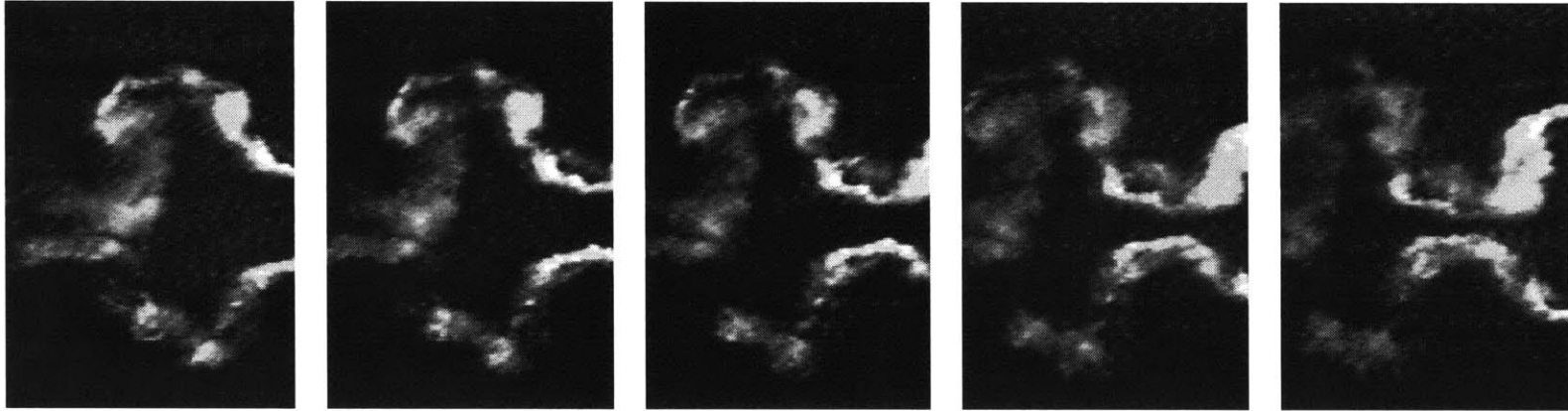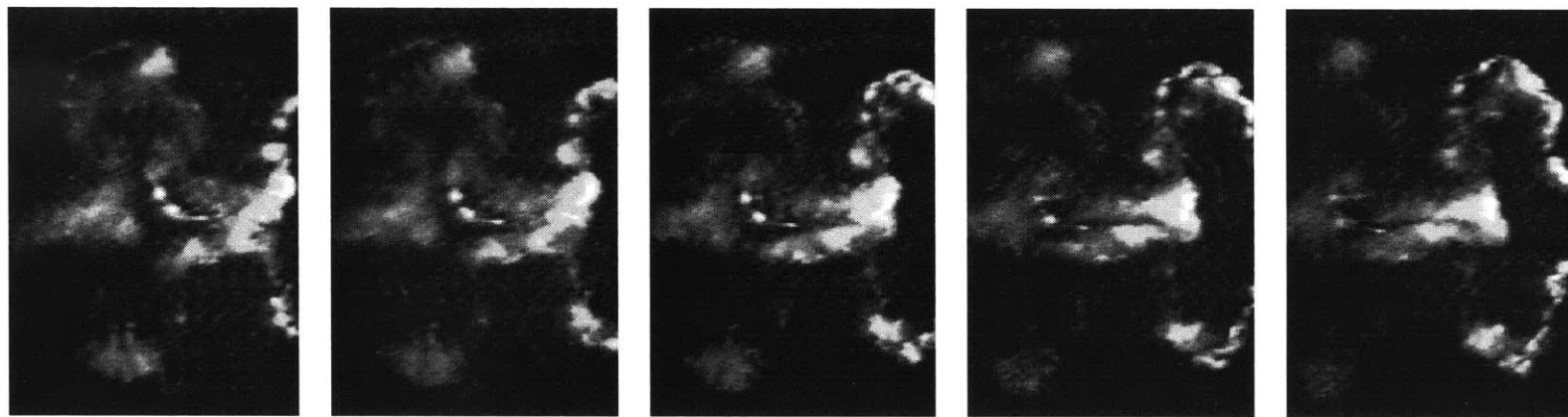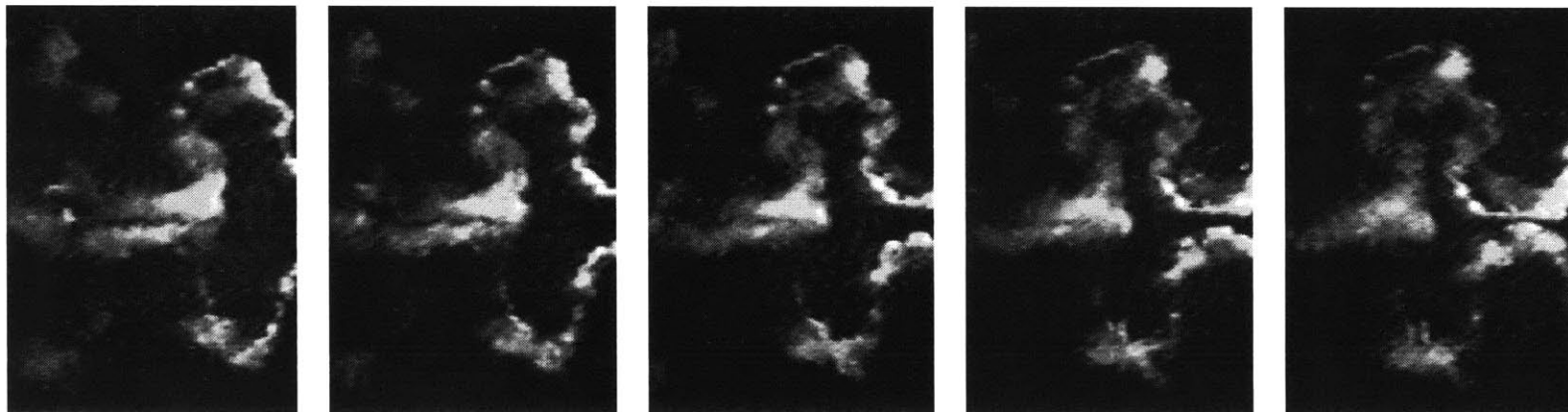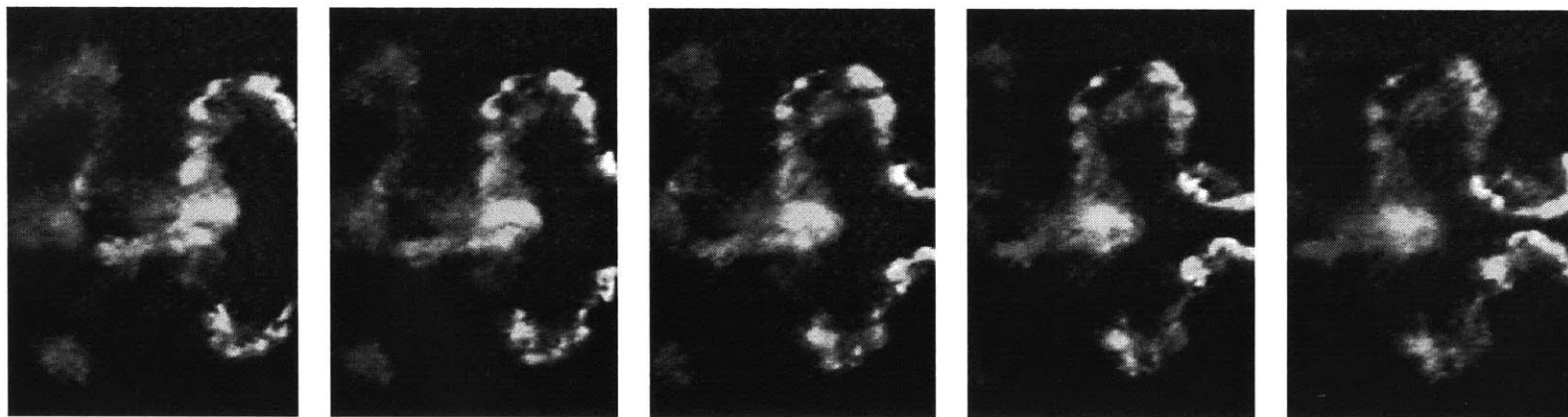Run 34 : $\alpha = 20°$, St. # = 0.3, $\phi = 110°$ between each frame $\Delta t = 0.233$

Run 35 : $\alpha = 30°$, St. # = 0.3, $\phi = 110°$ between each frame $\Delta t = 0.233$

Run 36 : $\alpha = 10°$, St. # = 0.4, $\phi = 110°$ between each frame $\Delta t = 0.167$
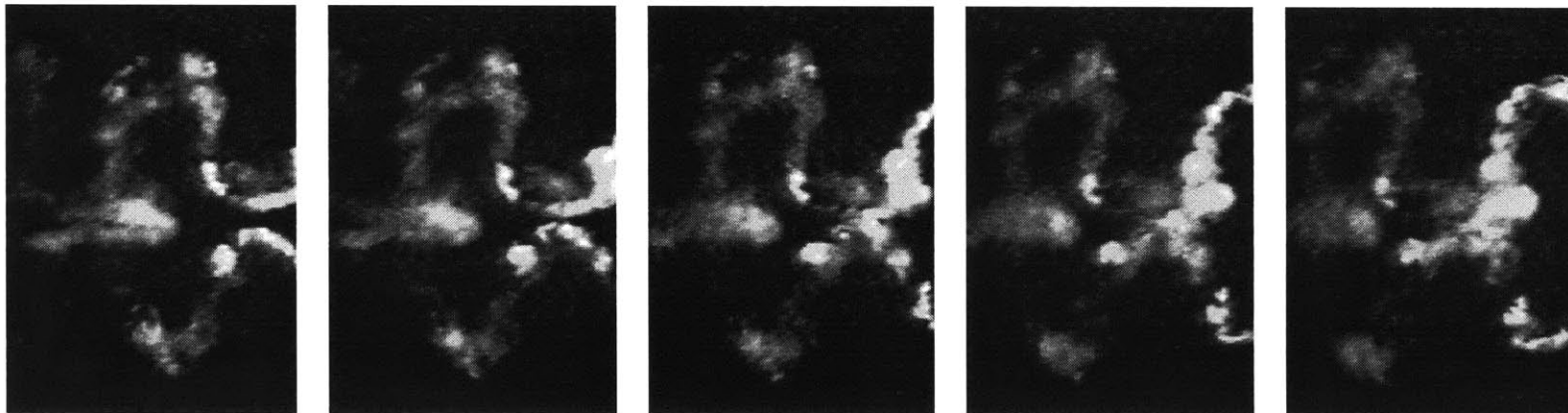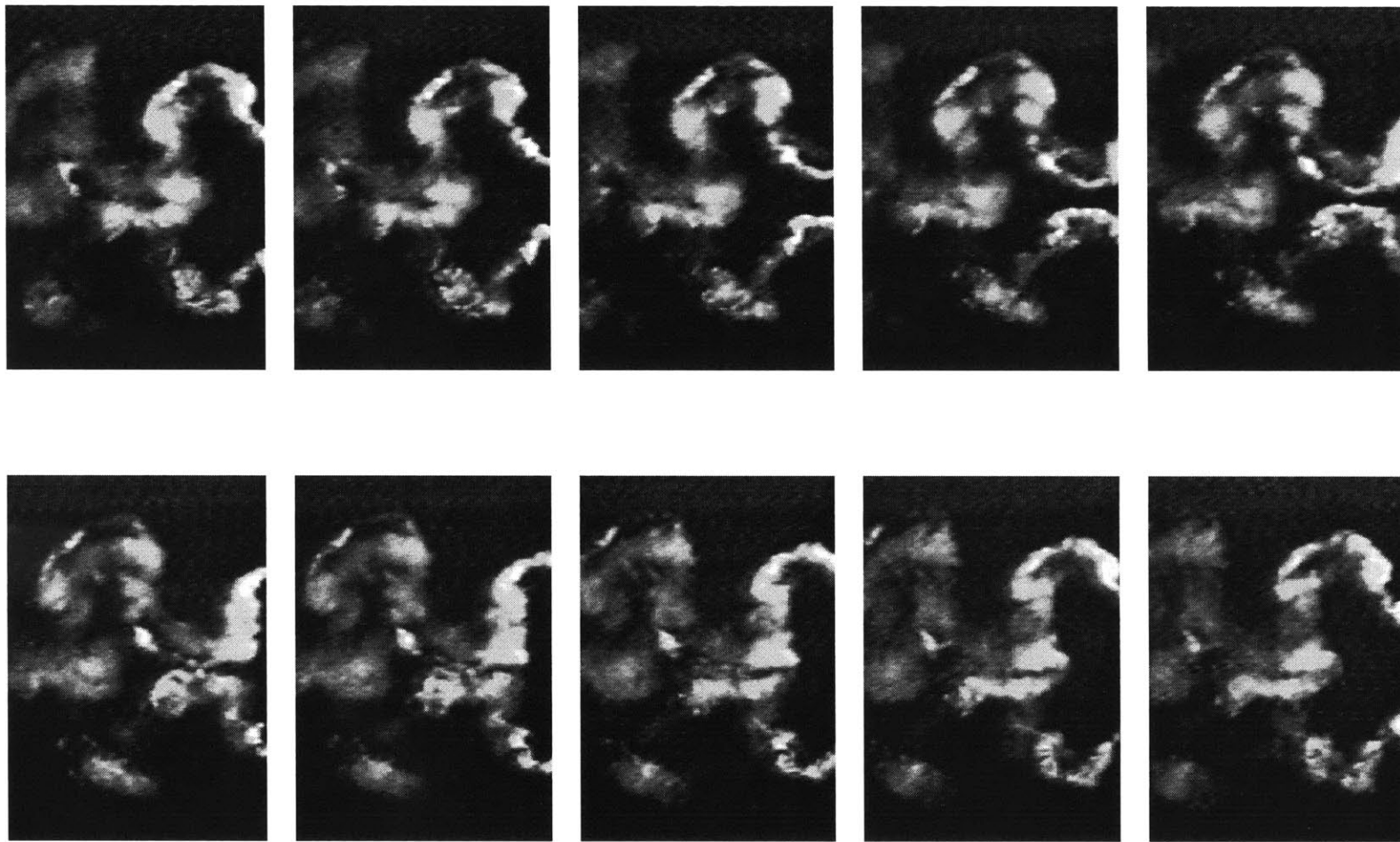
Run 37 : $\alpha = 20°$, St. # = 0.4, $\phi = 110°$ between each frame $\Delta t = 0.167$

Run 38 : $\alpha = 30°$, St. # = 0.4, $\phi = 110°$ between each frame $\Delta t = 0.167$

Bibliography

[1] Ames, D. Shear flow visualization at high Reynolds numbers. Master's Thesis, Massachusetts Institute of Technology, June 1998.

[2] Anderson, J.M. Vorticity control for efficient propulsion. Ph.D. Thesis, Massachusetts Institute of Technology, February 1996.

[3] Cusanelli, D.S. and Hundley, L. Stern flap powering performance on a spruance class destroyer: Ship trials and model experiments. Naval Engineers Journal, Mar. 1999, pp. 69-81.

[4] Czarnowski, J.T. Exploring the possibility of placing traditional marine vessel under oscillating foil propulsion. Master's Thesis, Massachusetts Institute of Technology, June 1997.

[5] Freymuth, P. Propulsive vortical signature of plunging and pitching airfoils. AIAA J., vol. 26, No. 7, July 1988.

[6] Gopalkrishnan, R. Vortex-induced forces on oscillating bluff cylinders. Ph.D. thesis. Massachusetts Institute of Technology, June 1993.

[7] Gray, J. "Studies in animal locomotion VI: The propulsive powers of the dolphin." *J. Exp. Biology* 13: 192-199, 1936.

[8] Harper, K.A., Berkemeier, M.D., Grace, S. Modeling the dynamics of spring-driven oscillating-foil propulsion. IEEE J. of Oceanic Engineering, v. 23, n3, Jul. 1998, pp. 285-296.

[9] Jones, K.D., Dohring, C.M, and Platzer, M.F. Wake structures behind plunging airfoils: A comparison of numerical and experimental results. AIAA Paper No. 96-0078.

[10] Koochesfahani, M.M. Vortical patterns in the wake of an oscillating airfoil. AIAA J., vol. 27, No. 9, Sept. 1989.

[11] Liu, P. A Time-Domain panel method for oscillating propulsors with both chordwise and spanwise flexibility. Dissertation, Memorial University of Newfoundland, 1996.

[12] Nagai, M., Teruya, I. and Isaka, K. Experimental study on an oscillating wing propulsive ship. Proc. Of the First Pacific/Asia Offshore Mechanics Symposium. ISOPE, 24-28 June 1990.

[13] Ohmi, K., Coutanceau, M., Daube, O., Loc, T.P. Further experiments on vortex formation around an oscillating and translating airfoil at large incidences. J. Fluid Mechanics (1991), vol. 225, pp. 607-630.

[14] Panda, J. and Zaman, K.B.M.Q. Experimental investigation of the flow field of an oscillating airfoil and estimation of lift from wake surveys. J. Fluid Mechanics (1994), vol. 265, pp. 65-95.

[15] Read, D. A. Oscillating foils for propulsion and maneuvering of ships and underwater vehicles. Master's Thesis, Massachusetts Institute of Technology, Feb. 2000.

[16] Techet, A.H. Vortical patterns behind a tapered cylinder. Master's Thesis, Massachusetts Institute of Technology, June 1998.

[17] Triantafyllou, M.S., Barrett, D.S., Streitlien, K. and Anderson, J.M. Flapping foils of high propulsive efficiency. J. Fluid Mechanics, April, 1998.

[18] Williamson, C.H.K. Three-dimensional vortex dynamics in bluff body wakes. Experimental Thermal and Fluid Science, 1996, 12:150-168.

[19] Williamson, C.H.K. and Roshko, A. Vortex formation in the wake of an oscillating cylinder. Journal of Fluids and Structures (1988) 2: 355-381.

[20] Yamaguchi, H. and Bose, N. Oscillating foils for marine propulsion. Proc. 4th International Offshore and Polar Engineering Conference, 1994, v. 3, p. 539-544.